The Incompressible Surface Navier-Stokes Equation

Numerical Approaches, Geometric Interactions and Extensions

Dissertation

zur Erlangung des akademischen Grades
Doctor rerum naturalium
(Dr. rer. nat.)

vorgelegt

dem Bereich Mathematik und Naturwissenschaften
der Technischen Universität Dresden

von

Sebastian Reuther

geboren am 14. November 1986 in Marienberg

Eingereicht am 18. Dezember 2018

Die Dissertation wurde in der Zeit von Juni/2012 bis Dezember/2018 im
Institut für Wissenschaftliches Rechnen angefertigt.

In Gedenken an meinen Vater.

Abstract

In this thesis, we consider the mathematical formulation of thin liquid films, which are approximated by two-dimensional evolving surfaces. The resulting equation, which describes the fluid flow on such fluid films, is a vector-valued surface partial differential equation, namely the incompressible surface Navier-Stokes equation. We are interested in numerical approaches in order to solve this equation as well as the interaction with the underlying geometry. Thereby, the highly nonlinear coupling of the interfacial hydrodynamics and the geometric properties is analyzed in various examples. First, we derive the vorticity-stream function formulation, which circumvents the vector-valued structure of the equations. This allows us to use the standard surface finite element method to solve this alternative approach numerically This has already been considered in the literature, but for stationary surfaces. Here, we extend these basic ideas and propose the respective formulation on evolving surfaces. However, it turned out, that this approach is only valid for surfaces which are topologically invariant to a sphere. Thus, we consider the incompressible surface Navier-Stokes equation in its original form and propose a further approach, which is based on the reformulation in the Euclidean basis, the Chorin projection method and spatial discretization with the standard surface finite element method. This allows us to study the geometric effects on more general surfaces. Additionally, we present two extensions of the proposed approaches. The first extension takes the interaction of the interfacial hydrodynamics and the surrounding fluids into account, for which a model based on phase fields is derived. Finally, an approach for polar liquid crystals on evolving surfaces is proposed, which couples the incompressible surface Navier-Stokes equation to another vector-valued surface partial differential equation for their orientational ordering. All examples show the highly nonlinear coupling between topology, geometric properties, defect interactions, shape changes and hydrodynamics.

Kurzfassung

In dieser Arbeit betrachten wir die mathematische Formulierung von dünnen Flüssigkeitsfilmen, die durch zweidimensionale bewegte Oberflächen approximiert werden. Die resultierende Gleichung, welche fluide Strömungen auf diesen Flüssigkeitsfilmen beschreibt, ist eine vektorwertige partielle Differentialgleichung, nämlich die inkompressible Navier-Stokes Gleichung auf Oberflächen. Wir sind interessiert an numerischen Algorithmen zur Lösung dieser Gleichung und der Interaktion mit der zu Grunde liegenden Geometrie. Dabei wird das hochgradig nichtlineare Zusammenspiel der Grenzflächenhydrodynamik und der Geometrie in verschiedenen Beipielen analysiert. Als erstes leiten wir die Stromfunktionsformulierung her, welche die vektorwertige Struktur der Gleichung umgeht. Damit ist es möglich, die gewöhnliche parametrische Finite Elemente Methode für das numerische Lösen des alternativen Ansatzes anzuwenden. Dies wurde bereits in der Literatur behandelt, jedoch für stationäre Oberflächen. In dieser Arbeit erweitern wir die grundlegenden Ideen und stellen die entsprechende Formulierung für bewegte Oberflächen auf. Dabei stellt sich heraus, dass dieser Ansatz nur für sphärenähnliche Oberflächen geeignet ist. Deshalb betrachten wir die inkompressible Navier-Stokes Gleichung auf Oberflächen in ihrer Originalform und verfolgen einen weiteren Ansatz, welcher auf der Formulierung in der Euklidischen Basis, dem Chorin Projektionsalgorithmus und der räumlichen Diskretisierung durch die gewöhnliche parametrische Finite Elemente Methode basiert. Dies erlaubt es uns, die geometrischen Effekte auf allgemeinere Oberflächen zu untersuchen. Zusätzlich präsentieren wir zwei Erweiterungen der angegebenen Ansätze. Die erste Erweiterung behandelt die Interaktion der Grenzflächenhydrodynamik mit umgebenden Fluiden, für welche ein Modell mit Phasenfeldern hergeleitet wird. Letztendlich beschreiben wir ein Model für polare Flüssigkristalle auf bewegten Oberflächen, welches die inkompressible Navier-Stokes Gleichung an eine vektorwertige partielle Differentialgleichung für deren orientierte Ordnung koppelt. In allen Beispielen ist die hochgradig nichtlineare Kopplung zwischen Topologie, Geometrieeigenschaften, Defektinteraktionen, Veränderungen der Oberfläche und Hydrodynamik zu verzeichnen.

Acknowledgment

Last but not least, I would like to gratefully say "Thank you" to my wife Jana, my lively son Emil, my parents Elke and Matthias as well as my brother Markus. Without your support this thesis would not have been possible in the present form. Finally, I would like to thank my father for his continuous support I have experienced by his honorable and unforgotten life.

Contents

1 | Introduction

One of the most illustrative examples for experiencing interfacial hydrodynamics can be observed in playing with soap bubbles. Here, the whole system consists of three parts, namely the surrounding air, the enclosed air and – most interestingly – the sopy water film in between. Obviously, this film is very thin, separates the inner and outer volume and is covered by colored structures. These structures emerge due to the interference phenomena, when light is broken and reflected on the inside and outside of the film. Soap bubbles follow the physical principle of minimizing the surface energy which explains the dynamic shape changes from their emergence to the so-called equilibrium state, where their shape becomes constant. But not only the shape of the bubble changes dynamically until the equilibrium state is reached, also the colored structures appearing on the surface nicely visualize the hydrodynamic behavior of the thin fluid film and the interaction with the surrounding air. Even for this simple and eye-catching example the fluidic properties of the thin film can be observed. This leads to the following questions

- What influences the flow behavior of thin fluid films?
- Which roles play dynamic shape changes and the local curvature?
- How does a fluid film interact with the surrounding?
- How can a fluid film be described mathematically?

More serious examples can be found in computer graphics, geophysics or cell

biology, where the fluidic behavior of cell or vesicle membranes is considered. Also so-called active liquid crystals on fluid interfaces are of special interest.

In this thesis we will study the physical effects influencing the hydrodynamics on general thin fluid films more carefully. In particular, we will see that the interfacial flow field can be manipulated by the (non-constant) curvature. Moreover, we will demonstrate the strong influence of dynamic shape changes on the flow field. These highly nonlinear phenomena are analyzed in detail and the physical properties are validated in various numerical studies.

Due to the fact that the thickness of such fluid films is typically orders of magnitudes lower than its lateral extension, the interface is considered as a two-dimensional curved surface. The only prize which has to be paid for this dimensional reduction, is the more complex mathematical description of the geometry and the equations. More precisely, describing interfacial hydrodynamics on surfaces generally generates a vector-valued surface partial differential equation (PDE), namely the incompressible surface Navier-Stokes equation. We will see that this PDE is a generalization of the usual incompressible Navier-Stokes equation in the two-dimensional flat space, but requires more care, e. g. regarding the differential operators. We propose two possible approaches based on finite elements in order to numerically solve the incompressible surface Navier-Stokes equation. Moreover, we demonstrate the flexibility of these approaches in various extensions.

1.1 Thesis overview

Considering interfacial hydrodynamics directly accounts for describing vector fields on surfaces. In Chapter 2 we introduce the required notation and basic concepts in dealing with vector fields on general evolving surfaces. Furthermore, a generic approach for describing locally defined vector-valued surface PDEs in the common Euclidean basis is proposed before the incompressible surface Navier-Stokes equation is derived and introduced in its original form. The following Chapter 3 is devoted for the surface vorticity-stream function formulation which is analogously derived as the usual formulation in the two-dimensional flat space. Thereby, the resulting equations are a system of coupled

scalar-valued surface PDEs which are numerically solved using the surface finite element method. We consider designed examples which nicely show the interplay of the flow field with the underlying geometry and the highly nonlinear dynamic behavior through shape changes. The introduced vorticity-stream function formulation is restricted to geometries which are topologically invariant to a sphere, cf. Section 3.4. Therefore, we propose a numerical approach which directly solves the incompressible surface Navier-Stokes equation in its original form and circumvents this issue in Chapter 4. To be more precise, the Cartesian representation of the equations and a minor transformation to reduce the numerical effort is used to componentwise apply the standard surface finite element method. We show some numerical examples on more general geometries, such as n-tori, for which the vorticity-stream function approach – as introduced in Chapter 3 – cannot be applied. Additionally, shape changes of the sphere based on a so-called nonic surface are used to dynamically influence the flow field. The two proposed approaches from Chapter 3 and Chapter 4 are used in various extensions which are introduced in the remaining chapters of this thesis. E. g. in Chapter 5, a diffuse domain/diffuse interface model is proposed, which accounts for the interaction of the fluid interface with surrounding bulk fluids. This model can be seen as an approach for two-phase flow problems with an interface condition based on the incompressible surface Navier-Stokes equation. We compare the numerical results of the proposed model with an experiment based on vesicles in shear flow. Furthermore, in Chapter 6 a model to describe surface liquid crystals on evolving surfaces is considered. Here, we use the method from Chapter 4 and a coupling to an additional vector-valued surface PDE for their orientational ordering. The numerical approach for the resulting system of equations is proposed and various examples are shown, which accounts for the strong influence of the flow field on the orientational ordering. In Chapter 7 we conclude this thesis and give some possibilities for further extensions.

1.2 Literature list

Some of the chapters of this thesis have partially been published in international journals. In the beginning of each chapter it is provided on which publication the respective chapter is based on. However, in the following list the author's publications are concluded and the respective chapters are shown.

Chapter 3:

[RV15]   S. Reuther and A. Voigt. The Interplay of Curvature and Vortices in Flow on Curved Surfaces. *Multiscale Model. Sim.*, 13(2):632–643, 2015

[RV18a]   S. Reuther and A. Voigt. Erratum: The Interplay of Curvature and Vortices in Flow on Curved Surfaces. *Multiscale Model. Sim.*, 16(3):1448–1453, 2018

[NRV17]   I. Nitschke, S. Reuther, and A. Voigt. Discrete Exterior Calculus (DEC) for the Surface Navier-Stokes Equation. In Dieter Bothe and Arnold Reusken, editors, *Transport Processes at Fluidic Interfaces*, pages 177–197. Springer, 2017

Chapter 4:

[RV18b]   S. Reuther and A. Voigt. Solving the incompressible surface Navier-Stokes equation by surface finite elements. *Phys. Fluids*, 30(1):012107, 2018

Chapter 5:

[RV16]   S. Reuther and A. Voigt. Incompressible two-phase flows with an inextensible Newtonian fluid interface. *J. Comput. Phys.*, 322:850–858, 2016

Chapter 6:

[NRV18]   I. Nitschke, S. Reuther, and A. Voigt. Hydrodynamic interactions in polar liquid crystals on evolving surfaces. *arXiv:1809.00457*, 2018

2 | Mathematical Preliminaries

In this chapter, we provide the required notation for describing a two-dimensional evolving surface, provide necessary tools for understanding the appearance of defects and introduce a general concept to numerically treat vector-valued surface PDEs. We further propose an alternative approach in order to derive the incompressible surface Navier-Stokes equation. Additionally, the equation is nondimensionalized and represented in Cartesian coordinates.

Parts of Section 2.1 and Section 2.3 are taken from the author's publication [RV15].

Contents

2.1 Overview

We consider thin films, whose thickness is much smaller than their lateral extension, and therefore use a two-dimensional surface to approximate the thin film. Such systems can often bend easily and we are interested in the question how an imposed geometric deformation influences the internal structure of the film. Such an interplay between geometry and internal structure is well studied for condensed matter systems, see [BG09]. The most illustrative example is probably the structure of a soccer ball, with 12 pentagons, serving as topological defects. Here, the favored regular order of hexagons, which easily tile a flat surface, cannot be extended throughout the surface of the sphere. We will discuss this example in more detail in Section 2.3. In technologically more relevant examples of soft materials, such defects are the key for chemical functionalization and provide the opportunity for the design of novel materials [Nel02].

Less explored is an analogy for fluid films. Here, the defects are vortices or saddles, which interact with the geometry. In [TVN10] this is analyzed for superfluidic films, i. e. fluids with zero viscosity and zero entropy, for which thin layers of liquid helium are used as a model system. In this thesis, we will concentrate on the more subtle case of fluids with nonzero viscosity and consider various numerical approaches for the incompressible surface Navier-Stokes equation in the following chapters. Thereby, we simultaneously concentrate on both the numerical approach and the interaction of the flow field with the underlying geometry.

2.2 General notation

In this section, we provide the general notation as well as differential operators, which are extensively used in the whole work. Note that this section serves

as a formulary more than a rigorous mathematical theory. Therefore, we leave some details which are not important or never used in the further chapters. Additionally, we use the Einstein summation convention over repeated indices (unless otherwise noted).

2.2.1 Geometric quantities

Throughout this thesis, we consider a regular moving oriented compact smooth Riemannian surface $\mathcal{S} = \mathcal{S}(t) \subset \mathbb{R}^3$ embedded in $\mathbb{R}^3$, where t denotes the time. Thereby, we restrict to the case $\partial\mathcal{S} = \emptyset$ (unless otherwise stated). We follow the general notation introduced in [NNPV18, NV18] and consider a parametrization $\mathbf{x}(t, y^1, y^2)$ of the surface $\mathcal{S}$ defined by

$$\mathbf{x}(t) : U \to \mathbb{R}^3\,,$$
$$\left(y^1, y^2\right) \mapsto \mathbf{x}\left(t, y^1, y^2\right)\,.$$

Thereby, $U \subset \mathbb{R}^2$ denotes a parameter set, t the time and y^1, y^2 the local coordinates. The $\mathbb{R}^3$ representation of the surface $\mathcal{S}$ is given by $\mathcal{S}(t) = \mathbf{x}(t, U)$. From now on we drop the time argument, since it is clear that everything is time-dependent, and use a similar approach as in [RV18b] but for the more general case of evolving surfaces. Furthermore, the local basis is given by $\{\partial_1\mathbf{x}, \partial_2\mathbf{x}\}$, where ∂_i is the partial derivative in the direction of the i-th local coordinate, and the unit outer normal vector field is denoted by $\boldsymbol{\nu}$. Accordingly, the first fundamental form or metric tensor $\boldsymbol{g}$ is defined by $g_{ij} = \langle \partial_i\mathbf{x}, \partial_j\mathbf{x}\rangle$. In the following chapters we will see that the second fundamental form (or shape operator) $\mathcal{B}_{ij} := -\langle \partial_i\mathbf{x}, \partial_j\boldsymbol{\nu}\rangle$ plays an important role and occurs in several so-called extrinsic contributions in the considered equations. Also the two main curvatures – the Gaussian curvature κ and the mean curvature $\mathcal{H}$ – typically enters such equations. Thereby, κ and $\mathcal{H}$ are defined by the product and the sum of the two principal curvatures, respectively. Furthermore, let $\mathsf{T}^{(d)}_{\mathbf{x}}\mathcal{S} = \mathsf{T}^{(d)}_{\mathbf{x}}\mathcal{S}(t)$ denotes the tangent space of d-tensors on $\mathbf{x} \in \mathcal{S}$ and let $\mathsf{T}^{(d)}\mathcal{S} = \mathsf{T}^{(d)}\mathcal{S}(t) = \sqcup_{\mathbf{x}\in\mathcal{S}}\mathsf{T}^{(d)}_{\mathbf{x}}\mathcal{S}$ be the respective tangent bundle of tensor fields of order d. We further assume that the surface $\mathcal{S}$ moves in normal direction with a prescribed normal velocity $v_{\boldsymbol{\nu}}$.

We exclusively restrict to a transversal observer for the surface $\mathcal{S}$. This means we use an Eulerian perspective for the tangential space and a Lagrangian point of view in normal direction. For further details on the choice of an observer we refer to [NRV18, NV18].

In the following we omit high and low indices as it is usual in the context of covariant and contravariant descriptions of vector fields and exclusively restrict to contravariant case. This means that a contravariant vector field $\mathbf{p} \in \mathsf{T}^{(1)}\mathcal{S}$ is denoted by $\mathbf{p} = \mathbf{p}_i \partial_i \mathbf{x}$.

Let $\Omega_h = \Omega_h(t) := \{\mathbf{X} \in \mathbb{R}^3 \mid |d_{\mathcal{S}}(\mathbf{X})| < h/2\} \subset \mathbb{R}^3$ be a (tubular) neighborhood around the surface $\mathcal{S}$ with sufficiently small thickness h and a signed-distance function $d_{\mathcal{S}}$. The coordinate system y^1, y^2 of the surface $\mathcal{S}$ is extended by a third coordinate in normal direction denoted by ξ, which yields an arbitrary coordinate system of the neighborhood Ω_h. Furthermore, we introduce the coordinate projection operator $\pi_c : \Omega_h \to \mathcal{S}$, $\mathbf{X} \mapsto \mathbf{x}$ defined by $\mathbf{X} = \mathbf{x} + d_{\mathcal{S}}(\mathbf{X})\boldsymbol{\nu}(\mathbf{x})$, which is injective for sufficiently small h, cf. [DE13]. E.g. for a vector field $\mathbf{p} \in \mathsf{T}^{(1)}\mathcal{S}$ defined by $\mathbf{p} = \mathbf{p}_i \partial_i \mathbf{x}$ and a scalar field $\psi \in \mathsf{T}^{(0)}\mathcal{S}$ on the surface $\mathcal{S}$ we introduce the smooth normal extensions into the neighborhood Ω_h by $\widetilde{\psi}(\mathbf{X}) := \psi(\mathbf{x})$ and $\widetilde{\mathbf{p}}(\mathbf{X}) := \mathbf{p}(\mathbf{x})$, respectively. This means that scalar quantities are constantly extended and vector fields are parallel transported off the surface. Note that the introduction of the tubular neighborhood and the coordinate projection is necessary for expressing the differential operators from the next Section 2.2.2 in the $\mathbb{R}^3$ basis.

Next, we introduce the Cartesian representation of some of the geometric quantities from above. Assume the normal vector to be represented in the Euclidean basis, i.e. $\boldsymbol{\nu} \in \mathbb{R}^3$. Thus, the shape operator, the mean curvature and the Gaussian curvature is given by $[\mathcal{B}]_{ij} := [-\mathcal{D}\boldsymbol{\nu}]_{ij} = -\mathcal{D}_j\boldsymbol{\nu}_i$, $\mathcal{H} = \mathrm{trace}\,\mathcal{B}$ and $\kappa = \frac{1}{2}(\mathcal{H}^2 - \|\mathcal{B}\|^2)$, respectively. The differential operator $\mathcal{D}$ is thereby formally defined by $\mathcal{D} := \boldsymbol{\pi}\nabla$ and its components are given by $\mathcal{D}_i := \boldsymbol{\pi}_{ij}\partial_j$, where $\boldsymbol{\pi} = \mathbf{I} - \boldsymbol{\nu} \otimes \boldsymbol{\nu}$ denotes the projection into the tangent space and $\otimes$ the outer product. In the literature, $\mathcal{D}$ is often called surface gradient, e.g. in [DE07a, DE07b]. For scalar fields this operator coincides with the covariant surface gradient, but for vector fields we have to carefully distinguish between the surface gradient operator from above and the covariant differential operator, see Section 2.2.2.

2.2.2 Differential operators

Following [NNPV18, NV18, NRV18] the covariant surface gradient operator, the surface divergence and the two surface curl operators are denoted by $\nabla_{\mathcal{S}} : \mathsf{T}^{(d)}\mathcal{S} \to \mathsf{T}^{(d+1)}\mathcal{S}$, $\mathrm{div}_{\mathcal{S}} : \mathsf{T}^{(d+1)}\mathcal{S} \to \mathsf{T}^{(d)}\mathcal{S}$, $\mathrm{rot}_{\mathcal{S}} : \mathsf{T}^{(d+1)}\mathcal{S} \to \mathsf{T}^{(d)}\mathcal{S}$, $\mathrm{Rot}_{\mathcal{S}} : \mathsf{T}^{(d)}\mathcal{S} \to \mathsf{T}^{(d+1)}\mathcal{S}$ with $d \in \mathbb{N}_0$, respectively. A more detailed definition of the differential operators can be found in [NNPV18]. Let $\psi : \mathcal{S} \to \mathsf{T}^{(0)}\mathcal{S}$ be a scalar-valued function and $\mathbf{p} : \mathcal{S} \to \mathsf{T}^{(1)}\mathcal{S}$ a vector field defined on the surface $\mathcal{S}$, which is extended to the tubular neighborhood Ω_h by using the coordinate projection according to Section 2.2.1. We restrict to the Euclidean basis for the neighborhood Ω_h and thus the extension of the vector field $\mathbf{p}$ in the neighborhood Ω_h in the Euclidean basis is denoted by $\widehat{\mathbf{p}} : \mathcal{S} \to \mathbb{R}^3$. Note that the vector field $\widehat{\mathbf{p}}$ now has a normal component, which is completely arbitrary. Especially, $\widehat{\mathbf{p}} \cdot \boldsymbol{\nu} \neq 0$ is possible in this setting. Analogously, let $\mathbf{t} : \mathcal{S} \to \mathsf{T}^{(2)}\mathcal{S}$ be a 2-tensor field on the surface $\mathcal{S}$ and $\widehat{\mathbf{t}}$ its extension in Cartesian coordinates with again non-vanishing normal components in general. Thus, the first order differential operators represented in the Euclidean basis can be written as

$$[\nabla_{\mathcal{S}}\psi]_i = [\mathcal{D}\psi]_i = \mathcal{D}_i\psi \tag{2.1}$$

$$[\mathrm{Rot}_{\mathcal{S}}\,\psi]_i = [\boldsymbol{\nu} \times \nabla_{\mathcal{S}}\psi]_i = \epsilon_{kli}\boldsymbol{\nu}_k \mathcal{D}_l\psi \tag{2.2}$$

for the scalar function ψ,

$$[\mathcal{D}\widehat{\mathbf{p}}]_{ij} = \mathcal{D}_j\widehat{\mathbf{p}}_i \tag{2.3}$$

$$[\nabla_{\mathcal{S}}\widehat{\mathbf{p}}]_{ij} = [\boldsymbol{\pi}\mathcal{D}\widehat{\mathbf{p}} + (\widehat{\mathbf{p}} \cdot \boldsymbol{\nu})\,\mathcal{B}]_{ij} = \boldsymbol{\pi}_{ik}\mathcal{D}_j\widehat{\mathbf{p}}_k + \widehat{\mathbf{p}}_k\boldsymbol{\nu}_k\mathcal{B}_{ij} \tag{2.4}$$

$$\mathrm{div}_{\mathcal{S}}\,\widehat{\mathbf{p}} = \mathrm{trace}\,(\mathcal{D}\widehat{\mathbf{p}}) + (\widehat{\mathbf{p}} \cdot \boldsymbol{\nu})\,\mathcal{H} = \mathcal{D}_i\widehat{\mathbf{p}}_i + \widehat{\mathbf{p}}_i\boldsymbol{\nu}_i\mathcal{H} \tag{2.5}$$

$$\mathrm{rot}_{\mathcal{S}}\,\widehat{\mathbf{p}} = -\,\mathrm{div}_{\mathcal{S}}\,(\boldsymbol{\nu} \times \widehat{\mathbf{p}}) = -\epsilon_{kli}\mathcal{D}_i\,(\boldsymbol{\nu}_k\widehat{\mathbf{p}}_l) \tag{2.6}$$

for the vector field $\widehat{\mathbf{p}}$ and

$$\left[\mathcal{D}\widehat{\mathbf{t}}\right]_{ijk} = \mathcal{D}_k\widehat{\mathbf{t}}_{ij} \tag{2.7}$$

$$\begin{aligned}
\left[\mathrm{div}_{\mathcal{S}}\,\widehat{\mathbf{t}}\right]_i &= \left[\boldsymbol{\pi}\,\mathrm{trace}\,(\mathcal{D}\widehat{\mathbf{t}}) + \boldsymbol{\nu}^T\widehat{\mathbf{t}}\mathcal{B} + \mathcal{H}\boldsymbol{\pi}\widehat{\mathbf{t}}\boldsymbol{\nu}\right]_i \\
&= \boldsymbol{\pi}_{ik}\mathcal{D}_j\widehat{\mathbf{t}}_{kj} + \boldsymbol{\nu}_k\widehat{\mathbf{t}}_{kj}\mathcal{B}_{ij} + \mathcal{H}\boldsymbol{\pi}_{ij}\widehat{\mathbf{t}}_{jk}\boldsymbol{\nu}_k \tag{2.8}
\end{aligned}$$

for the tensor field $\widehat{\mathbf{t}}$ with the Levi-Civita symbol ϵ_{kli}. These identities follow by considering the derivatives in the neighborhood Ω_h and restricting to the surface $\mathcal{S}$. A more detailed derivation can be found in [NNPV18, NV18]. Note that we use the same symbols for the first order differential operators in the local and the Cartesian representation of the vector field $\mathbf{p}$ as well as the tensor field $\mathbf{t}$.

With the definitions from above we are now able to formulate second order operators on the surface $\mathcal{S}$. For the scalar-valued function ψ we define the Laplace-Beltrami operator by

$$\Delta_{\mathcal{S}}\psi = \operatorname{div}_{\mathcal{S}} \nabla_{\mathcal{S}}\psi\,. \tag{2.9}$$

For the vector field $\mathbf{p}$ there are two possible definitions of the vector Laplacian, namely the Bochner Laplacian

$$\boldsymbol{\Delta}^{\mathrm{B}}\mathbf{p} = \operatorname{div}_{\mathcal{S}} \nabla_{\mathcal{S}}\mathbf{p} \tag{2.10}$$

and the Laplace-deRham operator or Hodge Laplacian

$$\boldsymbol{\Delta}^{\mathrm{dR}}\mathbf{p} = -\left(\boldsymbol{\Delta}^{\mathrm{RR}} + \boldsymbol{\Delta}^{\mathrm{GD}}\right)\mathbf{p} \tag{2.11}$$

with $\boldsymbol{\Delta}^{\mathrm{RR}}\mathbf{p} = \operatorname{Rot}_{\mathcal{S}} \operatorname{rot}_{\mathcal{S}} \mathbf{p}$ and $\boldsymbol{\Delta}^{\mathrm{GD}}\mathbf{p} = \nabla_{\mathcal{S}}\left(\operatorname{div}_{\mathcal{S}} \mathbf{p}\right)$, cf. [AMR88]. These two operators are connected by the Weizenböck identity, i.e.

$$\boldsymbol{\Delta}^{\mathrm{B}}\mathbf{p} = -\boldsymbol{\Delta}^{\mathrm{dR}}\mathbf{p} + \kappa\mathbf{p}\,. \tag{2.12}$$

From that point of view it can be easily seen that the Bochner Laplacian and the Laplace-deRham operator match (except of the sign), if the Gaussian curvature is zero. This is, e.g., the case in flat space or on a surface on which one of the principal curvatures vanishes identically such as a cylindrical shape. Analogously, we define these operators for the extended vector field $\widehat{\mathbf{p}}$. Thus, the extended Bochner Laplacian is given by

$$\boldsymbol{\Delta}^{\mathrm{B}}\widehat{\mathbf{p}} = \operatorname{div}_{\mathcal{S}} \nabla_{\mathcal{S}}\widehat{\mathbf{p}} \tag{2.13}$$

and the extended Laplace-deRham or Hodge Laplacian by

$$\boldsymbol{\Delta}^{\mathrm{dR}}\widehat{\mathbf{p}} = -\left(\boldsymbol{\Delta}^{\mathrm{RR}} + \boldsymbol{\Delta}^{\mathrm{GD}}\right)\widehat{\mathbf{p}} \tag{2.14}$$

with $\boldsymbol{\Delta}^{\mathrm{RR}}\widehat{\mathbf{p}} = \mathrm{Rot}_{\mathcal{S}}\,\mathrm{rot}_{\mathcal{S}}\,\widehat{\mathbf{p}}$ and $\boldsymbol{\Delta}^{\mathrm{GD}}\widehat{\mathbf{p}} = \nabla_{\mathcal{S}}\left(\mathrm{div}_{\mathcal{S}}\,\widehat{\mathbf{p}}\right)$. Again, we use the same symbols for the Laplacians in the local and the Cartesian representation of the vector field $\mathbf{p}$.

For further details on geometric calculus – especially for covariant differentiation in local coordinates – we refer to [AMR88, NVW12, NRV18, NNP$^+$18, NRV17] and especially to [NV18] for the moving surface setting.

2.3 Basic concepts for the appearance of defects

2.3.1 Topological constraints

One mechanism for the appearance of defects is a topological constraint. Consider a triangulation of the surface $\mathcal{S}$. Although the Gaussian curvature κ is a local geometric property, when integrated over $\mathcal{S}$ it becomes a topological invariant, namely the Euler characteristic $\chi(\mathcal{S})$, which is stated in the Gauss-Bonnet theorem, i. e.

$$\chi(\mathcal{S}) = \frac{1}{2\pi}\int_{\mathcal{S}}\kappa\mathrm{d}\mathcal{S}\,. \tag{2.15}$$

Thereby, the Euler characteristic $\chi(\mathcal{S})$ is defined by

$$\chi(\mathcal{S}) := V + F - E \tag{2.16}$$

with the number of vertices V, the number of faces F and the number of edges E of the triangulation. Equations (2.15) and (2.16) form a relation between the triangulation and the Gaussian curvature κ. E. g. for a sphere with radius R, the (constant) Gaussian curvature is $1/R^2$ and the surface area is $4\pi R^2$, which yields $\chi(\mathcal{S}) = 2$ according to equation (2.15). For the i-th vertex of the triangulation,

we can assign a coordination number C_i, counting the number of edges at that point. Each edge connects two vertices. On the other hand, the i-th vertex also connects C_i faces, where each connects three vertices. Thus, the contribution of the i-th vertex to $\chi(\mathcal{S})$ can be written as $1 - C_i/2 + C_i/3 = (6 - C_i)/6$ according to equation (2.16). Hence, vertices with a coordination number $C_i = 6$ do not contribute and we can sum over all defects ($C_i \neq 6$) and obtain

$$\sum_i \frac{\mathrm{ind}_S(\mathbf{d}_i)}{6} = \chi(\mathcal{S}) \tag{2.17}$$

with $\mathrm{ind}_S(\mathbf{d}_i) := 6 - C_i$ the defect charge at defect position $\mathbf{d}_i$. This can be related to our soccer ball example from Section 2.1. Each of the black and white face is replaced by a vertex, which is located in the center of the pentagon/hexagon and is connected to the neighboring vertices by an edge. This forms triangular faces and thus we find 12 vertices with charge $+1$.

Similar arguments hold for continuous vector fields on closed surfaces. Also in this case the Euler characteristic can be used to understand the defects. Here, the charge of a defect is no longer determined by its coordination number $\mathrm{ind}_S(\cdot)$, but by its index/winding number $\mathrm{ind}_V(\cdot)$, which is the algebraic sum of the number of revolution of the vector field along a small counterclockwise oriented curve around the defect. Thus, we state the Poincaré-Hopf theorem

$$\sum_i \mathrm{ind}_V(\mathbf{d}_i) = \chi(\mathcal{S}) \,. \tag{2.18}$$

Equation (2.18) shows, that any continuous vector field on a sphere must have at least two $+1$ defects or one $+2$ defect. E. g., consider the lines of latitude on the globe that naturally create two vortices ($+1$ defects) at the north and south pole, which yields a realization of the Poincaré-Hopf theorem (2.18). For a more detailed discussion we refer to, e. g., [Kam02]. Additionally, the Euler characteristic is related to the genus $g(\mathcal{S})$ of the surface $\mathcal{S}$ by

$$\chi(\mathcal{S}) = 2 - 2g(\mathcal{S}) \,,$$

where $g(\mathcal{S})$ is formally defined as the number of handles of the surface $\mathcal{S}$. Thus,

an alternative version of the Poincaré-Hopf theorem is given by

$$\sum_i \operatorname{ind}_V(\mathbf{d}_i) = 2 - 2g(\mathcal{S})\,. \tag{2.19}$$

2.3.2 Geometric potential

The topology of the surface is one source for the appearance of defects and the total topological charge of all defects is a conserved quantity. However, the realization of equations (2.17) and (2.18) and the defect positions are not determined by topology, but result from other sources, such as geometric properties.

Each defect experiences a geometric potential, which reflects the broken translational invariance of the surface and the type of order in the film or the alignment of the vector field with the surface. In all these cases, defects can be related to the geometry by an effective geometric interaction [VT04], which reads in the case of the triangulated surface

$$\mathcal{E}_S(\mathbf{d}_i) = -\pi k_e \operatorname{ind}_S(\mathbf{d}_i)^2 U_G(\mathbf{d}_i) \tag{2.20}$$

and in the case of a continuous vector field

$$\mathcal{E}_V(\mathbf{d}_i) = 2\pi k_e \operatorname{ind}_V(\mathbf{d}_i) \left(1 - \frac{\operatorname{ind}_V(\mathbf{d}_i)}{2}\right) U_G(\mathbf{d}_i) \tag{2.21}$$

with elastic stiffness k_e and geometric potential U_G determined by the surface Poisson equation

$$\Delta_{\mathcal{S}} U_G = \kappa\,.$$

The linear term in equation (2.21) arises from the geometric frustration of a vector field, while the quadratic term in equations (2.20) and (2.21) originates from the distortion of a vortex's own flow pattern by the geometry. This self-interaction is analyzed in detail for superfluid helium in [TVN10]. For this case, analytic expressions can be derived for the interaction of vortices with the geometry showing, e. g., a repulsion of vortices from positive Gaussian curvature and an attraction to negative Gaussian curvature regions, irrespective of their

charge and sign. The situation changes if the linear contribution comes into play. The defects still place themselves such that the Gaussian curvature is screened. More precisely, positive defects are attracted to peaks and valleys while negative defects are pulled to saddles of the surface [VN06].

2.3.3 Defect interactions

In addition to the interaction with the geometry, defects also interact with each other. Like particles, defects interact due to its charge via a Coulomb-like interaction. This results in our two illustrative examples of a soccer ball and the globe in a repulsion of the defects and a realization in which the geodesic distance between the defects is maximized.

2.3.4 Nonlinear interactions and hydrodynamics

Combining all three contributions leads to a highly nonlinear interaction of topology, geometry and defect positions. While this mesoscopic approach is very efficient and successful in determining stable configurations (at least for simple geometries), it neglects other influences for the appearance of defects, which are caused by hydrodynamics. Therefore, we consider a full dynamic model and use the described approaches only to justify the chosen examples and to demonstrate the interaction of the flow field with the geometry. Instead of a superfluid, where dissipation mechanisms of a conventional fluid are absent, we consider the incompressible surface Navier-Stokes equation for which the above mentioned interactions are used as suggestive analogies in order to show that similar interactions can also be found in that case.

2.4 General vector-valued PDEs on evolving surfaces

In this section, we propose a general approach to rewrite locally defined vector-valued surface PDEs in the Euclidean basis, which is a starting point for further

numerical approaches. We will see, that this opens the possibility to use established methods, such as the standard surface finite element method.

In the literature, a lot of work has been done on the class of general scalar-valued surface PDEs, e. g. in [Dzi88, DE07a, DE07b, DE13], whereas for vector-valued surface PDEs only very recent approaches have been proposed, e. g. in [RV18b, NNPV18, NNP$^+$18, NRV18, OQRY18, HLL16]. In [NNV18] a finite element method for arbitrary tensor-valued surface PDEs is proposed, which uses the representation of the equations in the Euclidean basis. Here, we will use the same basic ideas in order to reformulate vector-valued surface PDEs on moving surfaces. Thus, consider a general local vector-valued surface PDE of the form

$$\bar{\partial}_t \mathbf{p} = \boldsymbol{F}(\mathbf{p}, \boldsymbol{\Delta}^{\mathrm{dR}} \mathbf{p}) \qquad (2.22)$$

on $\mathcal{S} = \mathcal{S}(t)$ with initial condition $\mathbf{p}(\cdot, t)|_{t=0} = \mathbf{p}_0(\cdot)$. Thereby, $\mathbf{p} = \mathbf{p}_i \partial_i \mathbf{x} \in \mathsf{T}^{(1)}\mathcal{S}$ denotes a vector field and $\bar{\partial}_t \mathbf{p} := (\partial_t \mathbf{p}_i)\, \partial_i \mathbf{x}$ the so-called intrinsic time derivative. For simplicity the right hand side $\boldsymbol{F}$ only depends on zero and second order contributions of $\mathbf{p}$. Note that we restrict to the Laplace-deRham operator $\boldsymbol{\Delta}^{\mathrm{dR}}$ in equation (2.22) since the Bochner Laplacian $\boldsymbol{\Delta}^{\mathrm{B}}$ can be expressed via the Laplace-deRham operator $\boldsymbol{\Delta}^{\mathrm{dR}}$ in connection with the Gaussian curvature κ through the Weizenböck identity (2.12).

The intrinsic time derivative in equation (2.22) is embarrassing for the most of the numerical tools to solve vector-valued surface PDEs, since they are not able to work with a local vector basis. To be more precise, solving such equations is typically done by considering the vectors in the Euclidean basis and considering the vector-valued equation as system of coupled scalar surface PDEs for each component. We follow [NRV18] and define $\partial_t \mathbf{p} := \partial_t (\mathbf{p}_i \partial_i \mathbf{x})$, which would be more appropriate than $\bar{\partial}_t \mathbf{p} = (\partial_t \mathbf{p}_i)\, \partial_i \mathbf{x}$ as in the above equation (2.22). By using the product rule, we obtain $\partial_t \mathbf{p} = (\partial_t \mathbf{p}_i)\, \partial_i \mathbf{x} + \mathbf{p}_i \partial_i \partial_t \mathbf{x} = \bar{\partial}_t \mathbf{p} + \mathbf{p}_i \partial_i \partial_t \mathbf{x}$ and therefore a relation between $\partial_t \mathbf{p}$ and $\bar{\partial}_t \mathbf{p}$. Generally, $\partial_t \mathbf{p}$ does not belong to the tangential space of the surface $\mathcal{S}$ and therefore only the tangential part of $\partial_t \mathbf{p}$ is considered. This means, the i-th contravariant component of $\partial_t \mathbf{p}$ reads $[\partial_t \mathbf{p}]_i = [\boldsymbol{g}^{-1}]_{ij}\, \partial_t \mathbf{p} \cdot \partial_i \mathbf{x} = [\boldsymbol{g}^{-1}]_{ij} \left(\boldsymbol{g}_{jk} \partial_t \mathbf{p}_k - v_{\boldsymbol{\nu}} \boldsymbol{g}_{jk} \mathcal{B}_{kl} \mathbf{p}_l \right)$ which results in $\bar{\partial}_t \mathbf{p} = \boldsymbol{\pi} \partial_t \mathbf{p} + v_{\boldsymbol{\nu}} \mathcal{B} \mathbf{p}$. For more details we refer to [NV18, NRV18]. Accordingly, equation

(2.22) now reads

$$\boldsymbol{\pi}\partial_t\mathbf{p} + v_\nu\mathcal{B}\mathbf{p} = \boldsymbol{F}(\mathbf{p}, \boldsymbol{\Delta}^{\mathrm{dR}}\mathbf{p}) \, . \tag{2.23}$$

Next, we extend the local basis by a coordinate in the normal direction and consider the Euclidean basis as in Section 2.2.2. Thus, let $\widehat{\mathbf{p}}$ be the Cartesian representation of the corresponding local vector $\mathbf{p}$. Note that $\widehat{\mathbf{p}}$ is not necessarily tangential. The newly added normal coordinate yields an additional degree of freedom and equation (2.23) rewritten for $\widehat{\mathbf{p}}$ results in an under-determined problem. This issue can be handled in various ways. One possibility is the introduce a Lagrange multiplier to enforce a zero normal component, which has been considered in, e. g., [JOR17]. But this is not the focus of this work, since the arising equations have saddle point structure and the numerical methods require more care. Therefore, we here follow a penalty approach which uses an additional penalty term in the equation to enforce the normal component to be zero in a weak sense, cf. [NNPV18, RV18b]. Thus, equation (2.23) rewritten in Cartesian coordinates reads

$$\boldsymbol{\pi}\partial_t\widehat{\mathbf{p}} + v_\nu\mathcal{B}\widehat{\mathbf{p}} = \boldsymbol{F}(\widehat{\mathbf{p}}, \boldsymbol{\Delta}^{\mathrm{dR}}\widehat{\mathbf{p}}) \pm \alpha(\widehat{\mathbf{p}}\cdot\boldsymbol{\nu})\boldsymbol{\nu} \, , \tag{2.24}$$

with initial condition $\widehat{\mathbf{p}}\left(\cdot, t\right)\big|_{t=0} = \widehat{\mathbf{p}}_0(\cdot)$ and a typically large penalty parameter α. The sign in front of the penalty term corresponds with the sign in front of the Laplace-deRham operator. It was shown in [NNPV18] that $\boldsymbol{\Delta}^{\mathrm{dR}}\mathbf{v} \approx \boldsymbol{\Delta}^{\mathrm{dR}}\widehat{\mathbf{v}}$ if the penalization technique from above is applied. Furthermore, first order convergence in α was numerically shown for various physical problems in [NNPV18, RV18b].

Eq. (2.24) can now be treated componentwise and established methods for solving surface PDEs – such as the surface finite element method [DE13] – can be applied. We will use these technique in some of the following chapters in order to directly solve the incompressible surface Navier-Stokes equation and an vector-valued equation for oriented ordering on evolving surfaces, see Chapter 4 and Chapter 6.

2.5 Incompressible surface Navier-Stokes equation

2.5.1 Literature

One of the first occurrence of the incompressible surface Navier-Stokes equation dates back to the 1960s where Scriven published his fundamental work on incompressible Newtonian fluids on evolving surfaces in [Scr60]. In [AD09] this formulation is used to describe the influence of the membrane viscosity effect in liquid membranes. These models are based on basic conservation laws, i. e. mass and linear momentum conservation. It turned out that the formulation of the interfacial fluid – especially the acceleration term – in [Scr60] and [AD09] is wrong, which has been corrected recently by [YOS16]. Here, the incompressible surface Navier-Stokes equation is derived by variation of the kinetic energy of a moving manifold and using the Lagrange-d'Alembert principle. Other approaches, which correctly derive the equations, can be found in [DF96], where the Rayleigh dissipation potential is minimized, and in [HZE07], where rigorous covariant differentiation is used. Recently, the correct formulation on moving surfaces is derived by a thin-film limit of the three-dimensional incompressible Navier-Stokes equation in [Miu17], by using basic conservation laws in [JOR17] and by applying a variational principle in [KLG17]. All of these models are restricted to Cartesian coordinates and consider a three-dimensional velocity vector field in the Euclidean space. Very recently, in [NRV18] a thin film limit of the three-dimensional incompressible Navier-Stokes equation is performed to achieve the correct formulation in covariant form.

The formulation on stationary surfaces is discussed in [Tem88, CRT99], but with the wrong factor in front of the term including the Gaussian curvature. The correct formulation can be found in [EM70, MT01, RV18b], for which the property of a dissipative system was analytically shown in [NRV17]. A vorticity-stream function approach was derived in [NVW12], which is used in [NRV17] and extended to evolving surfaces in [RV15, RV18a]. In [GA18] the equation is derived by using a variational approach and exterior calculus.

Applications   The incompressible surface Navier-Stokes equation is connected to the Boussinesq-Scriven constitutive law for two-phase flow problems with interfacial viscous dissipation, see e. g. [Scr60, SS82, BP10, BGN15a]. Applications can be found in [HZE07, AD09, FHH10, BGN15a, RV16], where the properties and dynamics of biomembranes were discussed, in computer graphics [ETK+07, MCP+09, VCD+16] and in geophysics [STY15, PGRPV17]. Additionally, the dynamics of plasma motion in fusion plasma physics is of special interest, see e. g. [Boo05].

Numerical approaches   Methods to numerically solve the incompressible surface Navier-Stokes equation are rare in the mathematical literature. The vorticity-stream function approach [NVW12, RV15, RV18a] allows to use standard techniques for scalar-valued surface PDEs, such as the surface finite element method [DE07a, DE07b, DE13] or the diffuse interface method [RV06]. The latter was extensively used in [RV16]. Other numerical approaches, which take the incompressible surface Navier-Stokes equation in its vector-valued form into account, can be found in [MHS16], but with the missing term including the Gaussian curvature, and in [NRV17]. Both approaches are based in discrete exterior calculus (DEC). In [GA18] a spectral numerical method is proposed to numerically solve the equations on radial manifold shapes. The incompressible surface Navier-Stokes equation is rewritten in Cartesian coordinates in [RV18b, NRV18] and the standard surface finite element method [DE07a, DE07b, DE13] is used to solve the equations componentwise. A similar technique is proposed in [JOR17] for the surface Stokes problem.

2.5.2 Derivation

In the following, we briefly sketch a possibility to derive the incompressible surface Navier-Stokes equation from the mass conservation law and a modification of the linear momentum conservation law, which is proposed in [YOS16]. The purpose of this modification is that the derivation is independent of the choice of the coordinate system, while the derivation in, e. g., [JOR17] is restricted to the Cartesian coordinate system. To start with we state the following lemma

adapted from [YOS16, Appendix 2].

Lemma 1 (Master balance equation, [YOS16]). *Let $\psi, \eta \in \mathsf{T}^{(0)}\mathcal{S}$ are given scalar functions and let $\mathbf{p} \in \mathsf{T}^{(1)}\mathcal{S}$ be a vector field on the surface $\mathcal{S}$. Furthermore, let hold the balance law*

$$\frac{\mathrm{d}}{\mathrm{d}t} \int_{\mathcal{U}} \psi \mathrm{d}s = \int_{\mathcal{U}} \eta \mathrm{d}s + \int_{\partial\mathcal{U}} \langle \mathbf{p}, \boldsymbol{\nu}_T \rangle \mathrm{d}a$$

for any open subset $\mathcal{U} = \mathcal{U}(t) \subset \mathcal{S} = \mathcal{S}(t)$ with sufficiently smooth boundary, $\boldsymbol{\nu}_T$ the normal vector on $\partial\mathcal{U}$ and $\frac{\mathrm{d}}{\mathrm{d}t}$ the material derivative. Then, localization yields the partial differential equation

$$\frac{\mathrm{d}}{\mathrm{d}t}\psi + \psi \operatorname{div}_{\mathcal{S}} \mathbf{v} - \psi v_{\boldsymbol{\nu}}\mathcal{H} = \eta + \operatorname{div}_{\mathcal{S}} \mathbf{p}\,.$$

Thereby, $\mathbf{v}$ denotes the tangential velocity of the surface $\mathcal{S}$.

Conservation of mass   The conservation of mass reads in integral form

$$\frac{\mathrm{d}}{\mathrm{d}t} \int_{\mathcal{U}} \rho_{\mathcal{S}} \mathrm{d}s = 0$$

for any open subset $\mathcal{U} \subset \mathcal{S} = \mathcal{S}(t)$ with the surface material density $\rho_{\mathcal{S}}$. Using Lemma 1 with $\psi = \rho_{\mathcal{S}}$, $\eta = 0$ and $\mathbf{p} = 0$ yields the localized conservation of mass

$$\frac{\mathrm{d}}{\mathrm{d}t}\rho_{\mathcal{S}} + \rho_{\mathcal{S}} \operatorname{div}_{\mathcal{S}} \mathbf{v} - \rho_{\mathcal{S}} v_{\boldsymbol{\nu}}\mathcal{H} = 0\,.$$

Modified tangential balance of linear momentum   In flat space the balance of linear momentum is a vector-valued integral equation. This can be generalized to surfaces if Cartesian coordinates are used, see e. g. [JOR17]. In the more general context of an arbitrary coordinate system this is no longer possible. If we analogously state the balance equation in an arbitrary local coordinate system componentwise, we would lose the frame invariance of the whole system. Roughly speaking, for two different choices of the coordinate system we get two different equations in general. Thus, we modify this law by contracting

with an arbitrary time-independent and covariantly time-constant test vector field $\mathbf{u}$ tangent to $\mathcal{U}$ [YOS16]. Accordingly, the modified tangential balance of linear momentum reads

$$\frac{\mathrm{d}}{\mathrm{d}t}\int_{\mathcal{U}}\langle\rho_{\mathcal{S}}\mathbf{v},\mathbf{u}\rangle\mathrm{d}s = \int_{\mathcal{U}}\langle\mathbf{f},\mathbf{u}\rangle\mathrm{d}s + \int_{\partial\mathcal{U}}\langle\boldsymbol{\sigma}\boldsymbol{\nu}_{T},\mathbf{u}\rangle\mathrm{d}a \qquad (2.25)$$

with external forces $\mathbf{f}$ and surface stress tensor $\boldsymbol{\sigma} = -p\,\mathrm{id}_{\mathcal{S}} + 2\eta_{\mathcal{S}}\mathbf{d}$. Thereby, p denotes the pressure, $\mathrm{id}_{\mathcal{S}}$ the surface identity and $\mathbf{d}$ the rate-of-strain tensor, i. e.

$$\mathbf{d} = \frac{1}{2}\left(\nabla_{\mathcal{S}}\mathbf{v} + (\nabla_{\mathcal{S}}\mathbf{v})^{T}\right) - v_{\nu}\mathcal{B}\,,$$

see [AD09]. It holds $\langle\boldsymbol{\sigma}\boldsymbol{\nu}_{T},\mathbf{u}\rangle = \langle\boldsymbol{\nu}_{T},\boldsymbol{\sigma}\mathbf{u}\rangle$ due to the symmetry of the stress tensor $\boldsymbol{\sigma}$. Hence, Lemma 1 can be applied to equation (2.25) with $\psi = \langle\rho_{\mathcal{S}}\mathbf{v},\mathbf{u}\rangle$, $\eta = \langle\mathbf{f},\mathbf{u}\rangle$, $\mathbf{p} = \boldsymbol{\sigma}\mathbf{u}$ and thus localization yields

$$\frac{\mathrm{d}}{\mathrm{d}t}\langle\rho_{\mathcal{S}}\mathbf{v},\mathbf{u}\rangle + \langle\rho_{\mathcal{S}}\mathbf{v},\mathbf{u}\rangle\operatorname{div}_{\mathcal{S}}\mathbf{v} - \langle\rho_{\mathcal{S}}\mathbf{v},\mathbf{u}\rangle v_{\nu}\mathcal{H} = \langle\mathbf{f},\mathbf{u}\rangle + \operatorname{div}_{\mathcal{S}}\left(\boldsymbol{\sigma}\mathbf{u}\right)\,.$$

With the product rule $\frac{\mathrm{d}}{\mathrm{d}t}\langle\rho_{\mathcal{S}}\mathbf{v},\mathbf{u}\rangle = \left(\frac{\mathrm{d}}{\mathrm{d}t}\rho_{\mathcal{S}}\right)\langle\mathbf{v},\mathbf{u}\rangle + \rho_{\mathcal{S}}\langle\frac{\mathrm{d}}{\mathrm{d}t}\mathbf{v},\mathbf{u}\rangle$ we obtain

$$\left(\frac{\mathrm{d}}{\mathrm{d}t}\rho_{\mathcal{S}} + \rho_{\mathcal{S}}\operatorname{div}_{\mathcal{S}}\mathbf{v} - \rho_{\mathcal{S}}v_{\nu}\mathcal{H}\right)\langle\mathbf{v},\mathbf{u}\rangle + \rho_{\mathcal{S}}\langle\frac{\mathrm{d}}{\mathrm{d}t}\mathbf{v},\mathbf{u}\rangle = \langle\mathbf{f},\mathbf{u}\rangle + \operatorname{div}_{\mathcal{S}}\left(\boldsymbol{\sigma}\mathbf{u}\right)\,.$$

The term in the first brackets on the left hand side is the localized conservation of mass and therefore vanishes identically. Thus, by using the arbitrariness of $\mathbf{u}$ and the correct acceleration term from [HZE07] or [YOS16], i. e. $\frac{\mathrm{d}}{\mathrm{d}t}\mathbf{v} = \bar{\partial}_{t}\mathbf{v} + \boldsymbol{\nabla}_{\mathbf{v}}\mathbf{v} - 2v_{\nu}\mathcal{B}\mathbf{v} - v_{\nu}\nabla_{\mathcal{S}}v_{\nu}$, we obtain

$$\rho_{\mathcal{S}}\left(\bar{\partial}_{t}\mathbf{v} + \boldsymbol{\nabla}_{\mathbf{v}}\mathbf{v} - 2v_{\nu}\mathcal{B}\mathbf{v} - v_{\nu}\nabla_{\mathcal{S}}v_{\nu}\right) = \operatorname{div}_{\mathcal{S}}\boldsymbol{\sigma} + \mathbf{f}\,,$$

where we recall the intrinsic time derivative $\bar{\partial}_{t}\mathbf{v} = \left(\partial_{t}\mathbf{v}_{i}\right)\partial_{i}\mathbf{x}$ from above. We further assume the surface density $\rho_{\mathcal{S}}$ to be constant in space and time. Follow-

ing [AD09], the divergence of the rate-of-strain tensor can be evaluated as

$$2 \operatorname{div}_{\mathcal{S}} \mathbf{d} = \underbrace{\operatorname{div}_{\mathcal{S}} (\nabla_{\mathcal{S}} \mathbf{v})}_{=-\boldsymbol{\Delta}^{\mathrm{dR}} \mathbf{v} + \kappa \mathbf{v}} + \underbrace{\operatorname{div}_{\mathcal{S}} \left((\nabla_{\mathcal{S}} \mathbf{v})^T \right)}_{=\nabla_{\mathcal{S}} (\operatorname{div}_{\mathcal{S}} \mathbf{v}) + \kappa \mathbf{v}} - 2 \operatorname{div}_{\mathcal{S}} (v_{\boldsymbol{\nu}} \mathcal{B})$$
$$= -\boldsymbol{\Delta}^{\mathrm{dR}} \mathbf{v} + 2\kappa \mathbf{v} + \nabla_{\mathcal{S}} (v_{\boldsymbol{\nu}} \mathcal{H}) - 2 \operatorname{div}_{\mathcal{S}} (v_{\boldsymbol{\nu}} \mathcal{B})$$

and by using the identity $\bar{\partial}_t \mathbf{v} = \boldsymbol{\pi} \partial_t \mathbf{v} + v_{\boldsymbol{\nu}} \mathcal{B} \mathbf{v}$ from Section 2.4 the incompressible surface Navier-Stokes equation finally reads

$$\rho_{\mathcal{S}} (\boldsymbol{\pi} \partial_t \mathbf{v} + \boldsymbol{\nabla}_{\mathbf{v}} \mathbf{v} - v_{\boldsymbol{\nu}} \mathcal{B} \mathbf{v} - v_{\boldsymbol{\nu}} \nabla_{\mathcal{S}} v_{\boldsymbol{\nu}}) = -\nabla_{\mathcal{S}} p + \eta_{\mathcal{S}} \left(-\boldsymbol{\Delta}^{\mathrm{dR}} \mathbf{v} + 2\kappa \mathbf{v} \right)$$
$$+ \eta_{\mathcal{S}} \left(-2 \operatorname{div}_{\mathcal{S}} (v_{\boldsymbol{\nu}} \mathcal{B}) + \nabla_{\mathcal{S}} (v_{\boldsymbol{\nu}} \mathcal{H}) \right)$$
$$+ \mathbf{f} \tag{2.26}$$
$$\operatorname{div}_{\mathcal{S}} \mathbf{v} - v_{\boldsymbol{\nu}} \mathcal{H} = 0 \tag{2.27}$$

with the initial condition $\mathbf{v} (\cdot, t) |_{t=0} = \mathbf{v}_0(\cdot)$.

2.5.3 Nondimensionalization and Cartesian extension

We denote nondimensional variables/quantities and differential operators by a "$\sim$" over its symbol. Let l^* be a given length scale and t^* a given time scale. By using the identities from Table 2.1, we obtain for equations (2.26) and (2.27)

$$\frac{\rho_{\mathcal{S}} l^*}{t^{*2}} \left(\widetilde{\boldsymbol{\pi}} \widetilde{\partial}_t \widetilde{\mathbf{v}} + \widetilde{\boldsymbol{\nabla}}_{\widetilde{\mathbf{v}}} \widetilde{\mathbf{v}} - \widetilde{v}_{\boldsymbol{\nu}} \widetilde{\mathcal{B}} \widetilde{\mathbf{v}} - \widetilde{v}_{\boldsymbol{\nu}} \widetilde{\nabla}_{\mathcal{S}} \widetilde{v}_{\boldsymbol{\nu}} \right) = -\frac{\rho_{\mathcal{S}} l^*}{t^{*2}} \widetilde{\nabla}_{\mathcal{S}} \widetilde{p} + \frac{\eta_{\mathcal{S}}}{l^* t^*} \left(-\widetilde{\boldsymbol{\Delta}}^{\mathrm{dR}} \widetilde{\mathbf{v}} + 2\widetilde{\kappa} \widetilde{\mathbf{v}} \right)$$
$$+ \frac{\eta_{\mathcal{S}}}{l^* t^*} \widetilde{\nabla}_{\mathcal{S}} \left(\widetilde{v}_{\boldsymbol{\nu}} \widetilde{\mathcal{H}} \right)$$
$$- \frac{2\eta_{\mathcal{S}}}{l^* t^*} \widetilde{\operatorname{div}}_{\mathcal{S}} \left(\widetilde{v}_{\boldsymbol{\nu}} \widetilde{\mathcal{B}} \right) + \frac{\rho_{\mathcal{S}} l^*}{t^{*2}} \widetilde{\mathbf{f}}$$
$$\frac{1}{t^*} \widetilde{\operatorname{div}}_{\mathcal{S}} \widetilde{\mathbf{v}} - \frac{1}{t^*} \widetilde{v}_{\boldsymbol{\nu}} \widetilde{\mathcal{H}} = 0 \,.$$

For convenience and for better readability we drop the "$\sim$"-notation from now on and consider each variable, quantity and operator in its nondimensional form (unless otherwise stated). Thus, we get by further manipulation and by using the definition of the Reynolds number $\mathrm{Re} := \frac{\rho_{\mathcal{S}} l^{*2}}{\eta_{\mathcal{S}} t^*}$ the nondimensional form of

Symbol	nondimensional counterpart	Symbol	nondimensional counterpart
∂_t	$\frac{1}{t^*}\widetilde{\partial}_t$	$v_{\boldsymbol{\nu}}$	$\frac{l^*}{t^*}\widetilde{v}_{\boldsymbol{\nu}}$
$\nabla_{\mathcal{S}}$	$\frac{1}{l^*}\widetilde{\nabla}_{\mathcal{S}}$	$\boldsymbol{\nu}$	$\widetilde{\boldsymbol{\nu}}$
$\mathrm{div}_{\mathcal{S}}$	$\frac{1}{l^*}\widetilde{\mathrm{div}}_{\mathcal{S}}$	$\boldsymbol{\pi}$	$\widetilde{\boldsymbol{\pi}}$
$\boldsymbol{\Delta}^{\mathrm{dR}}$	$\frac{1}{l^{*2}}\widetilde{\boldsymbol{\Delta}}^{\mathrm{dR}}$	$\mathcal{B}$	$\frac{1}{l^*}\widetilde{\mathcal{B}}$
$\boldsymbol{\nabla}$	$\frac{1}{l^*}\widetilde{\boldsymbol{\nabla}}$	$\mathcal{H}$	$\frac{1}{l^*}\widetilde{\mathcal{H}}$
$\mathbf{v}$	$\frac{l^*}{t^*}\widetilde{\mathbf{v}}$	κ	$\frac{1}{l^{*2}}\widetilde{\kappa}$
p	$\frac{\rho_{\mathcal{S}}l^{*2}}{t^{*2}}\widetilde{p}$	$\mathbf{f}$	$\frac{\rho_{\mathcal{S}}l^*}{t^{*2}}\widetilde{\mathbf{f}}$

Table 2.1: Variables, quantities and differential operators in dimensional and nondimensional form.

the incompressible surface Navier-Stokes equation (2.26)-(2.27)

$$\boldsymbol{\pi}\partial_t\mathbf{v} + \boldsymbol{\nabla}_{\mathbf{v}}\mathbf{v} - v_{\boldsymbol{\nu}}\mathcal{B}\mathbf{v} - v_{\boldsymbol{\nu}}\nabla_{\mathcal{S}}v_{\boldsymbol{\nu}} = -\nabla_{\mathcal{S}}p + \frac{1}{\mathrm{Re}}\left(-\boldsymbol{\Delta}^{\mathrm{dR}}\mathbf{v} + 2\kappa\mathbf{v} + \nabla_{\mathcal{S}}\left(v_{\boldsymbol{\nu}}\mathcal{H}\right)\right)$$

$$- \frac{2}{\mathrm{Re}}\,\mathrm{div}_{\mathcal{S}}\left(v_{\boldsymbol{\nu}}\mathcal{B}\right) + \mathbf{f} \tag{2.28}$$

$$\mathrm{div}_{\mathcal{S}}\mathbf{v} - v_{\boldsymbol{\nu}}\mathcal{H} = 0\,. \tag{2.29}$$

Next, we propose an alternative formulation of the divergence of the surface stress tensor in its nondimensional form, i. e. the viscous terms in equation (2.28), which is sometimes more convenient to use. As above, we follow [AMR88] and use the definition of the Laplace-deRham operator $\boldsymbol{\Delta}^{\mathrm{dR}}\mathbf{v} = -\mathrm{Rot}_{\mathcal{S}}\mathrm{rot}_{\mathcal{S}}\mathbf{v} - \nabla_{\mathcal{S}}\left(\mathrm{div}_{\mathcal{S}}\mathbf{v}\right)$. Furthermore, we use the identity $\mathrm{div}_{\mathcal{S}}\mathcal{B} = \nabla_{\mathcal{S}}\mathcal{H}$, the localized conservation of mass as well as the product rule and rewrite the viscous terms as

$$\begin{aligned}\mathrm{div}_{\mathcal{S}}\,\boldsymbol{\sigma} &= -\boldsymbol{\Delta}^{\mathrm{dR}}\mathbf{v} + 2\kappa\mathbf{v} + \nabla_{\mathcal{S}}\left(v_{\boldsymbol{\nu}}\mathcal{H}\right) - 2\,\mathrm{div}_{\mathcal{S}}\left(v_{\boldsymbol{\nu}}\mathcal{B}\right)\\ &= \mathrm{Rot}_{\mathcal{S}}\mathrm{rot}_{\mathcal{S}}\mathbf{v} + 2\kappa\mathbf{v} + 2\nabla_{\mathcal{S}}\left(v_{\boldsymbol{\nu}}\mathcal{H}\right) - 2\mathcal{B}\nabla_{\mathcal{S}}v_{\boldsymbol{\nu}} - 2v_{\boldsymbol{\nu}}\,\mathrm{div}_{\mathcal{S}}\mathcal{B}\\ &= \mathrm{Rot}_{\mathcal{S}}\mathrm{rot}_{\mathcal{S}}\mathbf{v} + 2\kappa\mathbf{v} + 2\mathcal{H}\nabla_{\mathcal{S}}v_{\boldsymbol{\nu}} - 2\mathcal{B}\nabla_{\mathcal{S}}v_{\boldsymbol{\nu}}\,. \end{aligned} \tag{2.30}$$

Thus, an alternative form of the incompressible surface Navier-Stokes equation

(2.28)-(2.29) reads

$$\boldsymbol{\pi}\partial_t \mathbf{v} + \boldsymbol{\nabla}_{\mathbf{v}}\mathbf{v} - v_{\boldsymbol{\nu}}\mathcal{B}\mathbf{v} - v_{\boldsymbol{\nu}}\nabla_{\mathcal{S}}v_{\boldsymbol{\nu}} = -\nabla_{\mathcal{S}}p + \frac{1}{\mathrm{Re}}\left(\mathrm{Rot}_{\mathcal{S}}\,\mathrm{rot}_{\mathcal{S}}\,\mathbf{v} + 2\kappa\mathbf{v} + 2\mathcal{H}\nabla_{\mathcal{S}}v_{\boldsymbol{\nu}}\right)$$

$$- \frac{2}{\mathrm{Re}}\mathcal{B}\nabla_{\mathcal{S}}v_{\boldsymbol{\nu}} + \mathbf{f} \tag{2.31}$$

$$\mathrm{div}_{\mathcal{S}}\,\mathbf{v} - v_{\boldsymbol{\nu}}\mathcal{H} = 0\,. \tag{2.32}$$

In order to use established numerical methods to solve the incompressible surface Navier-Stokes equation (2.28)-(2.29) or the alternative version (2.31)-(2.32), we extend the equations to Cartesian coordinates and penalize the normal component to be zero in a weak sense as proposed in Section 2.4. Thus, the system (2.28)-(2.29) now reads

$$\boldsymbol{\pi}\partial_t \widehat{\mathbf{v}} + \boldsymbol{\nabla}_{\widehat{\mathbf{v}}}\widehat{\mathbf{v}} - v_{\boldsymbol{\nu}}\mathcal{B}\widehat{\mathbf{v}} - v_{\boldsymbol{\nu}}\nabla_{\mathcal{S}}v_{\boldsymbol{\nu}} = -\nabla_{\mathcal{S}}p + \frac{1}{\mathrm{Re}}\left(-\boldsymbol{\Delta}^{\mathrm{dR}}\widehat{\mathbf{v}} + 2\kappa\widehat{\mathbf{v}} + \nabla_{\mathcal{S}}\left(v_{\boldsymbol{\nu}}\mathcal{H}\right)\right)$$

$$- \frac{2}{\mathrm{Re}}\,\mathrm{div}_{\mathcal{S}}\left(v_{\boldsymbol{\nu}}\mathcal{B}\right) + \widehat{\mathbf{f}} - \alpha_{\mathbf{v}}\left(\widehat{\mathbf{v}}\cdot\boldsymbol{\nu}\right)\boldsymbol{\nu} \tag{2.33}$$

$$\mathrm{div}_{\mathcal{S}}\,\widehat{\mathbf{v}} - v_{\boldsymbol{\nu}}\mathcal{H} = 0\,, \tag{2.34}$$

where $\widehat{\mathbf{f}}$ denotes the extended three-component external forces. Analogously, the extended version of the alternative formulation (2.31)-(2.32) reads

$$\boldsymbol{\pi}\partial_t \widehat{\mathbf{v}} + \boldsymbol{\nabla}_{\widehat{\mathbf{v}}}\widehat{\mathbf{v}} - v_{\boldsymbol{\nu}}\mathcal{B}\widehat{\mathbf{v}} - v_{\boldsymbol{\nu}}\nabla_{\mathcal{S}}v_{\boldsymbol{\nu}} = -\nabla_{\mathcal{S}}p + \frac{1}{\mathrm{Re}}\left(\mathrm{Rot}_{\mathcal{S}}\,\mathrm{rot}_{\mathcal{S}}\,\widehat{\mathbf{v}} + 2\kappa\widehat{\mathbf{v}} + 2\mathcal{H}\nabla_{\mathcal{S}}v_{\boldsymbol{\nu}}\right)$$

$$- \frac{2}{\mathrm{Re}}\mathcal{B}\nabla_{\mathcal{S}}v_{\boldsymbol{\nu}} + \widehat{\mathbf{f}} - \alpha_{\mathbf{v}}\left(\widehat{\mathbf{v}}\cdot\boldsymbol{\nu}\right)\boldsymbol{\nu} \tag{2.35}$$

$$\mathrm{div}_{\mathcal{S}}\,\widehat{\mathbf{v}} - v_{\boldsymbol{\nu}}\mathcal{H} = 0\,. \tag{2.36}$$

The systems (2.33)-(2.34) and (2.35)-(2.36) are equipped with the initial condition $\widehat{\mathbf{v}}\left(\cdot,t\right)|_{t=0} = \widehat{\mathbf{v}}_0(\cdot)$.

2.5.4 Relation to other derivation approaches

In this section, we successively transform [JOR17, equation (3.12)] to the present formulation (2.35)-(2.36) in order to show their equivalence. For simplicity we consider the surface force $\widehat{\mathbf{f}}$ to be zero and the velocity field $\widehat{\mathbf{v}}$ to be tangential.

Hence, equations (2.35) and (2.36) read

$$\boldsymbol{\pi}\partial_t\widehat{\mathbf{v}} + \boldsymbol{\nabla}_{\widehat{\mathbf{v}}}\widehat{\mathbf{v}} - v_{\boldsymbol{\nu}}\mathcal{B}\widehat{\mathbf{v}} - v_{\boldsymbol{\nu}}\nabla_{\mathcal{S}}v_{\boldsymbol{\nu}} = -\nabla_{\mathcal{S}}p + \frac{1}{\mathrm{Re}}\left(\mathrm{Rot}_{\mathcal{S}}\,\mathrm{rot}_{\mathcal{S}}\,\widehat{\mathbf{v}} + 2\kappa\widehat{\mathbf{v}} + 2\mathcal{H}\nabla_{\mathcal{S}}v_{\boldsymbol{\nu}}\right)$$

$$- \frac{2}{\mathrm{Re}}\mathcal{B}\nabla_{\mathcal{S}}v_{\boldsymbol{\nu}} \tag{2.37}$$

$$\mathrm{div}_{\mathcal{S}}\,\widehat{\mathbf{v}} - v_{\boldsymbol{\nu}}\mathcal{H} = 0\,. \tag{2.38}$$

We recall [JOR17, equation (3.12)] in their notation and in nondimensional form

$$\partial_{\Gamma}^{\bullet}\mathbf{u}_T + u_n\dot{\mathbf{n}} = -\nabla_{\Gamma}\pi + \frac{1}{\mathrm{Re}}\left(\Delta_{\Gamma}\mathbf{u}_T + K\mathbf{u}_T\right)$$

$$+ \frac{1}{\mathrm{Re}}\left(-\nabla_{\Gamma}\left(\nabla_{\Gamma}\cdot\mathbf{u}_T\right) - 2\left(\kappa\mathbf{P} - \mathbf{H}\right)\nabla_{\Gamma}u_n\right) \tag{2.39}$$

$$\nabla_{\Gamma}\cdot\mathbf{u}_T = -u_n\kappa\,. \tag{2.40}$$

Thereby, $\mathbf{u}_T$ denotes the tangential velocity, π the pressure, u_n the normal velocity, $\mathbf{n}$ the normal vector, $\mathbf{P}$ the projection to the tangent space, $\nabla_{\Gamma} = \mathbf{P}\nabla$ the surface gradient operator, Δ_{Γ} the Bochner Laplacian, K the Gaussian curvature, $\kappa = \nabla_{\Gamma}\cdot\mathbf{n}$ the mean curvature and $\mathbf{H} = \nabla_{\Gamma}\mathbf{n}$ the shape operator. Note that in contrast to [JOR17] we here assume that the surface gradient vector is formally a column vector. Replacing their notation by the notation of this thesis, i. e. replacing $\mathbf{u}_T$ by $\widehat{\mathbf{v}}$, π by p, u_n by $v_{\boldsymbol{\nu}}$, κ by $-\mathcal{H}$, K by κ, $\mathbf{H}$ by $-\mathcal{B}$, $\mathbf{n}$ by $\boldsymbol{\nu}$ and $\mathbf{P}$ by $\boldsymbol{\pi}$, yields for equations (2.39) and (2.40)

$$\partial_{\Gamma}^{\bullet}\widehat{\mathbf{v}} + v_{\boldsymbol{\nu}}\dot{\boldsymbol{\nu}} = -\nabla_{\Gamma}p + \frac{1}{\mathrm{Re}}\left(\Delta_{\Gamma}\widehat{\mathbf{v}} + \kappa\widehat{\mathbf{v}} - \nabla_{\Gamma}\left(\nabla_{\Gamma}\cdot\widehat{\mathbf{v}}\right)\right)$$

$$+ \frac{1}{\mathrm{Re}}\left(2\left(\mathcal{H}\boldsymbol{\pi} - \mathcal{B}\right)\nabla_{\Gamma}v_{\boldsymbol{\nu}}\right) \tag{2.41}$$

$$\nabla_{\Gamma}\cdot\widehat{\mathbf{v}} = v_{\boldsymbol{\nu}}\mathcal{H}\,. \tag{2.42}$$

By using $\nabla_{\Gamma}\cdot\widehat{\mathbf{v}} = \mathrm{div}_{\mathcal{S}}\,\widehat{\mathbf{v}}$ equation (2.42) is equivalent to equation (2.38) and we only need to consider equation (2.41) henceforth. Using the Weizenböck identity (2.12), the Bochner Laplacian in equation (2.41) can be replaced by

$$\Delta_{\Gamma}\widehat{\mathbf{v}} = -\boldsymbol{\Delta}^{\mathrm{dR}}\widehat{\mathbf{v}} + \kappa\widehat{\mathbf{v}} = \mathrm{Rot}_{\mathcal{S}}\,\mathrm{rot}_{\mathcal{S}}\,\widehat{\mathbf{v}} + \kappa\widehat{\mathbf{v}} + \nabla_{\mathcal{S}}\left(\mathrm{div}_{\mathcal{S}}\,\widehat{\mathbf{v}}\right)\,,$$

where $\mathbf{\Delta}^{\mathrm{dR}}\widehat{\mathbf{v}} = -\mathrm{Rot}_{\mathcal{S}}\,\mathrm{rot}_{\mathcal{S}}\,\widehat{\mathbf{v}} - \nabla_{\mathcal{S}}\,(\mathrm{div}_{\mathcal{S}}\,\widehat{\mathbf{v}})$ is used as above. Thus, by using $\nabla_{\Gamma}\xi = \nabla_{\mathcal{S}}\xi$ for scalar functions ξ on the surface $\mathcal{S}$ equation (2.41) reduces to

$$\partial_{\Gamma}^{\bullet}\widehat{\mathbf{v}} + v_{\boldsymbol{\nu}}\dot{\boldsymbol{\nu}} = -\nabla_{\mathcal{S}}p + \frac{1}{\mathrm{Re}}\left(\mathrm{Rot}_{\mathcal{S}}\,\mathrm{rot}_{\mathcal{S}}\,\widehat{\mathbf{v}} + 2\kappa\widehat{\mathbf{v}} + 2\mathcal{H}\nabla_{\mathcal{S}}v_{\boldsymbol{\nu}} - 2\mathcal{B}\nabla_{\mathcal{S}}v_{\boldsymbol{\nu}}\right) \quad (2.43)$$

and the right hand side is equivalent to that in equation (2.37). The left hand side of equation (2.43) can be rewritten as

$$\partial_{\Gamma}^{\bullet}\widehat{\mathbf{v}} + v_{\boldsymbol{\nu}}\dot{\boldsymbol{\nu}} = \boldsymbol{\pi}\partial_{t}\widehat{\mathbf{v}} + \boldsymbol{\pi}\left((\widehat{\mathbf{v}} + v_{\boldsymbol{\nu}}\boldsymbol{\nu})\cdot\nabla\right)\widehat{\mathbf{v}} - v_{\boldsymbol{\nu}}\mathcal{B}\widehat{\mathbf{v}} - v_{\boldsymbol{\nu}}\nabla_{\mathcal{S}}v_{\boldsymbol{\nu}}\,, \quad (2.44)$$

where the definitions $\partial_{\Gamma}^{\bullet}\widehat{\mathbf{v}} = \boldsymbol{\pi}\left(\partial_{t}\widehat{\mathbf{v}} + \left((\widehat{\mathbf{v}} + v_{\boldsymbol{\nu}}\boldsymbol{\nu})\cdot\nabla\right)\widehat{\mathbf{v}}\right)$ and $\dot{\boldsymbol{\nu}} = -\mathcal{B}\widehat{\mathbf{v}} - \nabla_{\mathcal{S}}v_{\boldsymbol{\nu}}$ from [JOR17] were used. Finally, if we assume that $\widehat{\mathbf{v}}$ is extended constantly off the surface in normal direction, we get the identity

$$\left[\boldsymbol{\pi}\left((\widehat{\mathbf{v}} + v_{\boldsymbol{\nu}}\boldsymbol{\nu})\cdot\nabla\right)\widehat{\mathbf{v}}\right]_{k} = \boldsymbol{\pi}_{kl}\left(\widehat{\mathbf{v}}_{i} + v_{\boldsymbol{\nu}}\boldsymbol{\nu}_{i}\right)\partial_{i}\widehat{\mathbf{v}}_{l} = \boldsymbol{\pi}_{kl}\left(\widehat{\mathbf{v}}_{i}\mathcal{D}_{i}\widehat{\mathbf{v}}_{l} + v_{\boldsymbol{\nu}}\boldsymbol{\nu}_{i}\mathcal{D}_{i}\widehat{\mathbf{v}}_{l}\right)$$
$$= \boldsymbol{\pi}_{kl}\widehat{\mathbf{v}}_{i}\mathcal{D}_{i}\widehat{\mathbf{v}}_{l} = \widehat{\mathbf{v}}_{i}\mathcal{D}_{i}\widehat{\mathbf{v}}_{k} = \left[\boldsymbol{\nabla}_{\widehat{\mathbf{v}}}\widehat{\mathbf{v}}\right]_{k}\,.$$

Therefore, the acceleration term (2.44) is equivalent to that in equation (2.37). Finally, we have shown the equivalence of the incompressible surface Navier-Stokes equation in the present form (2.37)-(2.38) to that proposed in [JOR17, equation (3.12)].

3 | Vorticity-stream function approach

In this chapter, we derive and numerically solve the vorticity-stream function approach of the incompressible surface Navier-Stokes equation and investigate the interplay between topology, geometry and fluid properties. Thereby, a surface finite element discretization is used to discretize the resulting equations in space. Motivated by designed examples for superfluids, we numerically consider the influence of a geometric potential on vortices for fluids with a finite Reynolds number and show examples in which geometric shape changes manipulate the flow field.

The main content of this chapter is taken from the author's publication [RV15] and its erratum [RV18a]. Additionally, the limitations of this approach and some simulation results from the book chapter [NRV17] are presented in the following Section 3.4 and Section 3.5.2, respectively.

Contents

3.1 Overview

An alternative formulation of the incompressible surface Navier-Stokes equation (2.28)-(2.29) is the vorticity-stream function formulation which has been considered for general stationary surfaces in [NVW12]. It turned out that this approach is only applicable for spherical surfaces (surfaces with genus $g(\mathcal{S}) = 0$), see [NRV17, RV18b] and the below Section 3.4. However, we will see that the vorticity-stream function approach is still a very appealing approach since the number of independent variables is reduced by dropping the pressure, the saddle point structure of the equations is removed and the incompressibility constraint is automatically fulfilled. Additionally, the resulting problem is a system of scalar-valued surface PDEs, for which established numerical methods – such as the standard surface finite element method [DE13] – can be used.

First, we consider some general assumptions and basic identities. Afterwards, we transform the incompressible surface Navier-Stokes equation (2.28)-(2.29) into the vorticity-stream function formulation step-by-step and present the limitations of this approach. Numerically, we consider similar examples as for superfluidic films and observe qualitatively the same phenomena as analyzed in [TVN10]. However, quantitatively the results differ and we analyze the influence of the Reynolds number as well as study the dynamics of the interaction between the geometry and the vortices of the flow field. Additionally, various examples for dynamically manipulating the flow field through shape changes are presented.

3.2 General assumptions and identities

Let ξ and η be scalar-valued functions, $\widehat{\mathbf{p}}$ an extended vector field on $\mathcal{S}$ as above and $\widehat{\mathbf{v}}$ the velocity field determined by equations (2.33) and (2.34), which is assumed to be tangential for simplicity. From [NVW12] we state the following identities. As in the two-dimensional flat space, it can be shown that

$$\operatorname{rot}_{\mathcal{S}} \nabla_{\mathcal{S}} \xi = \operatorname{div}_{\mathcal{S}} \operatorname{Rot}_{\mathcal{S}} \xi = 0 \,. \tag{3.1}$$

Furthermore, it holds

$$\text{rot}_{\mathcal{S}} \text{Rot}_{\mathcal{S}} \xi = \Delta_{\mathcal{S}} \xi \tag{3.2}$$

$$\text{Rot}_{\mathcal{S}} \xi \cdot \text{Rot}_{\mathcal{S}} \eta = \nabla_{\mathcal{S}} \xi \cdot \nabla_{\mathcal{S}} \eta \tag{3.3}$$

$$\text{rot}_{\mathcal{S}} (\xi \widehat{\mathbf{p}}) = \xi \, \text{rot}_{\mathcal{S}} \widehat{\mathbf{p}} + \widehat{\mathbf{p}} \cdot \text{Rot}_{\mathcal{S}} \xi \,, \tag{3.4}$$

where the dot in equations (3.3) and (3.4) means the standard dot product in $\mathbb{R}^3$. The Levi-Civita connection (transport term) can be componentwise expressed by the surface gradient operator $\mathcal{D}$, i.e. $[\boldsymbol{\nabla}_{\widehat{\mathbf{v}}} \widehat{\mathbf{v}}]_k = \widehat{\mathbf{v}}_i \mathcal{D}_i \widehat{\mathbf{v}}_k$. However, for the vorticity-stream function approach it is convenient to use the identity

$$\boldsymbol{\nabla}_{\widehat{\mathbf{v}}} \widehat{\mathbf{v}} = \frac{1}{2} \nabla_{\mathcal{S}} (\widehat{\mathbf{v}} \cdot \widehat{\mathbf{v}}) + \text{rot}_{\mathcal{S}} \widehat{\mathbf{v}} (\boldsymbol{\nu} \times \widehat{\mathbf{v}}) \,, \tag{3.5}$$

which was extensively used in [NVW12, NRV17, RV15, RV18a, RV18b]. Furthermore, we define the so-called Jacobian

$$J(\xi, \eta) := \text{Rot}_{\mathcal{S}} \xi \cdot \nabla_{\mathcal{S}} \eta = (\boldsymbol{\nu} \times \nabla_{\mathcal{S}} \xi) \cdot \nabla_{\mathcal{S}} \eta \,. \tag{3.6}$$

Note that right hand side of equation (3.6) is geometrically the triple product of the normal vector $\boldsymbol{\nu}$, the surface gradient of ξ and the surface gradient of η. Hence, the properties of the triple product directly yield the anti-symmetry of the Jacobian, i.e. $J(\xi, \eta) = -J(\eta, \xi)$, as well as $J(\xi, \xi) = 0$. Since the surface $\mathcal{S}$ is moving the curl operator $\text{rot}_{\mathcal{S}}(\cdot)$ and the partial time derivative ∂_t are non-commuting differential operators. The opposite is true on stationary surfaces which has been considered in [NVW12]. However, it holds

$$\text{rot}_{\mathcal{S}} (\boldsymbol{\pi} \partial_t \widehat{\mathbf{v}}) = \partial_t \text{rot}_{\mathcal{S}} \widehat{\mathbf{v}} + v_{\boldsymbol{\nu}} \mathcal{B} : \nabla_{\mathcal{S}} (\boldsymbol{\nu} \times \widehat{\mathbf{v}}) + \text{Rot}_{\mathcal{S}} v_{\boldsymbol{\nu}} \cdot (\mathcal{B} \widehat{\mathbf{v}}) \,,$$

which can be obtained by basic computations, see [RV18a]. Furthermore, we use the product rule and the identity $\text{div}_{\mathcal{S}} \mathcal{B} = \nabla_{\mathcal{S}} \mathcal{H}$ to finally get

$$\text{rot}_{\mathcal{S}} (\boldsymbol{\pi} \partial_t \widehat{\mathbf{v}}) = \partial_t \text{rot}_{\mathcal{S}} \widehat{\mathbf{v}} + v_{\boldsymbol{\nu}} \, \text{div}_{\mathcal{S}} (\mathcal{B} (\boldsymbol{\nu} \times \widehat{\mathbf{v}})) - v_{\boldsymbol{\nu}} (\boldsymbol{\nu} \times \widehat{\mathbf{v}}) \cdot \nabla_{\mathcal{S}} \mathcal{H}$$
$$+ \text{Rot}_{\mathcal{S}} v_{\boldsymbol{\nu}} \cdot (\mathcal{B} \widehat{\mathbf{v}}) \,. \tag{3.7}$$

3.3 Transformation

The starting point is the incompressible surface Navier-Stokes equation in its extended form (2.33)-(2.34) with $\widehat{\mathbf{f}} = 0$ for simplicity, i.e.

$$\boldsymbol{\pi}\partial_t\widehat{\mathbf{v}} + \boldsymbol{\nabla}_{\widehat{\mathbf{v}}}\widehat{\mathbf{v}} - v_{\boldsymbol{\nu}}\mathcal{B}\widehat{\mathbf{v}} - v_{\boldsymbol{\nu}}\nabla_{\mathcal{S}}v_{\boldsymbol{\nu}} = -\nabla_{\mathcal{S}}p + \frac{1}{\mathrm{Re}}\left(-\boldsymbol{\Delta}^{\mathrm{dR}}\widehat{\mathbf{v}} + 2\kappa\widehat{\mathbf{v}} + \nabla_{\mathcal{S}}\left(v_{\boldsymbol{\nu}}\mathcal{H}\right)\right)$$
$$- \frac{2}{\mathrm{Re}}\operatorname{div}_{\mathcal{S}}\left(v_{\boldsymbol{\nu}}\mathcal{B}\right) \tag{3.8}$$

$$\operatorname{div}_{\mathcal{S}}\widehat{\mathbf{v}} - v_{\boldsymbol{\nu}}\mathcal{H} = 0 \tag{3.9}$$

on the evolving surface $\mathcal{S}$. Note that we here assume that the velocity is tangential for simplicity and thus the penalty term vanishes identically. The approach in [NVW12] uses the ansatz $\widehat{\mathbf{v}} = \operatorname{Rot}_{\mathcal{S}}\psi$ with the stream function ψ. The present case is different since the divergence of the velocity field $\widehat{\mathbf{v}}$ is nonzero. Therefore, we consider

$$\widehat{\mathbf{v}} = \operatorname{Rot}_{\mathcal{S}}\psi + \nabla_{\mathcal{S}}\Phi \tag{3.10}$$

with a scalar potential function Φ, which also accounts for non-divergence free contributions of the velocity vector field $\widehat{\mathbf{v}}$. The ansatz in equation (3.10) is based on the Hodge decomposition (see [AMR88]) and is only valid for surfaces with genus $g(\mathcal{S}) = 0$ in the present form. For further details on this limitation we refer to the following Section 3.4.

The first step of the transformation is done by inserting equation (3.10) into equation (3.9), i.e.

$$\Delta_{\mathcal{S}}\Phi - v_{\boldsymbol{\nu}}\mathcal{H} = 0\,,$$

which yields a scalar-valued surface PDE for the potential Φ. The second step involves the momentum equation (3.8) and uses the curl operator $\operatorname{rot}_{\mathcal{S}}(\cdot)$ to obtain an equation for the stream function ψ. Thus, we apply the curl operator $\operatorname{rot}_{\mathcal{S}}(\cdot)$ to equation (3.8) and use the substitution

$$\phi = \Delta_{\mathcal{S}}\psi \tag{3.11}$$

T	$\text{rot}_\mathcal{S}\, T$	used equations
$\boldsymbol{\pi}\partial_t\widehat{\mathbf{v}}$	$\partial_t\phi + v_{\boldsymbol{\nu}}\,\text{div}_\mathcal{S}\left(\mathcal{B}\left(\text{Rot}_\mathcal{S}\,\Phi - \nabla_\mathcal{S}\psi\right)\right)$	(3.1), (3.2), (3.6),
	$\quad + v_{\boldsymbol{\nu}}\left(J\left(\mathcal{H},\Phi\right) + \nabla_\mathcal{S}\mathcal{H}\cdot\nabla_\mathcal{S}\psi\right)$	(3.7), (3.10), (3.11)
	$\quad + \text{Rot}_\mathcal{S}\, v_{\boldsymbol{\nu}}\cdot\left(\mathcal{B}\left(\text{Rot}_\mathcal{S}\,\psi + \nabla_\mathcal{S}\Phi\right)\right)$	
$\boldsymbol{\nabla}_{\widehat{\mathbf{v}}}\widehat{\mathbf{v}}$	$\text{div}_\mathcal{S}\left(\phi\nabla_\mathcal{S}\Phi\right) + J\left(\psi,\phi\right)$	(3.1), (3.2), (3.3),
		(3.4), (3.5), (3.6),
		(3.10), (3.11)
$v_{\boldsymbol{\nu}}\mathcal{B}\widehat{\mathbf{v}}$	$v_{\boldsymbol{\nu}}\,\text{rot}_\mathcal{S}\left(\mathcal{B}\left(\text{Rot}_\mathcal{S}\,\psi + \nabla_\mathcal{S}\Phi\right)\right)$	(3.10), (3.4)
	$\quad + \left(\mathcal{B}\left(\text{Rot}_\mathcal{S}\,\psi + \nabla_\mathcal{S}\Phi\right)\right)\cdot\text{Rot}_\mathcal{S}\, v_{\boldsymbol{\nu}}$	
$v_{\boldsymbol{\nu}}\nabla_\mathcal{S} v_{\boldsymbol{\nu}}$	0	(3.1), (3.4)
$\nabla_\mathcal{S} p$	0	(3.1)
$-\boldsymbol{\Delta}^{\text{dR}}\widehat{\mathbf{v}}$	$\Delta_\mathcal{S}\phi$	(2.14), (3.1), (3.2),
		(3.10), (3.11)
$\kappa\widehat{\mathbf{v}}$	$\text{div}_\mathcal{S}\left(\kappa\nabla_\mathcal{S}\psi\right) + J\left(\kappa,\Phi\right)$	(3.1), (3.2), (3.3),
		(3.4), (3.6), (3.10)
$\nabla_\mathcal{S}\left(v_{\boldsymbol{\nu}}\mathcal{H}\right)$	0	(3.1)
$\text{div}_\mathcal{S}\left(v_{\boldsymbol{\nu}}\mathcal{B}\right)$	$-\text{div}_\mathcal{S}\left(\boldsymbol{\nu}\times\text{div}_\mathcal{S}\left(v_{\boldsymbol{\nu}}\mathcal{B}\right)\right)$	(2.5)

Table 3.1: Term-by-term transformation of the incompressible surface Navier-Stokes equation (3.8)-(3.9).

with the so-called vorticity ϕ, since the resulting equation is a fourth order surface PDE. Accordingly, Table 3.1 provides the transformation term-by-term.

Finally, we obtain the vorticity-stream function approach of the incompressible surface Navier-Stokes equation (3.8)-(3.9) as system of three scalar-valued

surface PDEs for the stream function ψ, the vorticity ϕ and the potential Φ, i. e.

$$\partial_t \phi + J(\psi, \phi) + \operatorname{div}_{\mathcal{S}} (\phi \nabla_{\mathcal{S}} \Phi) = v_{\boldsymbol{\nu}} \left(\operatorname{div}_{\mathcal{S}} \left(\mathcal{B} \left(\nabla_{\mathcal{S}} \psi - \operatorname{Rot}_{\mathcal{S}} \Phi \right) \right) - J(\mathcal{H}, \Phi) \right)$$

$$+ v_{\boldsymbol{\nu}} \left(\operatorname{rot}_{\mathcal{S}} \left(\mathcal{B} \left(\operatorname{Rot}_{\mathcal{S}} \psi + \nabla_{\mathcal{S}} \Phi \right) \right) - \nabla_{\mathcal{S}} \mathcal{H} \cdot \nabla_{\mathcal{S}} \psi \right)$$

$$+ \frac{1}{\operatorname{Re}} \left(\Delta_{\mathcal{S}} \phi + 2 \operatorname{div}_{\mathcal{S}} (\kappa \nabla_{\mathcal{S}} \psi) + 2 J(\kappa, \Phi) \right)$$

$$+ \frac{2}{\operatorname{Re}} \operatorname{div}_{\mathcal{S}} (\boldsymbol{\nu} \times \operatorname{div}_{\mathcal{S}} (v_{\boldsymbol{\nu}} \mathcal{B})) \tag{3.12}$$

$$\phi = \Delta_{\mathcal{S}} \psi \tag{3.13}$$

$$\Delta_{\mathcal{S}} \Phi = v_{\boldsymbol{\nu}} \mathcal{H} \tag{3.14}$$

with appropriate initial conditions $\psi(\cdot, t)\,|_{t=0} = \psi_0(\cdot)$, $\phi(\cdot, t)\,|_{t=0} = \phi_0(\cdot)$ and $\Phi(\cdot, t)\,|_{t=0} = \Phi_0(\cdot)$.

Remark. *Consider the surface $\mathcal{S}$ to be stationary, i. e. $v_{\boldsymbol{\nu}} = 0$. Immediately, equation (3.14) yields $\Phi = 0$. Thus, we obtain*

$$\partial_t \phi + J(\psi, \phi) = \frac{1}{\operatorname{Re}} \left(\Delta_{\mathcal{S}} \phi + 2 \operatorname{div}_{\mathcal{S}} (\kappa \nabla_{\mathcal{S}} \psi) \right) \tag{3.15}$$

$$\phi = \Delta_{\mathcal{S}} \psi \tag{3.16}$$

for the stream function ψ and the vorticity ϕ. This system of equations coincides with the system proposed in [NVW12].

3.4 Limitations

In [NVW12] the surface vorticity-stream function approach for arbitrary stationary surfaces has been introduced. In that context, the word "arbitrary" has to be restricted to "arbitrary surfaces with genus $g(\mathcal{S}) = 0$" as shown in [NRV17, RV18b]. In the following we give some more detailed comments on this issue, which are partially taken from [NRV17]. Thereby, this section is restricted to stationary surfaces $\mathcal{S}$ with $v_{\boldsymbol{\nu}} = 0$ for simplicity.

The surface vorticity-stream function approach proposed by [NVW12] is based on the Hodge decomposition theorem (see [AMR88]) of the velocity field $\hat{\mathbf{v}}$ which

can be written as

$$\widehat{\mathbf{v}} = \widehat{\mathbf{v}}^{\mathrm{div}} + \widehat{\mathbf{v}}^{\mathrm{rot}} + \widehat{\mathbf{v}}^{\mathrm{harm}} \tag{3.17}$$

on a general surface $\mathcal{S}$ with a divergence free vector field $\widehat{\mathbf{v}}^{\mathrm{div}}$, a curl free vector field $\widehat{\mathbf{v}}^{\mathrm{rot}}$ and a divergence as well as curl free vector field $\widehat{\mathbf{v}}^{\mathrm{harm}}$. The first two parts are usually rewritten as $\widehat{\mathbf{v}}^{\mathrm{div}} = \mathrm{Rot}_{\mathcal{S}}\,\psi$ and $\widehat{\mathbf{v}}^{\mathrm{rot}} = \nabla_{\mathcal{S}}\Phi$ with scalar functions ψ and Φ as above. Since we require incompressibility of $\widehat{\mathbf{v}}$, i. e. $\mathrm{div}_{\mathcal{S}}\,\widehat{\mathbf{v}} = 0$, it can easily be verified that the curl free part $\widehat{\mathbf{v}}^{\mathrm{rot}}$ vanishes identically, i. e.

$$0 = \mathrm{div}_{\mathcal{S}}\,\widehat{\mathbf{v}} = \mathrm{div}_{\mathcal{S}}\,\widehat{\mathbf{v}}^{\mathrm{div}} + \mathrm{div}_{\mathcal{S}}\,\widehat{\mathbf{v}}^{\mathrm{rot}} + \mathrm{div}_{\mathcal{S}}\,\widehat{\mathbf{v}}^{\mathrm{harm}} = \mathrm{div}_{\mathcal{S}}\,\nabla_{\mathcal{S}}\Phi = \Delta_{\mathcal{S}}\Phi\,,$$

which leads to the trivial solution for Φ. Furthermore, on spherical surfaces ($g(\mathcal{S}) = 0$) we can drop the harmonic part since it is not possible to write a vector field that is divergence and curl free except of the zero vector field. Finally, the substitution $\widehat{\mathbf{v}} = \mathrm{Rot}_{\mathcal{S}}\,\psi$ holds in the case $g(\mathcal{S}) = 0$.

On surfaces with $g(\mathcal{S}) \neq 0$ the situation changes and the harmonic part $\widehat{\mathbf{v}}^{\mathrm{harm}}$ does not vanish in general. To demonstrate this property we use the torus which has genus $g(\mathcal{S}) = 1$ and can be described by the levelset function $q(\boldsymbol{x}) = (\sqrt{x^2 + z^2} - R)^2 + y^2 - r^2$, with $\boldsymbol{x} = (x, y, z)^T \in \mathbb{R}^3$, major radius R and minor radius r. Here, we use $R = 2$ and $r = 0.5$. Let φ and θ denote the standard parametrization angles on the torus. Then, the two basis vectors can be written as $\partial_{\varphi}\boldsymbol{x}$ as well as $\partial_{\theta}\boldsymbol{x}$ and read in Cartesian coordinates $\partial_{\varphi}\boldsymbol{x} = (-z, 0, x)$ as well as $\partial_{\theta}\boldsymbol{x} = (-\frac{xy}{\sqrt{x^2+z^2}}, \sqrt{x^2 + z^2} - 2, -\frac{yz}{\sqrt{x^2+z^2}})$, which are schematically shown in Figure 3.2. We find two (linear independent) harmonic vector fields on the torus

$$\widehat{\mathbf{v}}_{\varphi}^{\mathrm{harm}} = \frac{1}{4\left(x^2 + z^2\right)}\partial_{\varphi}\boldsymbol{x}$$

$$\widehat{\mathbf{v}}_{\theta}^{\mathrm{harm}} = \frac{1}{2\sqrt{x^2 + z^2}}\partial_{\theta}\boldsymbol{x}\,,$$

which are shown in Figure 3.1. It can be easily verified that $\mathrm{div}_{\mathcal{S}}\,\widehat{\mathbf{v}}_{\varphi}^{\mathrm{harm}} = \mathrm{rot}_{\mathcal{S}}\,\widehat{\mathbf{v}}_{\varphi}^{\mathrm{harm}} = 0$ as well as $\mathrm{div}_{\mathcal{S}}\,\widehat{\mathbf{v}}_{\theta}^{\mathrm{harm}} = \mathrm{rot}_{\mathcal{S}}\,\widehat{\mathbf{v}}_{\theta}^{\mathrm{harm}} = 0$.

First, we construct an example velocity field on the torus, which has zero har-
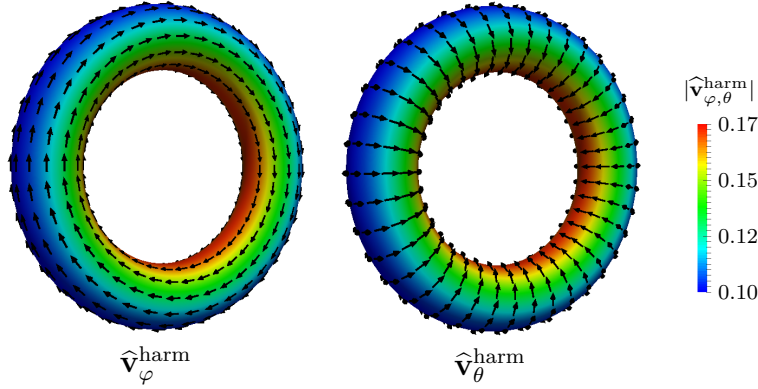
Figure 3.1: *Harmonic vector fields* $\widehat{\mathbf{v}}_{\varphi}^{\mathrm{harm}}$ *(left) and* $\widehat{\mathbf{v}}_{\theta}^{\mathrm{harm}}$ *(right) on a torus. The arrows are rescaled for better visualization. The color coding is according to the absolute value of the respective harmonic vector field.*
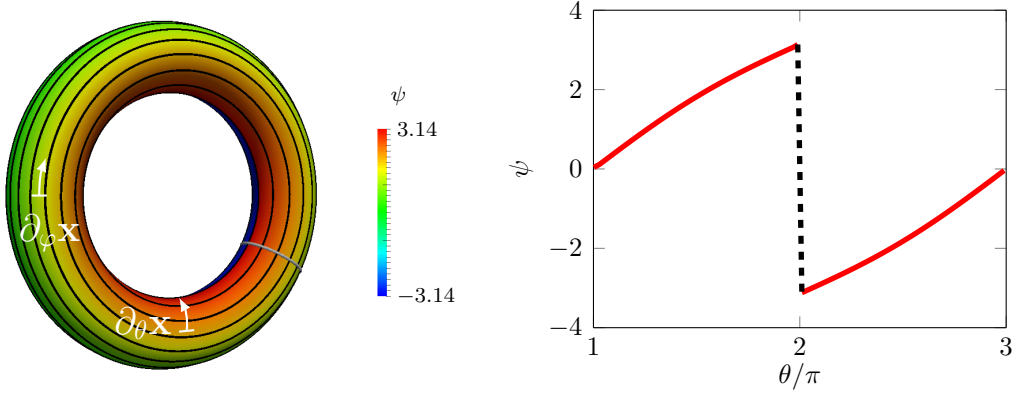
Figure 3.2: *Left: Streamlines and values of the discontinuous stream function* ψ *to represent the velocity field* $\widehat{\mathbf{v}} = \partial_{\varphi}\boldsymbol{x}$ *on the torus and the two basis vectors* $\partial_{\varphi}\boldsymbol{x}$ *and* $\partial_{\theta}\boldsymbol{x}$. *Right: Plot of the stream function values over the gray contour line in the left figure.*

monic parts but causes a discontinuity in the substituting scalar functions. Thus, let $\widehat{\mathbf{v}} = \partial_{\varphi}\boldsymbol{x}$, which has zero divergence and non-zero curl. The Hodge decomposition (3.17) leads to $\widehat{\mathbf{v}}^{\mathrm{rot}} = \widehat{\mathbf{v}}^{\mathrm{harm}} = 0$. In that case, the substitution $\widehat{\mathbf{v}} = \mathrm{Rot}_{\mathcal{S}}\,\psi$ holds, which is a first order differential equation for the scalar function ψ. The analytical solution of this equation reads $\psi(\theta) = -\frac{1}{4}\sin(\theta) + \theta - \pi$ in local coordinates. The linear contribution causes a discontinuity at $\theta = 2\pi$, which is shown in Figure 3.2 together with the streamlines of $\widehat{\mathbf{v}} = \partial_{\varphi}\boldsymbol{x}$ (contour lines of the stream function ψ).

In the next example we consider the vorticity-stream function formulation (3.15) and (3.16) with the mean of the two harmonic vector fields as initial condition, i.e. $\widehat{\mathbf{v}}_0(\boldsymbol{x}) = \frac{1}{2}(\widehat{\mathbf{v}}_\varphi^{\mathrm{harm}} + \widehat{\mathbf{v}}_\theta^{\mathrm{harm}})$, on the same torus. Following the Hodge decomposition (3.17) we have the initial conditions $\phi_0 = \psi_0 = 0$ and thus only the trivial solution over time. To also cover the harmonic parts, a different approach to numerically solve the incompressible surface Navier-Stokes equation is proposed in Chapter 4. There, we will use the same example for comparison with an alternative discretization technique based on discrete exterior calculus (DEC) from [NRV17]. For further details we refer to Chapter 4.

3.5 Geometric interactions in flow fields on stationary surfaces

First, we concentrate on stationary surfaces $\mathcal{S}$, i.e. surfaces with $v_{\boldsymbol{\nu}} = 0$. Therefore, equations (3.15) and (3.16) are considered and discretized by using the surface finite element method [DE13], which has already been tested for the considered equations in [NVW12].

3.5.1 Numerical approach

Let $\mathcal{T}$ be a conforming surface triangulation of mesh size h_{M} such that

$$\mathcal{S}_h = \bigcup_{T \in \mathcal{T}} T$$

is an interpolation of the surface $\mathcal{S}$ and let the time interval $(0, t_{\mathrm{end}}]$ with end time t_{end} be divided into a sequence of discrete times $0 < t_0 < t_1 < ...$ with time step width $\tau^m = t_m - t_{m-1}$. Furthermore, we define the discrete time derivative $d_\tau v^m := \frac{1}{\tau^m}(v^m - v^{m-1})$ for an arbitrary time-dependent function v. Thereby, v^m corresponds to the respective function at time $t = t_m$, i.e. $v^m := v(\cdot, t_m)$. Let further $L^2(\mathcal{S}_h)$ denotes the space of square-integrable functions on $\mathcal{S}_h$, $\mathcal{C}^k(\mathcal{S}_h)$ the space of k-times continuously differentiable functions on $\mathcal{S}_h$ and $\mathbb{P}^r(T)$ the set of polynomial functions of degree r on a triangle $T \in \mathcal{T}$. We introduce the

surface finite element space

$$V_h = \left\{ v \in \mathcal{C}^0(\mathcal{S}_h) \mid v_{|_T} \in \mathbb{P}^1(T), \ \forall T \in \mathcal{T} \right\},$$

which is used twice as trail and test space. Furthermore, let $(\cdot, \cdot)$ denote the standard scalar product on $L^2(\mathcal{S}_h)$. Thus, the surface finite element approximation of the equations (3.15) and (3.16) reads: Find $\phi^m, \psi^m \in V_h$ such that $\forall \alpha, \beta \in V_h$

$$\left(d_\tau \phi^m + J\left(\psi^{m-1}, \phi^m\right) \ , \ \alpha \right) = \frac{1}{\mathrm{Re}}\left(-\nabla_{\mathcal{S}}\phi^m - 2\kappa\nabla_{\mathcal{S}}\psi^m \ , \ \nabla_{\mathcal{S}}\alpha \right)$$
$$\left(\phi^m \ , \ \beta \right) = -\left(\nabla_{\mathcal{S}}\psi^m \ , \ \nabla_{\mathcal{S}}\beta \right).$$

Within this semi-implicit discretization, we assume κ to be given analytically or computable at the required accuracy. The implementation is done in the adaptive finite element toolbox AMDiS [VV07, WLPV15]. As linear solver a BiCGStab(l) method with $l = 2$ and a Jacobi preconditioner is used. To efficiently distribute the workload on many-core-platforms, we additionally use a domain decomposition approach.

3.5.2 Simulation results

The goal of this section is to demonstrate the analogies of the incompressible surface Navier-Stokes equation with known results for defect interactions mentioned in Section 2.3 and to show the complex interplay of topology, geometry, defect interactions and hydrodynamics.

We first come back to the unit sphere and consider the interaction of two $+1$ defects (vortices). We consider the solution for two vortices located in the north pole $(0, 0, 1)^T$ and south pole $(0, 0, -1)^T$, given by $\psi(\boldsymbol{x}) = z$ and $\phi(\boldsymbol{x}) = -2z$ with $\boldsymbol{x} = (x, y, z)^T \in \mathcal{S}$. This is a known analytic solution for the stationary problem. We consider a perturbed solution and specify the initial condition for the vorticity as $\phi(\boldsymbol{x}) = -2\tilde{z}$ with $\tilde{\boldsymbol{x}} = \mathbf{R}\boldsymbol{x} \in \mathcal{S}$. Thereby, $\mathbf{R} = \mathbf{R}(\eta)$ denotes a rotation matrix around the x-axis with a space dependent angle $\eta = \eta(\boldsymbol{x}) = \frac{z}{2}$. The initial condition for the stream function ψ can then be computed by solving
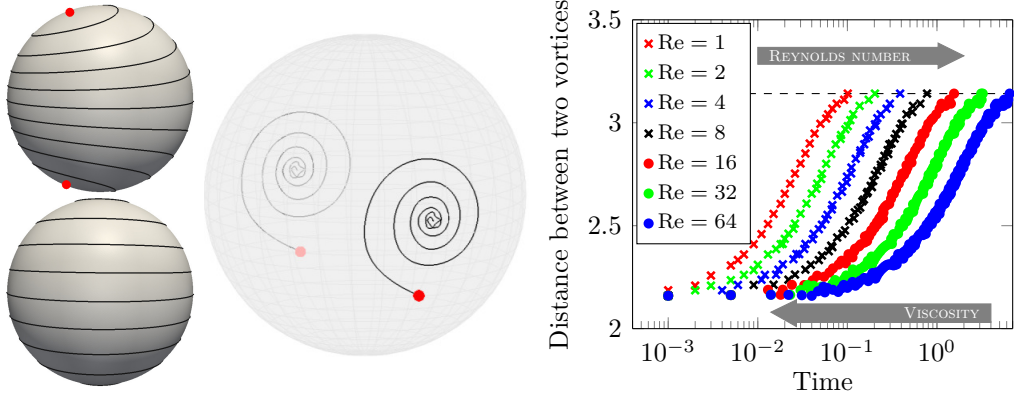
Figure 3.3: Left: Streamlines for the initial condition (top) and the reached steady state solution (bottom) for Re = 1. *Center: Vortex trajectories on the sphere for* Re = 100. *The red points (left and center) indicate the respective initial positions of the vortices. Right: Geodesic distance between the two vortices over time for various Reynolds numbers. The gray arrows indicate increasing Reynolds number and viscosity.*

the surface Poisson problem according to equation (3.16). Figure 3.3 (left) gives an illustration of the perturbed flow field with two vortices. The vortices are known to repel each other and their interaction energy depends linearly on the vortex separation distance [PL96]. Figure 3.3 (right) shows the dynamics towards the analytic solution, where the vortices are maximally separated, for different Reynolds numbers. For Re = 1 the vortices approach their maximal separation directly, as shown in Figure 3.3 (left). This is no longer the case for an increased Reynolds number. Figure 3.3 (center) shows the vortex trajectories for Re = 100. The dependency of the time needed to reach the stationary state on the Reynolds number is shown in Figure 3.3 (right). As larger the Reynolds number, as longer it takes to reach the stationary state.

This stationary state represents a so-called Killing vector field, i. e. a rotating flow which does not dissipate. As shown in [NRV17], the incompressible surface Navier-Stokes equation (3.15)-(3.16) is a dissipative system, i. e. $\frac{\mathrm{d}}{\mathrm{d}t}\mathcal{F}^{\mathrm{kin}} \leq 0$ with the kinetic energy $\mathcal{F}^{\mathrm{kin}} := \frac{1}{2}\int_{\mathcal{S}} \|\hat{\mathbf{v}}\|^2 \, \mathrm{d}\mathcal{S}$. The equality in this equation holds, if Re $\to \infty$ or the deformation tensor vanishes identically. The latter defines the property of a Killing vector field, which can be realized on rotational symmetric surfaces such as the sphere. The analogy in the flat case is a bi-periodic domain

| h_M	$|\mathcal{F}_0^\mathrm{kin} - \mathcal{F}^\mathrm{kin}(10)|$	*EOC*
0.109	0.0777	—
0.066	0.0295	1.93
0.048	0.0154	2.05
0.031	0.0063	2.03
0.022	0.0031	2.04
0.015	0.0016	1.78
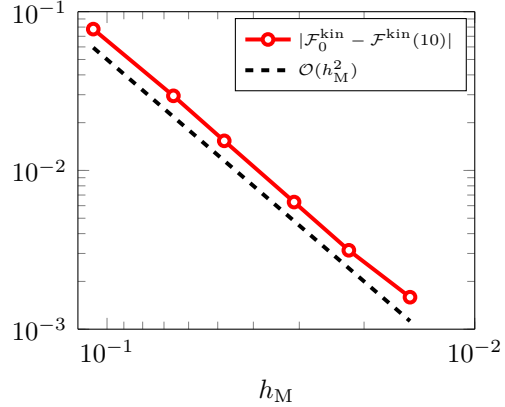
Figure 3.4: *Left: Values of the error in the kinetic energy and the experimental order of convergence (EOC) for different mesh sizes h_M (maximum circumcircle diameter of all triangles) at time $t = 10$. Right: Visualized error in the kinetic energy against meshsize h_M.*

in which a constant velocity vector field in one direction is defined. This system also does not dissipate. We will use this property in some of the following examples.

However, in the next example we investigate the numerical dissipation which occurs due to the approximation error of the temporal and spatial discretization. Again, the sphere is considered where the Killing vector field can be analytically written as $\widehat{\mathbf{v}}_\mathrm{K}(\boldsymbol{x}) = (y, -x, 0)^T$ with coordinates $\boldsymbol{x} = (x, y, z)^T \in \mathcal{S}$. The corresponding analytical form for the stream function is $\psi_\mathrm{K}(\boldsymbol{x}) = z$ and for the the vorticity is $\phi_\mathrm{K}(\boldsymbol{x}) = -2z$ which are used as initial conditions. We let the flow evolve for various mesh sizes h_M and compute the error in the kinetic energy $\mathcal{F}^\mathrm{kin}$ at time $t = 10$, i.e. $|\mathcal{F}_0^\mathrm{kin} - \mathcal{F}^\mathrm{kin}(10)|$ where $\mathcal{F}_0^\mathrm{kin}$ is exact kinetic energy and $\mathcal{F}^\mathrm{kin}(10)$ is the kinetic energy at time $t = 10$. The timestep is considered to be $\tau = \tau^m = 0.1$. Figure 3.4 shows the computed error in the kinetic energy, which essentially shows second order convergence in the mesh size h_M.

Next, we consider three simple examples which are adapted from [TVN10] to investigate geometric interactions. The first considers a circular domain with a bump, slightly placed outside the center, the second a circular domain with a Gaussian saddle and the third the Enneper disk, a minimal surface with vanishing mean curvature $\mathcal{H}$. Within the first two cases the surface is represented

by

$$\mathcal{S} = \left\{ (x, y, z)^T \in \mathbb{R}^3 \mid x^2 + y^2 < r^2, z = h(x, y) \right\}$$

with $r = 1$ and a height-function h specifying the bump

$$h(x, y) = \alpha r_0 \exp\left(-\frac{(x - m_x)^2 + (y - m_y)^2}{2 r_0^2} \right) \tag{3.18}$$

with $\alpha = 2.5$, $r_0 = 0.2$ and position $(m_x, m_y)^T$, or the Gaussian saddle

$$h(x, y) = \frac{\alpha}{r_0} \left((x - m_x)^2 - \lambda (y - m_y)^2 \right) \exp\left(-\frac{(x - m_x)^2 + (y - m_y)^2}{2 r_0^2} \right) \tag{3.19}$$

with $\alpha = 1.5$, $\lambda = 0.99$, $r_0 = 0.2$ and position $(m_x, m_y)^T$. The Enneper disk is parameterized over the circular domain $\mathcal{S}$ with $h(x, y) = 0$ and $r = 1.5$ by

$$\tilde{x} = \frac{1}{3} \left(\frac{1}{3} x^3 - xy^2 - x \right)$$
$$\tilde{y} = \frac{1}{3} \left(-\frac{1}{3} y^3 + yx^2 + y \right)$$
$$\tilde{z} = \frac{1}{3} \left(x^2 - y^2 \right).$$

All of the three cases require the presence of boundaries in order to induce one $+1$ defect and study its geometric interaction. More precisely, on the circular boundary $\partial \mathcal{S}$, we specify $\phi = 2c$ for the vorticity and $\psi = \frac{c}{2} r^2$ for the stream function with a constant c. This induces a tangential velocity at the boundary $\partial \mathcal{S}$ and thus a vortex within $\mathcal{S}$. We further specify zero initial conditions for the vorticity ϕ and the stream function ψ and let the flow evolve. Figure 3.5 shows the reached steady state solutions. All results show the same qualitative influence by the Gaussian curvature as described for superfluids in [TVN10]. In the first case, the bump leads to a lower velocity above the vortex (visible by a larger spacing between the contour lines of the stream function ψ), which creates a higher pressure and pushes the vortex away from the bump. Competing with the boundary condition, which favors the vortex to be in the center, this leads to a stationary profile with the vortex placed off the center. The second case is
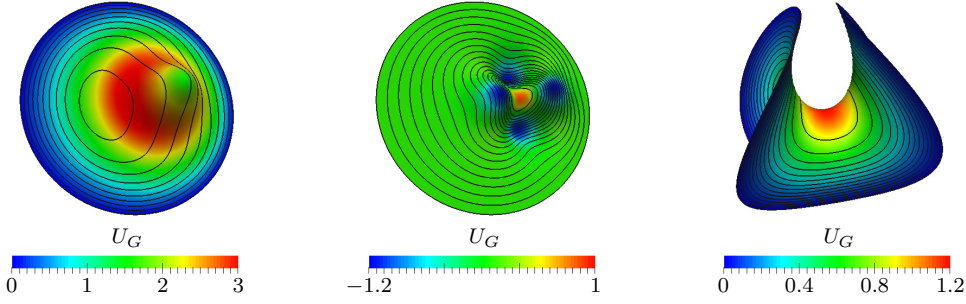
Figure 3.5: Stationary solution for the circular domain with a bump (left), the circular domain with a Gaussian saddle (center) and the Enneper disk (right). Shown are the contour lines for ψ. The color coding is according to the geometric potential U_G.

a vortex-trapping surface. The geometric potential has its absolute minimum in the center of the saddle, which attracts the vortex, independent of the position of the Gaussian saddle on the disk. The third case considers a minimal surface. In this example, the vortex is attracted to the middle of the surface. All these examples nicely demonstrates the vortex-geometry interaction.

We will now consider an example in which topological defects, geometric interactions and defect interactions are present. We use a geometry which is topologically equivalent to the sphere, but with non-constant Gaussian curvature, i.e. a common test case in computer graphics, the Stanford bunny. To make flow simulations on this geometry feasible, the original mesh had to be improved and the surface had to be smoothed to remove sharp corners. The obtained geometry still contains regions with large positive and negative Gaussian curvature. We start our simulation with noise as initial condition for the vorticity ϕ and use a fixed Reynolds number Re = 1. Figure 3.6 (left) shows the simulation result in which the defect positions becomes stationary. Note that dissipation still takes place due to lack of rotational symmetry of the geometry. In this state, we observe high velocity differences and three $+1$ defects (vortices) as well as one -1 defect (saddle), see Figure 3.6 (center). Thus, we obtain $\sum_i \mathrm{ind}_V(\mathbf{d}_i) = 1 + 1 + 1 - 1 = 2 = \chi(\mathcal{S})$ and therefore a different realization of the Poincaré-Hopf theorem. These stationary positions of the defects are reached for all considered realizations of the initial conditions and are clearly a result of the strong influence of the Gaussian curvature on the flow. Figure 3.6
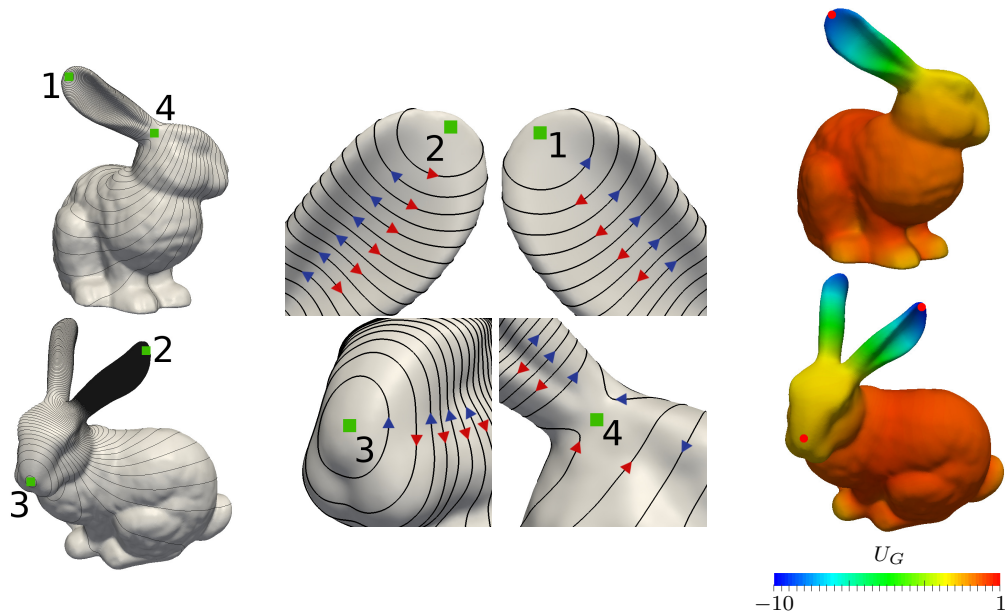
Figure 3.6: Left: Streamlines of the flow field on the Stanford bunny with the green marked positions of the different defects. Numbers 1 to 3 indicate vortices (+1 defects) and number 4 indicates a saddle point (−1 defect). Center: Identified defects with rescaled streamlines and different flow directions (red and blue arrows) according to different realizations of the noise initial condition. Right: Geometric potential U_G with identified local minima (red points).

(right) shows the respective geometric potential U_G. The geometry has many hyperbolic and elliptic points but the most influencing regions are the two minima of the geometric potential U_G located in the left and the right ear. Another local minimum is located on the nose, see Figure 3.6 (right). These positions agree very well with the positions of the vortices in Figure 3.6 (center). All +1 defects (labeled "1", "2", "3") are placed on extreme values of the Gaussian curvature, while the -1 defect (labeled "4") appears at a saddle, both in agreement with the discussed linear contribution in equation (2.21). For less viscous fluids, other regions of the surface (e.g. local extreme values of the geometric potential U_G) influence the flow field such that additional vortices can occur and the solution might converge towards a different realization of the Poincaré-Hopf theorem. However, a quantitative analysis of this influence seems not feasible for the considered geometry.

As already analyzed in the examples from above the vortices in the flow field
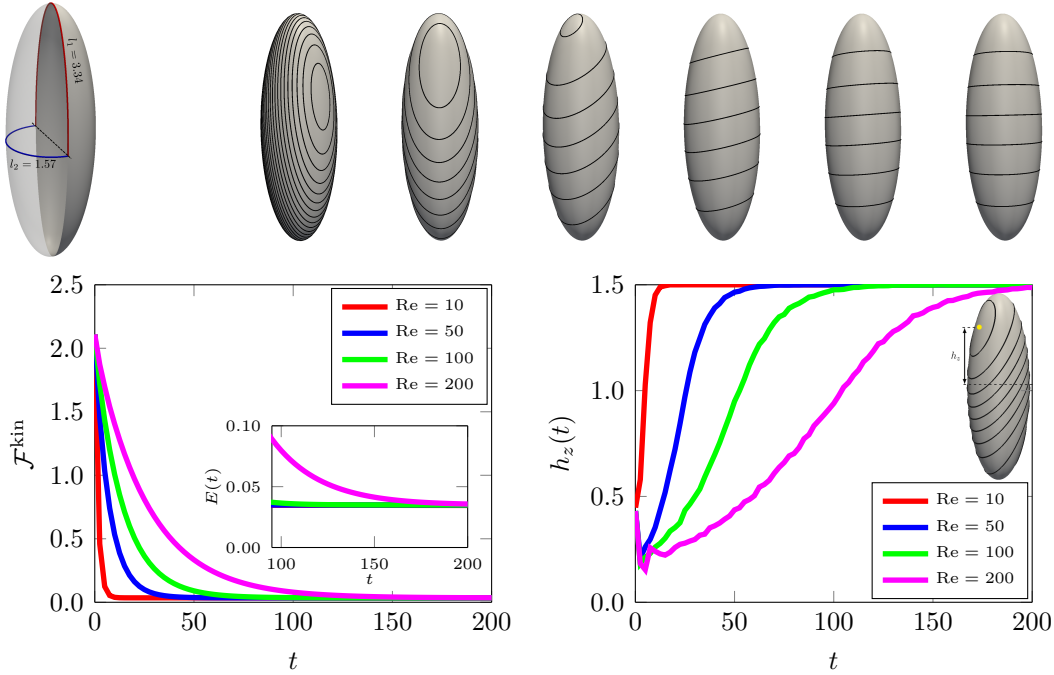
Figure 3.7: Top: Distances on the ellipsoid (left) together with the streamlines at times $t = 0, 4, 8, 12, 16$ and 20 for the rotating flow (left to right). Results are shown for $\mathrm{Re} = 10$. Bottom: Kinetic energy $\mathcal{F}^{\mathrm{kin}}$ against time t (left) and the height for the upper vortex h_z against time t for various Reynolds numbers Re.

repel each other and are attracted by regions of high Gaussian curvature. To further quantify these phenomena we consider an ellipsoid, represented by the levelset function $q(\boldsymbol{x}) = (x/a)^2 + (y/b)^2 + (z/c)^2$, with $\boldsymbol{x} = (x, y, z)^T \in \mathbb{R}^3$, $a = b = 0.5$ and $c = 1.5$. We consider the initial solutions $\psi_0(\boldsymbol{x}) = y + 0.1z$ and use the timestep $\tau = \tau^m = 0.1$. Figure 3.7 shows the geometric properties, the streamlines at various times for $\mathrm{Re} = 10$ as well as the kinetic energy over time and the position of one vortex over time for various Reynolds numbers. The flow converges to a Killing vector field with the vortices located at the high Gaussian curvature regions. However, these positions also favors the long range interaction between the vortices, since they maximize their distance. Thus, we cannot argue on a geometric interaction. The time to reach the Killing vector field strongly depends on the Reynolds number Re, the lower Re the faster it is reached.

The next example considers a biconcave shape, represented by the levelset func-
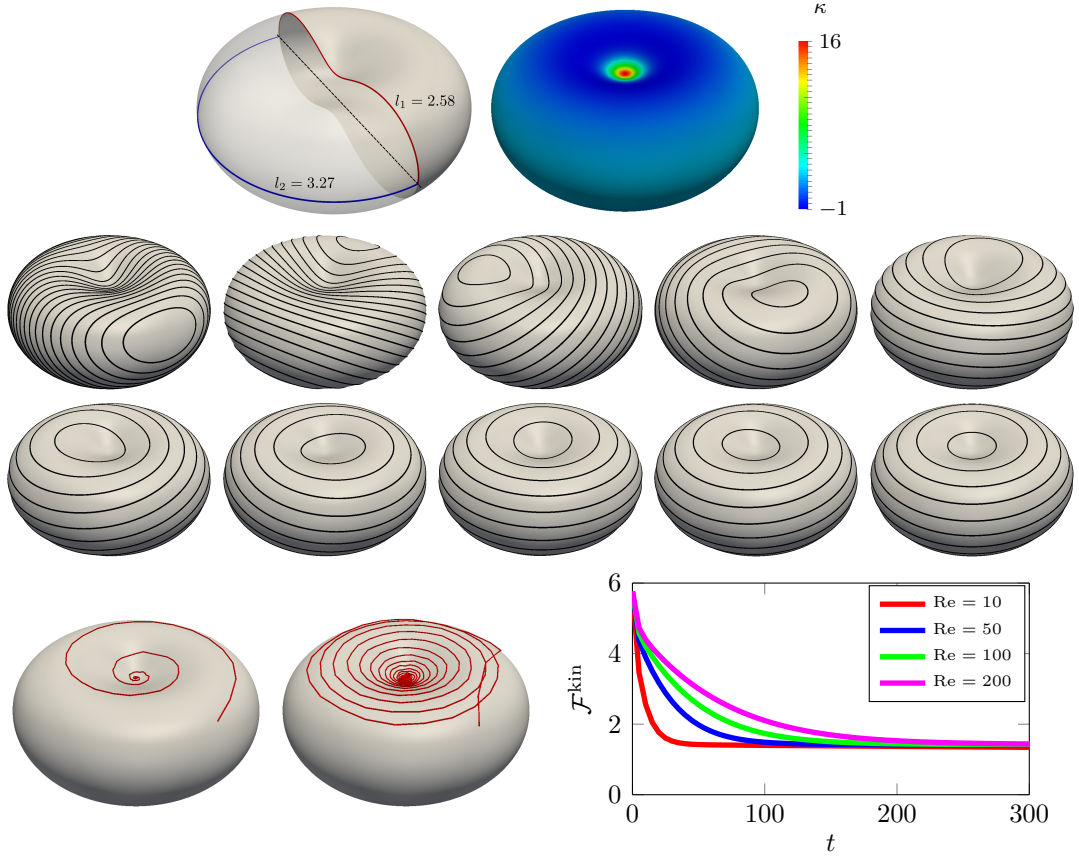
Figure 3.8: Top: Distances on the biconcave shape (left) together with the Gaussian curvature (right). Middle: Streamlines at times $t = 0, 7, 14, 21, 28, 35, 42, 49, 56$ and 200 (left to right, top to bottom) for the rotating flow. Results are shown for $\mathrm{Re} = 10$. Bottom: Two examples for the vortex trajectories for $\mathrm{Re} = 10$ (left) and $\mathrm{Re} = 100$ (center) and kinetic energy $\mathcal{F}^{\mathrm{kin}}$ against time t for various Reynolds numbers Re (right).

tion $q(\boldsymbol{x}) = (a^2 + x^2 + y^2 + z^2)^3 - 4a^2(y^2 + z^2) - c^4$, with $\boldsymbol{x} = (x, y, z)^T \in \mathbb{R}^3$, $a = 0.72$ and $c = 0.75$. We consider the initial solution $\psi_0(\boldsymbol{x}) = y + z$ and use the timestep $\tau = \tau^m = 0.1$. Figure 3.8 shows the geometric properties together with the trajectories of the upper vortex for different Reynolds numbers, the streamlines at various times, a plot of the Gaussian curvature and the kinetic energy over time. Again, the flow converges to a Killing vector field with the vortices located at the high Gaussian curvature regions. Here, the location of the vortices clearly is a result of the geometric interaction, as their distance is

not maximized, see Figure 3.8 (top, left). Again, the time to reach the Killing vector field strongly depends on the Reynolds number Re, the lower Re the faster it is reached.

The results on numerical dissipation, the ellipsoid and the biconcave shape are validated against a different discretization technique of the incompressible surface Navier-Stokes equation based on discrete exterior calculus (DEC) in [NRV17]. The vortex trajectories and kinetic energy values over time are almost indistinguishable for both discretizations. For more details we refer to [NRV17].

3.6 Manipulating flow fields through shape changes

Next, we consider a surface evolution in normal direction, i.e. $v_\nu \neq 0$, and assume that the surface area remains (at least globally) conserved. This requirement follows from our incompressibility assumption and is a typical constraint for, e.g., lipid bilayer membranes [Hel73]. Thus, the full system of equations (3.12), (3.13) and (3.14) is considered.

3.6.1 Numerical approach

As in Section 3.5.1, the above system of equations (3.12), (3.13) and (3.14) is discretized in time by a semi-implicit Euler scheme. We adapt the notation of Section 3.5.1 and introduce the surface finite element approximation. Let $\mathcal{T} = \mathcal{T}(t)$ be a conforming triangulation of the surface $\mathcal{S} = \mathcal{S}(t)$ of mesh size h_M and let $\mathcal{S}_h$ be an interpolation of $\mathcal{S}$ such that

$$\mathcal{S}_h = \bigcup_{T \in \mathcal{T}} T$$

at time $t = t_m$. We consider each space, set and quantity at time $t = t_m$ and therefore omit indexing with the timestep number m for better readability

(unless it is explicitly needed). The surface finite element space reads

$$V_h = \left\{ v \in \mathcal{C}^0(\mathcal{S}_h) \mid v_{|_T} \in \mathbb{P}^1(T), \ \forall T \in \mathcal{T} \right\}.$$

Note that $\mathcal{C}^k(\mathcal{S}_h)$, $\mathbb{P}^r(T)$, $L^2(\mathcal{S}_h)$ and the standard L^2 scalar product $(\cdot, \cdot)$ can analogously be defined as in Section 3.5.1. The finite element space V_h is thereby used twice as trail and test space. First, we solve equation (3.14) for the potential Φ^m in each timestep and equations (3.12) as well as (3.13) for the stream function ψ^m and the vorticity ϕ^m afterwards. Thus, the finite element approximation reads: For $m = 1, 2, 3, \ldots$ find $\Phi^m \in V_h$ such that $\forall \gamma \in V_h$

$$\left(-\nabla_{\mathcal{S}} \Phi^m , \ \nabla_{\mathcal{S}} \gamma \right) = \left(v_{\boldsymbol{\nu}} \mathcal{H} , \ \gamma \right).$$

Furthermore, find $\phi^m, \psi^m \in V_h$ such that $\forall \alpha, \beta \in V_h$

$$\left(\mathrm{d}_\tau \phi^m + \mathbf{p} \cdot \nabla_{\mathcal{S}} \psi^m + J\left(\psi^{m-1}, \phi^m \right) - g , \ \alpha \right)$$
$$= \frac{1}{\mathrm{Re}} \left(-\nabla_{\mathcal{S}} \phi^m + 2\kappa \nabla_{\mathcal{S}} \psi^m , \ \nabla_{\mathcal{S}} \alpha \right)$$
$$+ \left(\mathcal{M} \nabla_{\mathcal{S}} \psi^m + \phi^m \nabla_{\mathcal{S}} \Phi^m + \mathbf{q} , \ \nabla_{\mathcal{S}} \alpha \right)$$
$$\left(\phi^m , \ \beta \right) = -\left(\nabla_{\mathcal{S}} \psi^m , \ \nabla_{\mathcal{S}} \beta \right),$$

where we have used the discrete time derivative d_τ from Section 3.5.1 and the abbreviations

$$\mathcal{M} := v_{\boldsymbol{\nu}} \left(\boldsymbol{\nu} \times \mathbf{Rot}(\boldsymbol{\nu})^T - \mathcal{B} \right)$$
$$\mathbf{p} := \mathcal{B} \nabla_{\mathcal{S}} v_{\boldsymbol{\nu}} + v_{\boldsymbol{\nu}} \nabla_{\mathcal{S}} \mathcal{H} - \left(\boldsymbol{\nu} \times \mathcal{B} \operatorname{rot}_{\mathcal{S}}(v_{\boldsymbol{\nu}}) \right)$$
$$\mathbf{q} := v_{\boldsymbol{\nu}} \mathcal{B} \operatorname{rot}_{\mathcal{S}}(\Phi^m) + v_{\boldsymbol{\nu}} \boldsymbol{\nu} \times \left(\mathcal{B} \nabla_{\mathcal{S}} \Phi^m \right) - \frac{2}{\mathrm{Re}} \boldsymbol{\nu} \times \operatorname{div}_{\mathcal{S}} \left(v_{\boldsymbol{\nu}} \mathcal{B} \right)$$
$$g := -v_{\boldsymbol{\nu}} J\left(\mathcal{H}, \Phi^m \right) + \frac{2}{\mathrm{Re}} J\left(\kappa, \Phi^m \right) - \mathcal{B} \operatorname{rot}_{\mathcal{S}}(v_{\boldsymbol{\nu}}) \cdot \nabla_{\mathcal{S}} \Phi^m$$
$$+ \nabla_{\mathcal{S}} v_{\boldsymbol{\nu}} \cdot \left(\mathcal{B} \operatorname{rot}_{\mathcal{S}}(\Phi^m) \right),$$

where $\mathbf{Rot}(\boldsymbol{\nu})$ is a generalized curl operator with components $[\mathbf{Rot}(\boldsymbol{\nu})]_{ij} = (\operatorname{Rot}_{\mathcal{S}}(\boldsymbol{\nu}_j))_i$. The components of the generalized cross product $\boldsymbol{\nu} \times \mathbf{A}$ with a
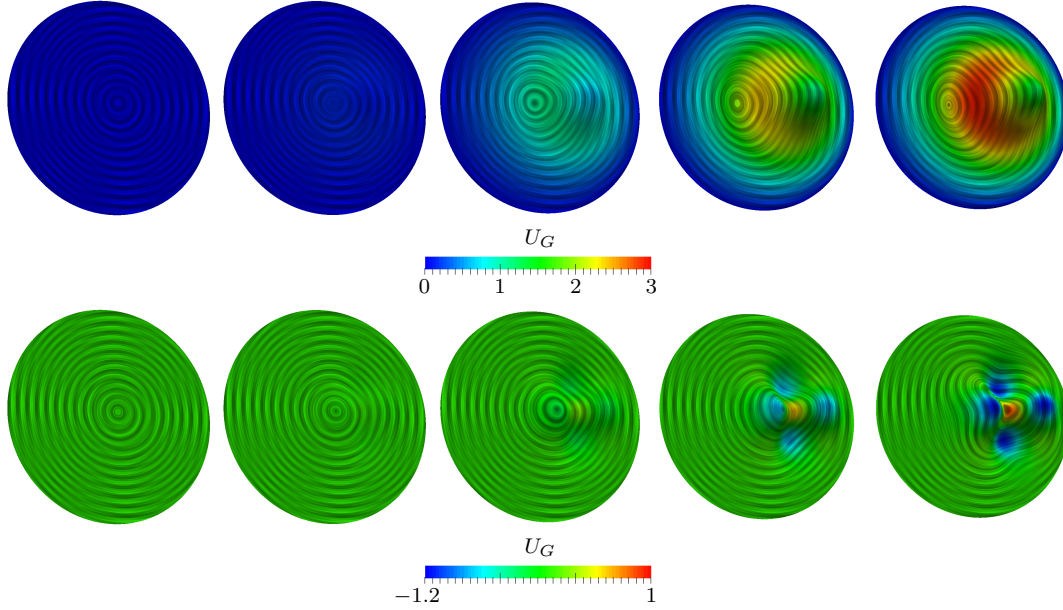
Figure 3.9: Evolution of $\widehat{\mathbf{v}}$ for the evolving bump (top row) and the evolving Gaussian saddle (bottom row) for $t = 2, 14, 26, 38$ and 50 (left to right) visualized as noise concentration field aligned to the velocity field $\widehat{\mathbf{v}}$. The color coding is according to the geometric potential U_G.

matrix $\mathbf{A}$ are determined by $[\boldsymbol{\nu} \times \mathbf{A}]_{ij} := (\boldsymbol{\nu} \times \mathbf{A}\mathbf{e}_j)_i$, where $\mathbf{e}_j$ is the j-th unit vector in $\mathbb{R}^3$. Again, the Gaussian curvature κ, the mean curvature $\mathcal{H}$, the shape operator $\mathcal{B}$ and the normal vector $\boldsymbol{\nu}$ are assumed to by given analytically or computable at the required accuracy in each timestep. As in Section 3.5, the implementation is done in the adaptive finite element toolbox AMDiS [VV07, WLPV15] with the domain decomposition approach and a BiCGStab(l) method with $l = 2$ and a Jacobi preconditioner to solve the resulting linear systems.

3.6.2 Simulation results

To demonstrate the strong influence through shape changes, we modify the considered examples for the stationary circular domain and let the bump and the Gaussian saddle evolve. First, we use $\alpha = \alpha(t)$ in the considered height profile with $\alpha(0) = 0$ and $\alpha(T) = 2.5$ or 1.5, for the bump, i. e. equation (3.18), and the Gaussian saddle, i. e. equation (3.19), respectively. Figure 3.9 shows the evolution of the velocity field, which adapt to the changing geometry leading
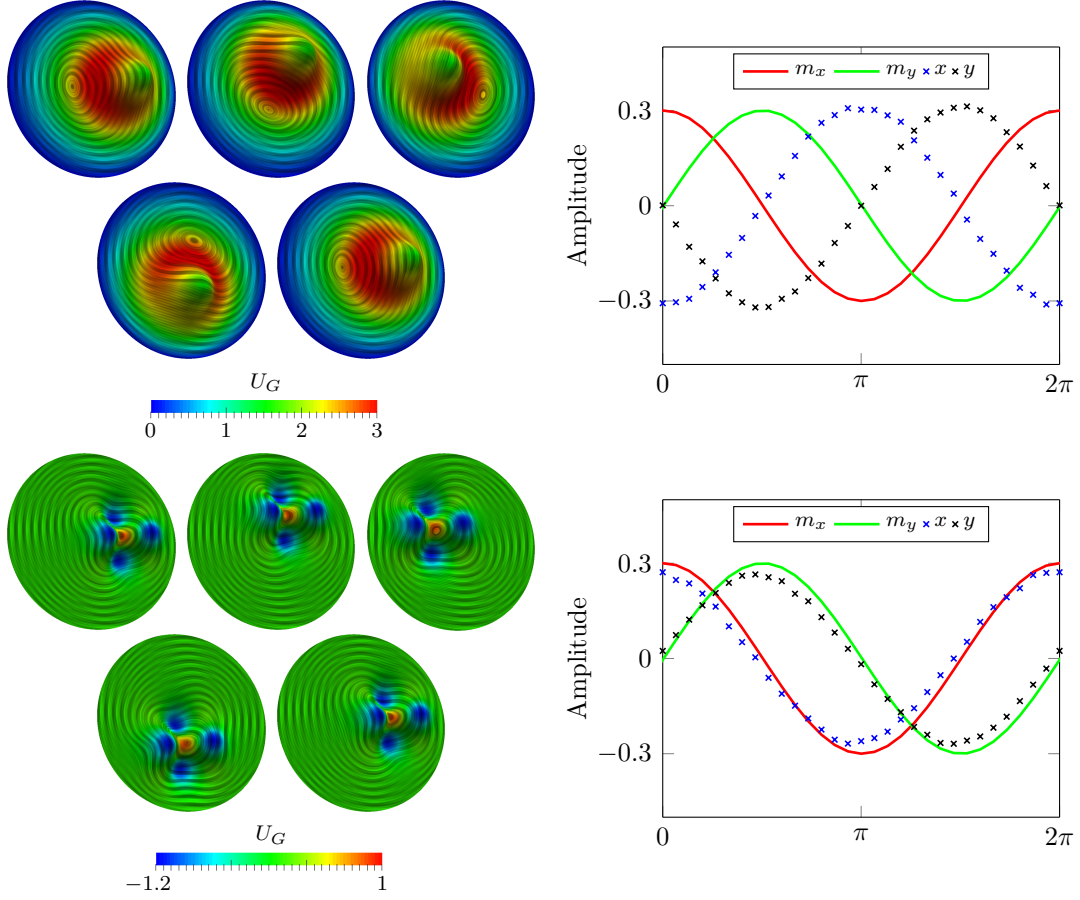
Figure 3.10: Top row: Evolution of $\widehat{\mathbf{v}}$ for the rotating bump for $t = 2, 11, 19, 27$ and 36 (left to right and top to bottom) visualized as noise concentration field aligned to the velocity field $\widehat{\mathbf{v}}$ (left) and evolution of the bump location $(m_x, m_y)^T$ and the vortex location $(x, y)^T$ for a full period of rotation (right). Bottom row: Evolution of $\widehat{\mathbf{v}}$ for the rotating Gaussian saddle for $t = 2, 11, 19, 27$ and 36 (left to right and top to bottom) visualized as noise concentration field aligned to the velocity field $\widehat{\mathbf{v}}$ (left) and evolution of the saddle location $(m_x, m_y)^T$ and the vortex location $(x, y)^T$ for a full period of rotation (right). The color coding is according to the geometric potential U_G.

to the same stationary solution as in the stationary case in Section 3.5.2. As a second example, we let the bump and the Gaussian saddle rotate around the center with $(m_x, m_y)^T = (m_x(t), m_y(t))^T$ and a constant angular velocity, see Figure 3.10. In that case the geometric forces are higher than the inertial forces and the center of the vortex follows the center of the Gaussian saddle, see
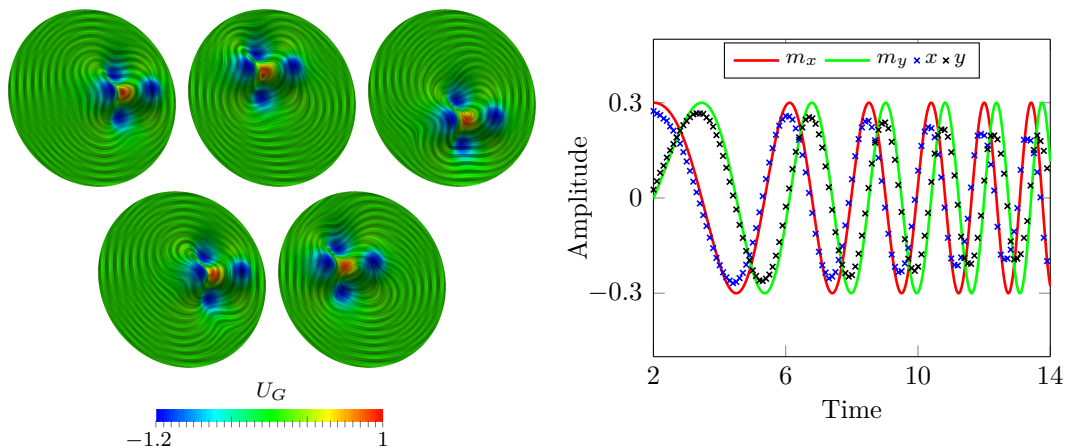
Figure 3.11: Evolution of $\widehat{\mathbf{v}}$ for the accelerated rotation of the Gaussian saddle for $t = 2, 7, 10, 12$ and 14 (left to right and top to bottom) visualized as noise concentration field aligned to the velocity field $\widehat{\mathbf{v}}$ (left) and evolution of the Gaussian Saddle location $(m_x, m_y)^T$ and the vortex location $(x, y)^T$ (right). The color coding is according to the geometric potential U_G.

Figure 3.10 (bottom, right). A different behavior is shown in Figure 3.11. Here, we use an initially higher angular velocity which also increases over time. In that case the inertial forces are higher than the geometric forces and the vortex is placed off the center of the Gaussian saddle. Figure 3.12 shows the Reynolds number against the angular velocity phase diagram, where the dependency of the geometric on the inertial forces can be observed.

3.7 Conclusion

The mathematical formulation of an incompressible fluid on a curved evolving surface is considered, for which the surface vorticity-stream function formulation is derived. The geometric terms in the incompressible surface Navier-Stokes equation induce a strong coupling between topology, geometry, defect interactions and hydrodynamics. On closed surfaces, topological constraints might require the presence of defects in the flow field. These defects interact with each other and respond to the local curvature as well as shape changes of the geometry. This leads to a highly nonlinear coupling, which can induce non-uniform surface flow and thus opens new possibilities to manipulate the interfacial hy-
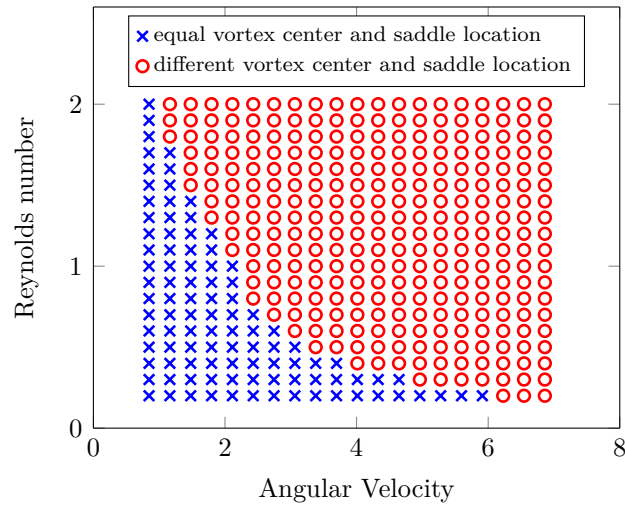
Figure 3.12: Reynolds number against angular velocity phase diagram. Here it is assumed that the vortex is placed off the Gaussian saddle if $||(m_x, m_y)^T - (x, y)^T|| \geq 0.1$ (red circles). Blue crosses indicate high geometric influences through vortex trapping.

drodynamics. We have demonstrated this interplay on various examples using a surface vorticity-stream function formulation, which is numerically solved by using the standard surface finite element method. Within the numerical treatment we have assumed all geometric quantities, such as the mean and Gaussian curvature, $\mathcal{H}$ and κ, the shape operator $\mathcal{B}$ and the normal vector $\boldsymbol{\nu}$, to be given analytically or computable at the required accuracy. For the example of the Stanford bunny we have used gradient recovery strategies to approximate the shape operator and the mean and Gaussian curvature. For more general surfaces or generalizations of the model, in which the normal velocity $v_{\boldsymbol{\nu}}$ is not specified but follows from conservation laws, the computation of $\mathcal{H}$, κ, $\mathcal{B}$ and $\boldsymbol{\nu}$ requires more care.

4 | Solving the incompressible surface Navier-Stokes equation

Due to the limitations of the proposed vorticity-stream function approach in Chapter 3, we consider a numerical approach for the incompressible surface Navier-Stokes equation, which is applicable on surfaces with arbitrary genus $g(\mathcal{S})$. The approach is based on the Cartesian extension of the equation, a Chorin projection method and discretization in space by surface finite elements. We study the experimental order of convergence of the proposed Chorin projection method and compare simulation results with discrete exterior calculus simulations on a torus. The interplay of the flow field with the topology is demonstrated by showing realizations of the Poincaré-Hopf theorem on n-tori. Additionally, the strong influence of shape changes on the flow field is shown in an example based on a non-uniform evolution of the nonic surface. The main content of this chapter is based on the author's publication [RV18b], but is extended to evolving surfaces.

Contents

4.1 Model formulation

The vorticity-stream function formulation from Chapter 3 is very appealing since the pressure is dropped, the saddle point structure of the equations is removed and the incompressibility constraint is automatically fulfilled. But the main disadvantage, namely that this method is restricted to surfaces with genus $g(\mathcal{S}) = 0$, requires further numerical approaches to circumvent this issue. One possibility is to directly solve the incompressible surface Navier-Stokes equation (2.28)-(2.29) by using discrete exterior calculus, see, e. g., [NRV17], which is not the purpose of this chapter. Here, we propose an approach based on the extended version of the incompressible surface Navier-Stokes equation (2.33)-(2.34). This allows us to split the vector-valued problem into a set of coupled scalar-valued problems for each component for which, e. g., surface finite elements can be used. Thus, we recall the alternative form of the incompressible surface Navier-Stokes equation (2.35)-(2.36) with $\widehat{\mathbf{f}} = 0$, i. e.

$$\boldsymbol{\pi}\partial_t\widehat{\mathbf{v}} + \boldsymbol{\nabla}_{\widehat{\mathbf{v}}}\widehat{\mathbf{v}} - v_{\boldsymbol{\nu}}\mathcal{B}\widehat{\mathbf{v}} - v_{\boldsymbol{\nu}}\nabla_{\mathcal{S}}v_{\boldsymbol{\nu}} = -\nabla_{\mathcal{S}}p + \frac{1}{\mathrm{Re}}\left(\mathrm{Rot}_{\mathcal{S}}\,\mathrm{rot}_{\mathcal{S}}\,\widehat{\mathbf{v}} + 2\kappa\widehat{\mathbf{v}} + 2\mathcal{H}\nabla_{\mathcal{S}}v_{\boldsymbol{\nu}}\right)$$
$$- \frac{2}{\mathrm{Re}}\mathcal{B}\nabla_{\mathcal{S}}v_{\boldsymbol{\nu}} - \alpha_{\mathbf{v}}\left(\widehat{\mathbf{v}}\cdot\boldsymbol{\nu}\right)\boldsymbol{\nu}$$
$$\mathrm{div}_{\mathcal{S}}\,\widehat{\mathbf{v}} - v_{\boldsymbol{\nu}}\mathcal{H} = 0$$

on $\mathcal{S} = \mathcal{S}(t)$ with the initial condition $\widehat{\mathbf{v}}\left(\cdot, t\right)|_{t=0} = \widehat{\mathbf{v}}_0(\cdot)$. As in Chapter 2, $\widehat{\mathbf{v}}$ denotes the extended surface velocity, p the surface pressure, $\boldsymbol{\pi}$ the tangential projection operator, $\mathcal{B}$ the shape operator, $\mathcal{H}$ the mean curvature, κ the Gaussian curvature, $v_{\boldsymbol{\nu}}$ the normal velocity, $\boldsymbol{\nu}$ the surface normal vector, Re the surface Reynolds number and $\alpha_{\mathbf{v}}$ the penalization parameter to weakly ensure the extended velocity $\widehat{\mathbf{v}}$ to be tangential. Furthermore, we use the alternative version of the transport term $\boldsymbol{\nabla}_{\widehat{\mathbf{v}}}\widehat{\mathbf{v}}$ from Section 3.1, i. e. $\boldsymbol{\nabla}_{\widehat{\mathbf{v}}}\widehat{\mathbf{v}} = \frac{1}{2}\nabla_{\mathcal{S}}(\widehat{\mathbf{v}}\cdot\widehat{\mathbf{v}}) + \mathrm{rot}_{\mathcal{S}}\,\widehat{\mathbf{v}}\boldsymbol{\nu}\times\widehat{\mathbf{v}}$, and $\bar{p} = p + \frac{1}{2}\widehat{\mathbf{v}}\cdot\widehat{\mathbf{v}}$ to obtain

$$\boldsymbol{\pi}\partial_t\widehat{\mathbf{v}} + \mathrm{rot}_{\mathcal{S}}\,\widehat{\mathbf{v}}\boldsymbol{\nu}\times\widehat{\mathbf{v}} - v_{\boldsymbol{\nu}}\mathcal{B}\widehat{\mathbf{v}} = -\nabla_{\mathcal{S}}\bar{p} + \frac{1}{\mathrm{Re}}\left(\mathrm{Rot}_{\mathcal{S}}\,\mathrm{rot}_{\mathcal{S}}\,\widehat{\mathbf{v}} + 2\kappa\widehat{\mathbf{v}}\right)$$
$$+ \mathbf{f}_G - \alpha_{\mathbf{v}}\left(\widehat{\mathbf{v}}\cdot\boldsymbol{\nu}\right)\boldsymbol{\nu} \tag{4.1}$$
$$\mathrm{div}_{\mathcal{S}}\,\widehat{\mathbf{v}} - v_{\boldsymbol{\nu}}\mathcal{H} = 0\,, \tag{4.2}$$

where we used the abbreviation

$$\mathbf{f}_G := \frac{2}{\mathrm{Re}} \left(\mathcal{H} \nabla_\mathcal{S} v_\nu - \mathcal{B} \nabla_\mathcal{S} v_\nu \right) + v_\nu \nabla_\mathcal{S} v_\nu \tag{4.3}$$

for better readability. The advantage of equations (4.1) and (4.2) is that they can be solved for each component $\widehat{\mathbf{v}}_x$, $\widehat{\mathbf{v}}_y$, $\widehat{\mathbf{v}}_z$ of $\widehat{\mathbf{v}} = (\widehat{\mathbf{v}}_x, \widehat{\mathbf{v}}_y, \widehat{\mathbf{v}}_z)^T$ and $\bar{p}$ using standard approaches for scalar-valued problems on surfaces, such as the surface finite element method [DE07b, DE07a, DE13], levelset approaches [BCOS01, GBS06, SV08, DE08], diffuse interface approximations [RV06] or trace finite element methods [Reu14].

In order to numerically solve equations (4.1) and (4.2) we will later use the standard surface finite element method. Within this method, the $\mathrm{Rot}_\mathcal{S}\, \mathrm{rot}_\mathcal{S}\, \widehat{\mathbf{v}}$ term in equation (4.1) leads to a heavy workload in terms of implementation and assembly time, since 36 second order operators, 72 first order operators and 36 zero order operators have to be considered. This effort can drastically be reduced by rotating the velocity field by an anlge of $\pi/2$ in the tangent space. Instead of $\widehat{\mathbf{v}}$, we consider the rotated velocity $\widehat{\mathbf{w}} := \boldsymbol{\nu} \times \widehat{\mathbf{v}}$ as unknown and apply $\boldsymbol{\nu} \times$ to equation (4.1). Thus, we obtain

$$\boldsymbol{\pi} \partial_t \widehat{\mathbf{w}} - \mathrm{div}_\mathcal{S}\, \widehat{\mathbf{w}} \boldsymbol{\nu} \times \widehat{\mathbf{w}} = -\mathrm{Rot}_\mathcal{S}\, \bar{p} + \frac{1}{\mathrm{Re}} \left(\nabla_\mathcal{S}\, \mathrm{div}_\mathcal{S}\, \widehat{\mathbf{w}} + 2\kappa \widehat{\mathbf{w}} \right)$$
$$- v_\nu \boldsymbol{\nu} \times \left(\mathcal{B} \left(\boldsymbol{\nu} \times \widehat{\mathbf{w}} \right) \right) + \mathbf{f}_G^\perp - \alpha_{\mathbf{w}} \left(\widehat{\mathbf{w}} \cdot \boldsymbol{\nu} \right) \boldsymbol{\nu} \tag{4.4}$$
$$\mathrm{rot}_\mathcal{S}\, \widehat{\mathbf{w}} - v_\nu \mathcal{H} = 0 \tag{4.5}$$

with the initial condition $\widehat{\mathbf{w}}\left(\cdot, t\right)\big|_{t=0} = \boldsymbol{\nu} \times \widehat{\mathbf{v}}_0(\cdot) =: \widehat{\mathbf{w}}_0(\cdot)$. Thereby, we have used $\mathbf{f}_G^\perp := \boldsymbol{\nu} \times \mathbf{f}_G$ and the identities $\mathrm{rot}_\mathcal{S}\, \widehat{\mathbf{v}} = -\mathrm{div}_\mathcal{S}\, \widehat{\mathbf{w}}$, $\mathrm{div}_\mathcal{S}\, \widehat{\mathbf{v}} = \mathrm{rot}_\mathcal{S}\, \widehat{\mathbf{w}}$, $\widehat{\mathbf{v}} = -\boldsymbol{\nu} \times \widehat{\mathbf{w}}$ as well as $\boldsymbol{\nu} \times \left(\boldsymbol{\nu} \times \widehat{\mathbf{v}} \right) = -\widehat{\mathbf{v}}$. Additionally, we added the respective penalty term to weakly ensure the rotated velocity $\widehat{\mathbf{w}}$ to be tangential. The $\nabla_\mathcal{S}\, \mathrm{div}_\mathcal{S}\, \widehat{\mathbf{w}}$ term now contains only nine second order terms and the remaining terms are of similar complexity as in equations (4.1) and (4.2). Note that in the language of exterior calculus system (4.4)-(4.5) is the so-called Hodge dual formulation of equations (4.1) and (4.2).

Remark. *Consider the surface $\mathcal{S}$ to be stationary, i. e. $v_\nu = 0$. Immediately,*

$\mathbf{f}_G = \mathbf{f}_G^{\perp} = \mathbf{0}$ *and thus we obtain*

$$\partial_t \widehat{\mathbf{v}} + \operatorname{rot}_{\mathcal{S}} \widehat{\mathbf{v}} \boldsymbol{\nu} \times \widehat{\mathbf{v}} = -\nabla_{\mathcal{S}} \bar{p} + \frac{1}{\text{Re}} \left(\operatorname{Rot}_{\mathcal{S}} \operatorname{rot}_{\mathcal{S}} \widehat{\mathbf{v}} + 2\kappa \widehat{\mathbf{v}} \right) - \alpha_{\mathbf{v}} \left(\widehat{\mathbf{v}} \cdot \boldsymbol{\nu} \right) \boldsymbol{\nu} \qquad (4.6)$$

$$\operatorname{div}_{\mathcal{S}} \widehat{\mathbf{v}} = 0 \,. \qquad (4.7)$$

Analogously, the rotated version is given by

$$\partial_t \widehat{\mathbf{w}} - \operatorname{div}_{\mathcal{S}} \widehat{\mathbf{w}} \boldsymbol{\nu} \times \widehat{\mathbf{w}} = -\operatorname{Rot}_{\mathcal{S}} \bar{p} + \frac{1}{\text{Re}} \left(\nabla_{\mathcal{S}} \operatorname{div}_{\mathcal{S}} \widehat{\mathbf{w}} + 2\kappa \widehat{\mathbf{w}} \right) - \alpha_{\mathbf{w}} \left(\widehat{\mathbf{w}} \cdot \boldsymbol{\nu} \right) \boldsymbol{\nu} \quad (4.8)$$

$$\operatorname{rot}_{\mathcal{S}} \widehat{\mathbf{w}} = 0 \,. \qquad (4.9)$$

4.2 Numerical approach

4.2.1 Chorin projection algorithm

First, we state the Chorin projection algorithm for the non-rotated system (4.1)-(4.2). Afterwards, we show that this method is also applicable for the rotated formulation (4.4)-(4.5). Let $0 = t_0 < t_1 < t_2 < \ldots$ be a sequence of discrete times with time step width $\tau^m := t_m - t_{m-1}$, where m denotes the time step number. The fields $\widehat{\mathbf{v}}^m = \widehat{\mathbf{v}}(\cdot, t)|_{t=t_m}$, $\widehat{\mathbf{w}}^m = \widehat{\mathbf{w}}(\cdot, t)|_{t=t_m}$ and $\bar{p}^m = \bar{p}(\cdot, t)|_{t=t_m}$ correspond to the time-discrete functions at time t_m. All other quantities are considered at time $t = t_m$ in the following time discrete equations, i.e. $\boldsymbol{\nu} = \boldsymbol{\nu}(\cdot, t)|_{t=t_m}$, $\boldsymbol{\pi} = \boldsymbol{\pi}(\cdot, t)|_{t=t_m}$, $\mathcal{H} = \mathcal{H}(\cdot, t)|_{t=t_m}$, $\kappa = \kappa(\cdot, t)|_{t=t_m}$, $\mathcal{B} = \mathcal{B}(\cdot, t)|_{t=t_m}$ and $v_{\boldsymbol{\nu}} = v_{\boldsymbol{\nu}}(\cdot, t)|_{t=t_m}$. Therefore, we omit indexing with the timestep number for better readability (unless it is explicitly needed). Following [Cho68], we ignore the pressure gradient term in equation (4.1) to find a so-called intermediate velocity $\widehat{\mathbf{v}}^{\star}$ and replace equation (4.2) by a Poisson equation to determine the pressure $\bar{p}^m$ in each time step. Furthermore, let $\mathrm{d}_{\tau^m}^{\widehat{\mathbf{v}}} := \frac{1}{\tau^m} \left(\widehat{\mathbf{v}}^{\star} - \boldsymbol{\pi} \widehat{\mathbf{v}}^{m-1} \right)$ be the discrete time derivative of the velocity $\widehat{\mathbf{v}}$. Analogously, we define the discrete time derivative of the rotated velocity $\widehat{\mathbf{w}}$ by $\mathrm{d}_{\tau^m}^{\widehat{\mathbf{w}}} := \frac{1}{\tau^m} \left(\widehat{\mathbf{w}}^{\star} - \boldsymbol{\pi} \widehat{\mathbf{w}}^{m-1} \right)$. Thus, by using a semi-implicit Euler time stepping scheme we finally get the following time discrete problem for the non-rotated equations (4.1) and (4.2):

Problem 4.1. *Let $\widehat{\mathbf{v}}_0$ be a sufficiently smooth initial velocity field. For $m =$*

$1, 2, 3, \ldots$ *find*

(i) $\widehat{\mathbf{v}}^\star$ *such that*

$$\mathrm{d}_{\tau^m}^{\widehat{\mathbf{v}}} + \mathrm{rot}_\mathcal{S}\,\widehat{\mathbf{v}}^\star \boldsymbol{\nu} \times \widehat{\mathbf{v}}^{m-1} - v_{\boldsymbol{\nu}}\mathcal{B}\widehat{\mathbf{v}}^\star = \frac{1}{\mathrm{Re}}\left(\mathrm{Rot}_\mathcal{S}\,\mathrm{rot}_\mathcal{S}\,\widehat{\mathbf{v}}^\star + 2\kappa\widehat{\mathbf{v}}^\star\right)$$
$$+ \mathbf{f}_G - \alpha_{\mathbf{v}}\left(\widehat{\mathbf{v}}^\star \cdot \boldsymbol{\nu}\right)\boldsymbol{\nu}\,,$$

(ii) $\bar{p}^{n+1}$ *such that*

$$\tau^m \Delta_\mathcal{S}\bar{p}^m = \mathrm{div}_\mathcal{S}\,\widehat{\mathbf{v}}^\star - v_{\boldsymbol{\nu}}\mathcal{H}\,,$$

(iii) $\widehat{\mathbf{v}}^m$ *such that*

$$\widehat{\mathbf{v}}^m = \widehat{\mathbf{v}}^\star - \tau^m\nabla_\mathcal{S}\bar{p}^m\,.$$

The new velocity $\widehat{\mathbf{v}}^m$, determined by Problem 4.1, satisfies the incompressibility condition (4.2), i.e.

$$\begin{aligned}\mathrm{div}_\mathcal{S}\,\widehat{\mathbf{v}}^m &= \mathrm{div}_\mathcal{S}\left(\widehat{\mathbf{v}}^\star - \tau^m\nabla_\mathcal{S}\bar{p}^m\right) = \mathrm{div}_\mathcal{S}\,\widehat{\mathbf{v}}^\star - \tau^m\Delta_\mathcal{S}\bar{p}^m\\ &= \mathrm{div}_\mathcal{S}\,\widehat{\mathbf{v}}^\star - \left(\mathrm{div}_\mathcal{S}\,\widehat{\mathbf{v}}^\star - v_{\boldsymbol{\nu}}\mathcal{H}\right) = v_{\boldsymbol{\nu}}\mathcal{H}\,.\end{aligned}$$

However, the corresponding scheme for the rotated formulation (4.4)-(4.5) follows by defining $\widehat{\mathbf{w}}^\star = \boldsymbol{\nu} \times \widehat{\mathbf{v}}^\star$ and applying $\boldsymbol{\nu}\times$ to the equation in step (*i*) of Problem 4.1 as above. Thus, we obtain:

Problem 4.2. *Let* $\widehat{\mathbf{v}}_0$ *be a sufficiently smooth initial velocity field and let* $\widehat{\mathbf{w}}_0 := \boldsymbol{\nu} \times \widehat{\mathbf{v}}_0$. *For* $m = 1, 2, 3, \ldots$ *find*

(i) $\widehat{\mathbf{w}}^\star$ *such that*

$$\mathrm{d}_{\tau^m}^{\widehat{\mathbf{w}}} - \mathrm{div}_\mathcal{S}\,\widehat{\mathbf{w}}^\star \boldsymbol{\nu} \times \widehat{\mathbf{w}}^{m-1} = \frac{1}{\mathrm{Re}}\left(\nabla_\mathcal{S}\,\mathrm{div}_\mathcal{S}\,\widehat{\mathbf{w}}^\star + 2\kappa\widehat{\mathbf{w}}^\star\right) + \mathbf{f}_G^\perp$$
$$- v_{\boldsymbol{\nu}}\boldsymbol{\nu} \times \left(\mathcal{B}\left(\boldsymbol{\nu} \times \widehat{\mathbf{w}}^\star\right)\right) - \alpha_{\mathbf{w}}\left(\widehat{\mathbf{w}}^\star \cdot \boldsymbol{\nu}\right)\boldsymbol{\nu}\,,$$

(ii) $\bar{p}^m$ *such that*

$$\tau^m \Delta_{\mathcal{S}} \bar{p}^m = \mathrm{rot}_{\mathcal{S}} \, \widehat{\mathbf{w}}^{\star} - v_{\boldsymbol{\nu}} \mathcal{H} \, ,$$

(iii) $\widehat{\mathbf{w}}^m$ *such that*

$$\widehat{\mathbf{w}}^m = \widehat{\mathbf{w}}^{\star} - \tau^m \, \mathrm{Rot}_{\mathcal{S}} \, \bar{p}^m \, ,$$

(iv) $\widehat{\mathbf{v}}^m$ *such that*

$$\widehat{\mathbf{v}}^m = -\boldsymbol{\nu} \times \widehat{\mathbf{w}}^m \, .$$

One of the main advantages of the projection scheme is that the equations has no longer a saddle point structure. This typically opens a broader set of applicable linear solvers (especially iterative solvers for large systems), if finite elements for spacial discretization are used. In contrast to the original saddle point problem, the pressure is determined by a Poisson equation in the projection scheme. However, on surfaces with boundaries or in flat space, this requires the specification of boundary conditions for the pressure. This directly affects the velocity on the boundaries due to the pressure correction step in the above algorithms. In other words, the numerical error of the Chorin projection scheme drastically increases in the near of the boundaries in that cases. This is a remarkable disadvantage and maybe the reason, why it is less often used in numerical simulations in bounded domains. In all cases of this thesis, in which the Chorin projection algorithm is used, this issue is implicitly circumvented, since only surfaces without boundaries are considered.

4.2.2 Pressure relaxation schemes

As already stated, the equation to determine the pressure $\bar{p}$ in step *(ii)* of Problem 4.1 and Problem 4.2 is a Poisson equation. Sometimes, especially when the timestep width τ^m is *small* or the right hand side is *big* compared to the left hand side, solving this equation requires more care. In the following, we present

two possible improvements to handle these issues – one, which iterates over the correction steps and another, which introduces a relaxation scheme.

Algorithm 4.1 (Iteration). *If the steps (ii) and (iii) of Problem 4.1 are numerically solved, an approximation error emerge in the solution of these equations. Therefore, we loop over the correction step by the following scheme. For $l = 1, 2, 3, ...,$ successively solve*

$$\tau^m \Delta_{\mathcal{S}} \bar{p}^{m,l} = \mathrm{div}_{\mathcal{S}} \, \widehat{\mathbf{v}}^{\star,l-1} - v_{\boldsymbol{\nu}} \mathcal{H} \tag{4.10}$$

$$\widehat{\mathbf{v}}^{\star,l} = \widehat{\mathbf{v}}^{\star,l-1} - \tau^m \nabla_{\mathcal{S}} \bar{p}^{m,l} \tag{4.11}$$

with $\widehat{\mathbf{v}}^{\star,0} = \widehat{\mathbf{v}}^{\star}$ determined by step (i) of Problem 4.1. Finally, the equations in steps (ii) and (iii) of Problem 4.1 are replaced by the equations (4.10) and (4.11) and the new velocity is given by $\widehat{\mathbf{v}}^m := \widehat{\mathbf{v}}^{\star,l}$ for $l \to \infty$. The same idea can be easily applied for Problem 4.2. The corresponding scheme reads: For $l = 1, 2, 3, ...,$ successively solve

$$\tau^m \Delta_{\mathcal{S}} \bar{p}^{m,l} = \mathrm{rot}_{\mathcal{S}} \, \widehat{\mathbf{w}}^{\star,l-1} - v_{\boldsymbol{\nu}} \mathcal{H} \tag{4.12}$$

$$\widehat{\mathbf{w}}^{\star,l} = \widehat{\mathbf{w}}^{\star,l-1} - \tau^m \, \mathrm{Rot}_{\mathcal{S}} \, \bar{p}^{m,l} \tag{4.13}$$

with $\widehat{\mathbf{w}}^{\star,0} = \widehat{\mathbf{w}}^{\star}$ determined by step (i) of Problem 4.2 and the equations in steps (ii) and (iii) of Problem 4.2 are replaced by the equations (4.12) and (4.13). The new rotated velocity is given by $\widehat{\mathbf{w}}^m := \widehat{\mathbf{w}}^{\star,l}$ for $l \to \infty$.

Algorithm 4.2 (Relaxation [NRV18]). *The solution of the equation in step (ii) of Problem 4.1 can be seen as the steady-state solution of a heat conduction equation with a source/sink term determined by the right hand side of this equation, i. e.*

$$\partial_{\tilde{t}} \bar{p}^m - \tau^m \Delta_{\mathcal{S}} \bar{p}^m = - \mathrm{div}_{\mathcal{S}} \, \widehat{\mathbf{v}}^{\star} + v_{\boldsymbol{\nu}} \mathcal{H}$$

for $\tilde{t} \to \infty$, where $\tilde{t}$ is the time on a newly introduced relaxation timescale. Therefore, we discretize this equation in time by an implicit Euler scheme, i. e.

$$\frac{1}{\tilde{\tau}} \left(\bar{p}^{m,l} - \bar{p}^{m,l-1} \right) - \tau^m \Delta_{\mathcal{S}} \bar{p}^{m,l} = - \mathrm{div}_{\mathcal{S}} \, \widehat{\mathbf{v}}^{\star} + v_{\boldsymbol{\nu}} \mathcal{H} \,, \tag{4.14}$$

where $\tilde{\tau}$ denotes the relaxation timestep with and l the relaxation timestep number. Finally, the equation in step (ii) of Problem 4.1 is replaced by equation (4.14) and $\bar{p}^m := \bar{p}^{m,l}$ for $l \to \infty$ is used in the pressure correction step (ii) of Problem 4.1. The same idea can be easily applied for Problem 4.2 with $\mathrm{rot}_\mathcal{S}\,\widehat{\mathbf{w}}^\star$ instead of $\mathrm{div}_\mathcal{S}\,\widehat{\mathbf{v}}^\star$ in equation (4.14).

In this setting, a combination of both algorithms would also be possible. More precisely, Algorithm 4.1 can be applied to Algorithm 4.2 by iterating over equation (4.14). However, we expect a similar convergence behavior as for Algorithm 4.1 and therefore consider both algorithms in the following separately.

4.2.3 Space discretization

For the discretization in space we apply the surface finite element method for scalar-valued problems [DE13] for each component of the velocity field $\widehat{\mathbf{v}}$ and $\widehat{\mathbf{w}}$, respectively. Therefore, let $\mathcal{S}_h = \mathcal{S}_h(t)$ be an interpolation of the surface $\mathcal{S} = \mathcal{S}(t)$ such that

$$\mathcal{S}_h := \bigcup_{T \in \mathcal{T}} T$$

with a conforming surface triangulation $\mathcal{T} = \mathcal{T}(t)$ of mesh size h_M at time $t = t_m$. Here, we consider each space, set and quantity at time $t = t_m$ and therefore omit indexing with the timestep number m for better readability (unless it is explicitly needed). We use globally continuous, piecewise linear Lagrange surface finite elements and thus the finite element space reads

$$V_h = \left\{ v \in \mathcal{C}^0(\mathcal{S}_h) \mid v_{|T} \in \mathbb{P}^1(T),\ \forall T \in \mathcal{T} \right\}$$

with $\mathcal{C}^k(\mathcal{S}_h)$ the space of k-times continuously differentiable functions on $\mathcal{S}_h$ and $\mathbb{P}^r(T)$ the set of polynomial functions of degree r on $T \in \mathcal{T}$. The finite element space V_h is thereby used twice as trail and test space for the pressure $\bar{p}$ and the velocities $\widehat{\mathbf{v}}$ and $\widehat{\mathbf{w}}$. Furthermore, let $(\cdot, \cdot)$ denote the standard scalar product on $L^2(\mathcal{S}_h)$ with $L^2(\mathcal{S}_h)$ the space of square-integrable functions on $\mathcal{S}_h$.
The resulting fully discrete system of Problem 4.1 reads: For $m = 1, 2, 3, \ldots$ find

$\widehat{\mathbf{v}}^{\star} = (\widehat{\mathbf{v}}_x^{\star}, \widehat{\mathbf{v}}_y^{\star}, \widehat{\mathbf{v}}_z^{\star})^T \in V_h^3$ and $\bar{p}^m \in V_h$ such that $\forall \mathbf{u} = (\mathbf{u}_x, \mathbf{u}_y, \mathbf{u}_z)^T \in V_h^3, \forall q \in V_h$

$$
\left(\mathrm{d}\widehat{\frac{\mathbf{v}}{\tau}}^m + \mathrm{rot}_{\mathcal{S}}\,\widehat{\mathbf{v}}^{\star}\boldsymbol{\nu} \times \widehat{\mathbf{v}}^{m-1} - v_{\boldsymbol{\nu}}\mathcal{B}\widehat{\mathbf{v}}^{\star} - \mathbf{f}_G + \alpha_{\mathbf{v}}\left(\widehat{\mathbf{v}}^{\star}\cdot\boldsymbol{\nu}\right)\boldsymbol{\nu} \ , \ \mathbf{u} \right)
$$
$$
= -\frac{1}{\mathrm{Re}}\left(\mathrm{rot}_{\mathcal{S}}\,\widehat{\mathbf{v}}^{\star} \ , \ \mathrm{rot}_{\mathcal{S}}\,\mathbf{u} \right) + \frac{2}{\mathrm{Re}}\left(\kappa\widehat{\mathbf{v}}^{\star} \ , \ \mathbf{u} \right)
$$
$$
\left(\tau^m\nabla_{\mathcal{S}}\bar{p}^m - \widehat{\mathbf{v}}^{\star} \ , \ \nabla_{\mathcal{S}}q \right) = \left(v_{\boldsymbol{\nu}}\mathcal{H} \ , \ q \right),
$$

from which $\widehat{\mathbf{v}}^m$ can be computed according to step (iii) in Problem 4.1. Note that the corresponding finite element approximation for the i-th component of $\widehat{\mathbf{v}}^{\star}$ follows by testing with $\mathbf{u} = \xi\mathbf{e}_i$ for $\xi \in V_h$, where $\mathbf{e}_i$ is the i-th unit vector in $\mathbb{R}^3$. The resulting fully discrete system of Problem 4.2 reads: For $m = 1, 2, 3, \dots$ find $\widehat{\mathbf{w}}^{\star} = (\widehat{\mathbf{w}}_x^{\star}, \widehat{\mathbf{w}}_y^{\star}, \widehat{\mathbf{w}}_z^{\star})^T \in V_h^3, \bar{p}^m \in V_h$ such that $\forall \mathbf{u} = (\mathbf{u}_x, \mathbf{u}_y, \mathbf{u}_z)^T \in V_h^3, \forall q \in V_h$

$$
\left(\mathrm{d}\widehat{\frac{\mathbf{w}}{\tau}}^m - \mathrm{div}_{\mathcal{S}}\,\widehat{\mathbf{w}}^{\star}\boldsymbol{\nu} \times \widehat{\mathbf{w}}^{m-1} + v_{\boldsymbol{\nu}}\boldsymbol{\nu} \times \left(\mathcal{B}\left(\boldsymbol{\nu} \times \widehat{\mathbf{w}}^{\star}\right)\right) - \mathbf{f}_G^{\perp} + \alpha_{\mathbf{w}}\left(\widehat{\mathbf{w}}^{\star}\cdot\boldsymbol{\nu}\right)\boldsymbol{\nu} \ , \ \mathbf{u} \right)
$$
$$
= \frac{1}{\mathrm{Re}}\left(\mathrm{div}_{\mathcal{S}}\,\widehat{\mathbf{w}}^{\star} \ , \ \mathrm{div}_{\mathcal{S}}\,\mathbf{u} \right) + \frac{2}{\mathrm{Re}}\left(\kappa\widehat{\mathbf{w}}^{\star} \ , \ \mathbf{u} \right)
$$
$$
\left(\tau^m\nabla_{\mathcal{S}}\bar{p}^m + \boldsymbol{\nu} \times \widehat{\mathbf{w}}^{\star} \ , \ \nabla_{\mathcal{S}}q \right) = \left(v_{\boldsymbol{\nu}}\mathcal{H} \ , \ q \right),
$$

from which $\widehat{\mathbf{w}}^m$ and $\widehat{\mathbf{v}}^m$ can be computed according to steps (iii) and (iv) in Problem 4.2. Again, testing with $\mathbf{u} = \xi\mathbf{e}_i$ for $\xi \in V_h$ yields the corresponding finite element approximation for the i-th component of $\widehat{\mathbf{w}}^{\star}$.

In the following simulations, we additionally use the pressure relaxation schemes from Section 4.2.2, i. e. Algorithm 4.1 and Algorithm 4.2, but omit its finite element formulation, which can be analogously derived as above. In order to assemble and solve the resulting system, we again use the finite element toolbox AMDiS [VV07, WLPV15] with a domain decomposition approach to work on many-core-platforms. As linear solver we have used a BiCGStab(l) method with $l = 2$ and a Jacobi preconditioner. In the following, we exclusively consider the systems and algorithms for the rotated velocity $\widehat{\mathbf{w}}$ due to the expected reduced numerical cost. This reduction is quantified in Section 4.2.4.
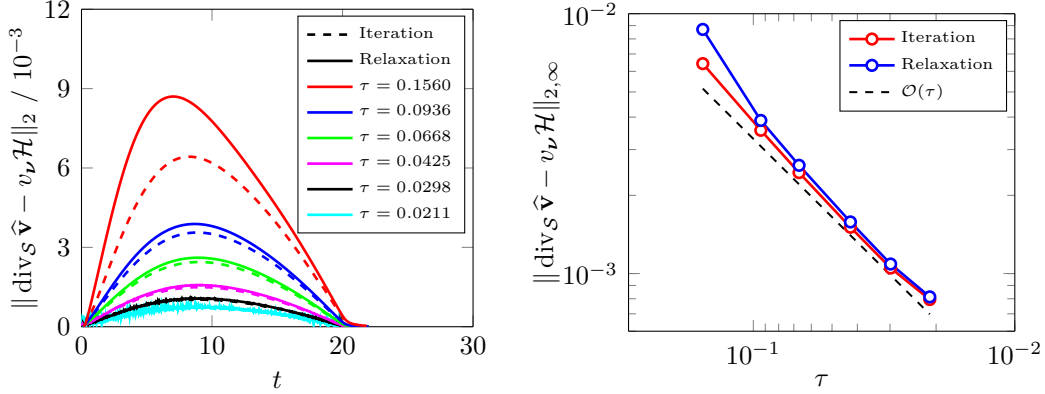
Figure 4.1: Continuity equation error $\|\operatorname{div}_{\mathcal{S}} \widehat{\mathbf{v}} - v_{\boldsymbol{\nu}}\mathcal{H}\|_2$ against time t (left) and continuity equation error $\|\operatorname{div}_{\mathcal{S}} \widehat{\mathbf{v}} - v_{\boldsymbol{\nu}}\mathcal{H}\|_{2,\infty}$ against timestep width τ (right) for both Algorithm 4.1 and Algorithm 4.2. Thereby, $\|\cdot\|_p$ denotes the spatial L^p norm and $\|\cdot\|_{p,q}$ denotes L^p norm in space and L^q norm in time.

4.2.4 Validation and comparison

First, we present a convergence study to numerically show the convergence in the timestep width τ^m for both Algorithm 4.1 and Algorithm 4.2. An ellipsoid with major axes $(0.7, 0.7, 1.2)$ is considered as starting geometry, which evolves by decreasing the third axis parameter to a sphere according to Figure 6.5 in Chapter 6. Thereby, the two other parameters are chosen such that they are equal to each other and the surface area is globally conserved over time. Furthermore, we use a constant timestep width $\tau = \tau^m$ and a fixed timestep-to-meshsize-ratio $\tau/h_{\mathrm{M}} = 2$ with mesh size h_{M} to have a constant Courant-Friedrichs-Lewy (CFL) condition for each considered timestep width. The Reynolds number Re is considered to be Re $= 1$ and the penalty parameter to ensure the tangentiality is choosen as $\alpha_{\mathbf{w}} = 10^3$. The evolution of the ellipsoid starts and ends smoothly following a half period of a sine function (cf. Figure 6.5 of Chapter 6) in the time period $[0, 20]$. We compute the solution of both projection methods, i.e. Algorithm 4.1 and Algorithm 4.2, for various timesteps and plot the error in the continuity equation $\|\operatorname{div}_{\mathcal{S}} \widehat{\mathbf{v}} - v_{\boldsymbol{\nu}}\mathcal{H}\|$ with a respective norm $\|\cdot\|$ against the time t as well as against the timestep width τ in Figure 4.1. Note that the continuity equation is not computed explicitly. In Table 4.1 the experimental order of convergence (EOC) in the timestep width τ is computed, where – as

τ	Iteration		Relaxation	
	$\|\operatorname{div}_{\mathcal{S}} \widehat{\mathbf{v}} - v_{\boldsymbol{\nu}} \mathcal{H}\|$	EOC	$\|\operatorname{div}_{\mathcal{S}} \widehat{\mathbf{v}} - v_{\boldsymbol{\nu}} \mathcal{H}\|$	EOC
0.1560	$6.43 \cdot 10^{-3}$	–	$8.70 \cdot 10^{-3}$	–
0.0936	$3.56 \cdot 10^{-3}$	1.16	$3.88 \cdot 10^{-3}$	1.58
0.0668	$2.45 \cdot 10^{-3}$	1.11	$2.61 \cdot 10^{-3}$	1.18
0.0425	$1.51 \cdot 10^{-3}$	1.07	$1.58 \cdot 10^{-3}$	1.11
0.0298	$1.05 \cdot 10^{-3}$	1.02	$1.09 \cdot 10^{-3}$	1.05
0.0211	$0.80 \cdot 10^{-3}$	0.81	$0.81 \cdot 10^{-3}$	0.84

Table 4.1: Experimental order of convergence (EOC) for the continuity equation error $\|\operatorname{div}_{\mathcal{S}} \widehat{\mathbf{v}} - v_{\boldsymbol{\nu}} \mathcal{H}\|$ with respect to the timestep width τ. Thereby, $\|\cdot\| := \|\cdot\|_{p,q}$ denotes L^p norm in space and L^q norm in time.

DOFs	$t_{\widehat{\mathbf{v}}}/\mathrm{ms}$	$t_{\widehat{\mathbf{w}}}/\mathrm{ms}$	$t_{\widehat{\mathbf{v}}}/t_{\widehat{\mathbf{w}}}$
1158	271	5	55
2310	544	8	65
4614	1123	16	72
9222	2200	32	70
18438	4369	69	63
36870	8818	157	56
73734	17920	327	55
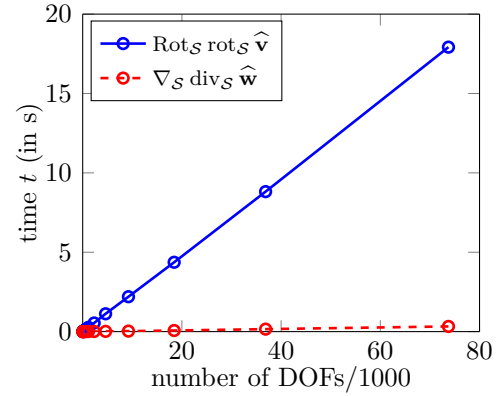
Figure 4.2: Assembly times $t_{\widehat{\mathbf{v}}}$ and $t_{\widehat{\mathbf{w}}}$ (in ms) for the two second order operators $\operatorname{Rot}_{\mathcal{S}} \operatorname{rot}_{\mathcal{S}} \widehat{\mathbf{v}}$ and $\nabla_{\mathcal{S}} \operatorname{div}_{\mathcal{S}} \widehat{\mathbf{w}}$, respectively, as a function of the number of DOFs.

in Figure 4.1 – linear convergence in τ can be observed. Algorithm 4.2 yields the same numerical results as the original projection method, i.e. Algorithm 4.1 with only one iteration.

However, both finite element approximations of Problem 4.1 and Problem 4.2 lead to the same results, but the computational cost for Problem 4.2 is reduced drastically. To quantify this reduction we compare the assembly time for the second order operators in Problem 4.1 and Problem 4.2, i.e. $\operatorname{Rot}_{\mathcal{S}} \operatorname{rot}_{\mathcal{S}} \widehat{\mathbf{v}}$ and $\nabla_{\mathcal{S}} \operatorname{div}_{\mathcal{S}} \widehat{\mathbf{w}}$, respectively. We consider a sphere and vary the triangulation $\mathcal{T}$. Figure 4.2 shows the assembly time as a function of degrees of freedom (DOFs).
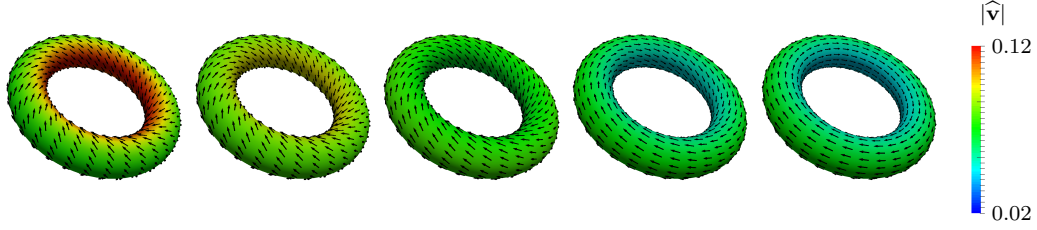
Figure 4.3: Velocity field $\widehat{\mathbf{v}} = -\boldsymbol{\nu} \times \widehat{\mathbf{w}}$ at $t = 0$, 2, 10, 30 and 60 (left to right). The arrows are rescaled for better visualization. The color coding is according to the absolute value of the velocity $\widehat{\mathbf{v}}$.

The time is the mean value of multiply runs of the assembly routine. The results indicate a reduction by a factor of approximately 50.

Next, we compare the numerical solution of Problem 4.2 in combination with Algorithm 4.1 with an example considered in [NRV17, Figure 7.8] using DEC. It uses a nontrivial solution based on harmonic vector fields with $\mathrm{div}_{\mathcal{S}}\,\widehat{\mathbf{v}} = 0$ and $\mathrm{rot}_{\mathcal{S}}\,\widehat{\mathbf{v}} = 0$, which can exist on surfaces with $g(\mathcal{S}) \neq 0$. Here, we use the same setting as in Section 3.4 and consider a torus, which has genus $g(\mathcal{S}) = 1$ and can be described by the levelset function $q(\boldsymbol{x}) = (\sqrt{x^2 + z^2} - R)^2 + y^2 - r^2$, with $\boldsymbol{x} = (x, y, z)^T \in \mathbb{R}^3$ with $\boldsymbol{x} = (x, y, z) \in \mathbb{R}^3$, major radius R and minor radius r. We use $R = 2$ and $r = 0.5$. Let φ and θ denote the standard parametrization angles on the torus. Thus, the two basis vectors can be written as $\partial_\varphi \boldsymbol{x} = (-z, 0, x)$ as well as $\partial_\theta \boldsymbol{x} = (-\frac{xy}{\sqrt{x^2 + z^2}}, \sqrt{x^2 + z^2} - 2, -\frac{yz}{\sqrt{x^2 + z^2}})$ and the two (linear independent) harmonic vector fields on the torus are given by

$$\widehat{\mathbf{v}}_\varphi^{\mathrm{harm}} = \frac{1}{4\,(x^2 + z^2)}\partial_\varphi \boldsymbol{x}$$

$$\widehat{\mathbf{v}}_\theta^{\mathrm{harm}} = \frac{1}{2\sqrt{x^2 + z^2}}\partial_\theta \boldsymbol{x}$$

according to Section 3.4. The example considers the mean of the two harmonic vector fields as initial condition, i.e. $\widehat{\mathbf{v}}_0 = \frac{1}{2}(\widehat{\mathbf{v}}_\varphi^{\mathrm{harm}} + \widehat{\mathbf{v}}_\theta^{\mathrm{harm}})$, and shows the evolution towards a Killing vector field, which is proportional to the basis vector $\partial_\varphi \boldsymbol{x}$. The surface Reynolds number is $\mathrm{Re} = 10$. Figure 4.3 shows the results obtained with the fully discrete scheme of Problem 4.2 in combination with Algorithm 4.1 with time step width $\tau^m = 0.1$ and penalization parameter $\alpha_{\mathbf{w}} =$
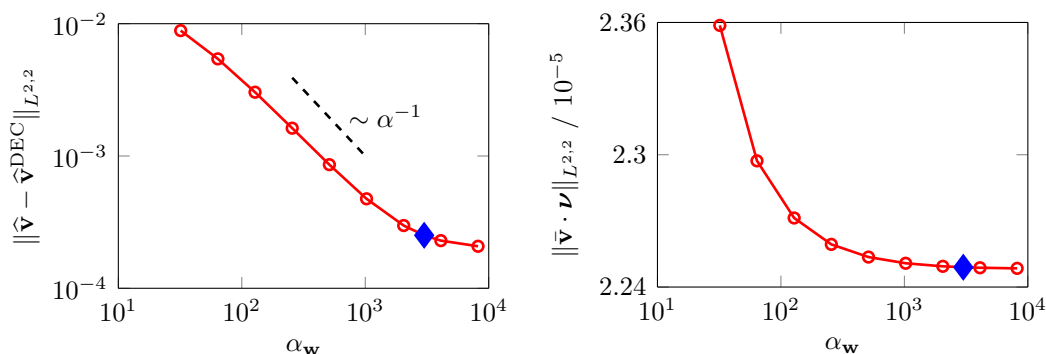
Figure 4.4: $L^{2,2}$ norm of the error between the velocity field $\widehat{\mathbf{v}}$ and the velocity field $\widehat{\mathbf{v}}^{\mathrm{DEC}}$ from [NRV17] using the DEC approach against the penalty parameter $\alpha_{\mathbf{w}}$ (left) and $L^{2,2}$ norm of the normal component of the rescaled velocity field $\bar{\mathbf{v}} = \widehat{\mathbf{v}}/\|\widehat{\mathbf{v}}\|_{L^2}$ against the penalty parameter $\alpha_{\mathbf{w}}$ (right). $L^{p,q}$ thereby denotes the L^p norm in space and L^q norm in time. The blue diamond indicates the penalty parameter $\alpha_{\mathbf{w}}$ used for visualization in Figure 4.3 and in the following examples.

3000 on the same mesh as considered in [NRV17]. For the Gaussian curvature κ we use the analytic formula. In Figure 4.4 (left) we compare $\widehat{\mathbf{v}}$ with $\widehat{\mathbf{v}}^{\mathrm{DEC}}$ for various $\alpha_{\mathbf{w}}$. Thereby, $\widehat{\mathbf{v}}^{\mathrm{DEC}}$ is the solution of the (local) incompressible surface Navier-Stokes equation (2.28)-(2.29) with $v_{\boldsymbol{\nu}} = 0$ from [NRV17] using the DEC approach. Within this approach, the velocity $\widehat{\mathbf{v}}^{\mathrm{DEC}}$ has a zero normal component by default. Again, first order convergence in $\alpha_{\mathbf{w}}$ can be obtained. In Figure 4.4 (right) we consider the rescaled velocity field $\bar{\mathbf{v}} = \widehat{\mathbf{v}}/\|\widehat{\mathbf{v}}\|_{L^2}$ in order to show that the penalization of the normal component $\bar{\mathbf{v}} \cdot \boldsymbol{\nu}$ is numerically satisfied. Using Algorithm 4.2 instead of Algorithm 4.1 leads to the same numerical results.

4.3 Simulation results

The Poincaré-Hopf theorem (2.19) relates the topology of the surface to analytic properties of a vector field on it. For vector fields $\widehat{\mathbf{v}}$ on the surface $\mathcal{S}$ with only finitely many zeros (defects), it holds

$$\sum_i \mathrm{ind}_V(\mathbf{d}_i) = 2 - 2g(\mathcal{S})$$
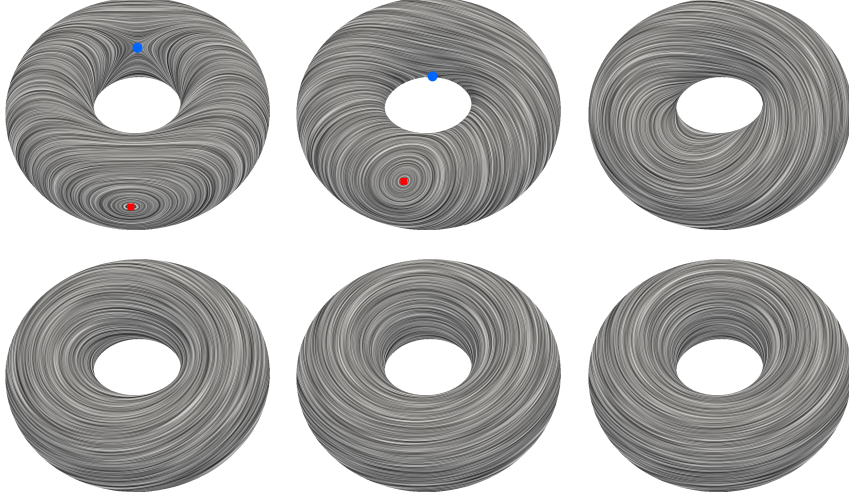
Figure 4.5: Velocity field $\widehat{\mathbf{v}} = -\boldsymbol{\nu} \times \widehat{\mathbf{w}}$ for the 1-torus at $t = 0, 5, 10, 15, 25$ and 100 (left to right and top to bottom) visualized as noise concentration field aligned to the velocity field $\widehat{\mathbf{v}}$. The red squares and blue circles are indicating $+1$ defects (vortices) and -1 defects (saddles), respectively.

with $\mathrm{ind}_V(\mathbf{d}_i)$ the index/winding number of $\widehat{\mathbf{v}}$ at defect position $\mathbf{d}_i$ and the genus $g(\mathcal{S})$ of the surface $\mathcal{S}$, cf. equation (2.19). To highlight this relation we consider n-tori for $n = 1, 2, 3$ with genus $1, 2$ and 3, respectively. Obviously, the simulation results have to fulfill the Poincaré-Hopf theorem in each time step, but they will also provide a realization of the theorem which depends on geometric properties and initial conditions. Similar relations have already been considered for surfaces with $g(\mathcal{S}) = 0$ in Chapter 3 and [RV15, RV18a, NRV17].

A general form of a levelset function for a n-torus can be written as $q_n(\boldsymbol{x}) = \prod_{i=1}^{n} T(\boldsymbol{x} - \mathbf{m}_i) - (n-1)\,\delta$ with a constant $\delta > 0$ and the midpoints of the tori $\mathbf{m}_i \in \mathbb{R}^3$ for $i = 1, \ldots, n$. In the following examples we consider the fully discrete scheme for Problem 4.2 in combination with Algorithm 4.1 and use $\mathrm{Re} = 10$, $\tau = \tau^m = 0.1$, $\alpha_{\mathbf{w}} = 3000$, $R = 1$ and $r = 0.5$. For the Gaussian curvature κ we use the analytic formula. The initial condition is considered to be $\widehat{\mathbf{v}}_0 = \mathrm{Rot}_{\mathcal{S}}\,\psi_0 = \boldsymbol{\nu} \times \nabla_{\mathcal{S}}\psi_0$ with $\psi_0 = \frac{1}{2}(x + y + z)$ which ensures the incompressibility constraint.

Figure 4.5 shows the time evolution on the 1-torus with $\mathbf{m}_1 = \mathbf{0}$. The initial state has four defects, two vortices with $\mathrm{ind}_V(\mathbf{d}_i) = +1$, indicated as red dots,
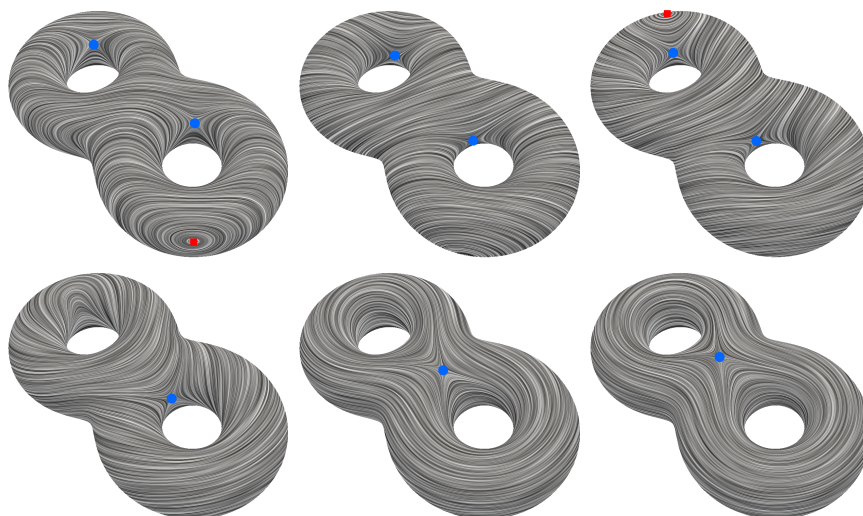
Figure 4.6: Velocity field $\widehat{\mathbf{v}} = -\boldsymbol{\nu} \times \widehat{\mathbf{w}}$ for the 2-torus at $t = 0, 10, 20, 30, 50$ and 100 (left to right and top to bottom) visualized as noise concentration field aligned to the velocity field $\widehat{\mathbf{v}}$. The red squares and blue circles are indicating $+1$ defects (vortices) and -1 defects (saddles), respectively.

and two saddles with $\text{ind}_V(\mathbf{d}_i) = -1$, indicated as blue dots (one vortex and one saddle are not visible). These defects annihilate during the evolution. The final state is again a Killing vector field without any defects, which yields a valid realization of the Poincaré-Hopf theorem (2.19).

For $n > 1$ the rotational symmetry is broken and Killing vector fields are no longer possible. Thus, we expect dissipation of the kinetic energy and convergence to $\widehat{\mathbf{v}} = \mathbf{0}$ for any initial condition. Figure 4.6 shows the time evolution on a 2-torus where we have used the midpoints $\mathbf{m}_1 = (-1.2, 0, 0)^T$ and $\mathbf{m}_2 = -\mathbf{m}_1$ as well as $\delta = 1$. The initial state has two vortices and four saddles and thus

$$\sum_i \text{ind}_V(\mathbf{d}_i) = -2 \,.$$

Two vortex-saddle pairs annihilate and the final defect configuration consists of two saddles located at the center of the 2-torus (one is not visible). The velocity field decays towards $\widehat{\mathbf{v}} = \mathbf{0}$. Figure 4.7 shows the time evolution on a 3-torus with $\delta = 10$ and midpoints $\mathbf{m}_1 = (-1.2, -0.75, 0)$, $\mathbf{m}_2 = (1.2, -0.75, 0)$ and
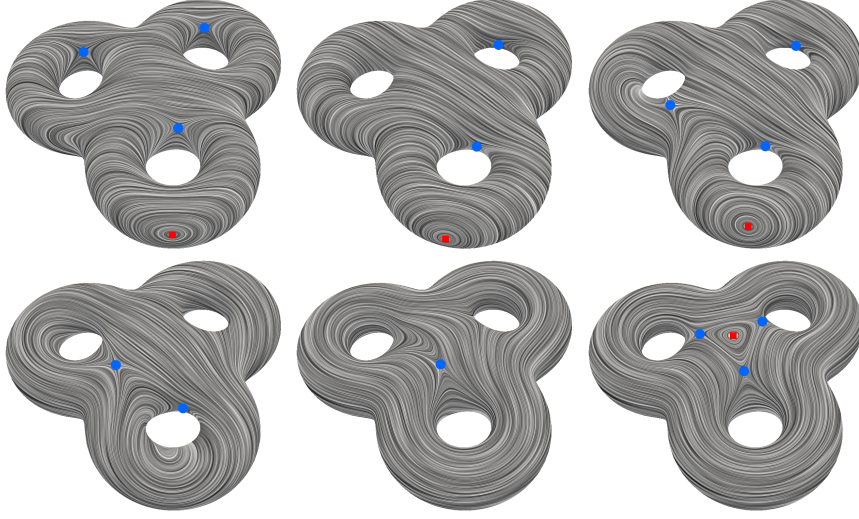
Figure 4.7: Velocity field $\widehat{\mathbf{v}} = -\boldsymbol{\nu} \times \widehat{\mathbf{w}}$ for the 3-torus at $t = 0$, 10, 20, 30, 50 and 100 (left to right and top to bottom) visualized as noise concentration field aligned to the velocity field $\widehat{\mathbf{v}}$. The red squares and blue circles are indicating $+1$ defects (vortices) and -1 defects (saddles), respectively.

$\mathbf{m}_3 = (0, 1.33, 0)$. Initially, we have three vortices and seven saddles and thus

$$\sum_i \mathrm{ind}_V(\mathbf{d}_i) = -4 \,,$$

which is also fulfilled for the final defect configuration with two vortices and six saddles at the center of the 3-torus (one vortex and three saddles are not visible). Again, the velocity field decays towards $\mathbf{v} = \mathbf{0}$.

In order to show the differences in the evolution on the n-tori before and after the final defect configuration is reached, we consider the H^1 semi-norm $|\cdot|_1$ of the rescaled velocity field $\bar{\mathbf{v}} = \widehat{\mathbf{v}}/\|\widehat{\mathbf{v}}\|_2$ with the L^2 norm $\|\cdot\|_2$. If the defects do not move, this quantity is constant. Figure 4.8 shows the evolution of $|\bar{\mathbf{v}}|_1$ over the time t together with the decay of the kinetic energy $\mathcal{F}^{\mathrm{kin}} = \frac{1}{2} \int_{\mathcal{S}} \|\widehat{\mathbf{v}}\|^2 \, \mathrm{d}\mathcal{S}$, which indicates a higher rate of dissipation for a surface with higher genus $g(\mathcal{S})$.

These results clearly show the strong interplay between topology, geometric properties and defect positions.

Now, we take the surface evolution into account and make use of a so-called nonic surface, see [NNPV18], which can be described as follows. Let $\mathbf{x}_{\mathbb{S}}$ be the
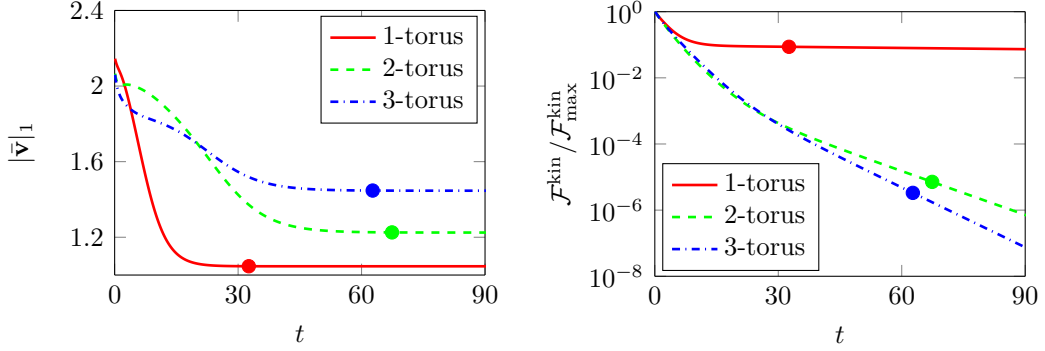
Figure 4.8: H^1 semi-norm $|\cdot|_1$ of the rescaled velocity field $\bar{\mathbf{v}} = \hat{\mathbf{v}}/\|\hat{\mathbf{v}}\|_{L^2}$ against time t (left) and normalized kinetic energy $\mathcal{F}^{\text{kin}}/\mathcal{F}^{\text{kin}}_{\max}$ against time t (right), where $\mathcal{F}^{\text{kin}}_{\max}$ is the maximum value of the kinetic energy $\mathcal{F}^{\text{kin}}$ over time. The colored dots are indicating the time points at which the defects reach their final position and only viscous dissipation takes place or a Killing vector field is reached. We identify these points if the decay rate of the H^1 semi-norm of the rescaled velocity field $\bar{\mathbf{v}}$ reaches 0.001% of its maximum value over time.

standard parametrization of the unit sphere $\mathbb{S}$ and let

$$f_{C,r}(z) := \frac{C}{4}z^2\left((z+1)^2(4-3z) + r(z-1)^2(4+3z)\right)$$

with $z \in \mathbb{R}$. The parametrization of the nonic surface is given by

$$\mathbf{x} = \mathbf{x}_{\mathbb{S}} + f_{C,r}(\cos\theta)\mathbf{e}_1 - B\sin\theta\sin\varphi\mathbf{e}_2$$

with the standard parametrization angles φ, θ of the unit sphere and the $\mathbb{R}^3$ unit vectors $\mathbf{e}_1$, $\mathbf{e}_1$ in x- and y-direction, respectively. The parameters C, B and r define the shape of the nonic surface. For $B = C = 0$ the parametrization $\mathbf{x}$ describes the unit sphere which motivates a surface evolution including the unit sphere and the nonic surface. Therefore, we consider the time dependent parameters

$$C = C(t) = \frac{1}{2}(1 - \cos(2\pi(t-t_0)/T))C_d$$
$$B = B(t) = 7/20\,C(t)$$
$$r = r(t) = \frac{1}{2}(1 - \cos(2\pi(t-t_0)/T))r_d$$
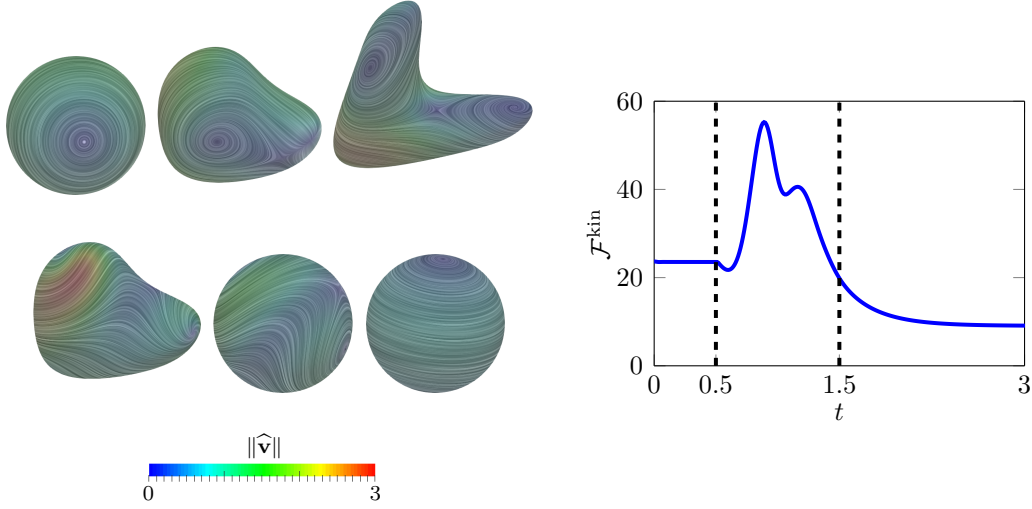
Figure 4.9: Left: Velocity field $\widehat{\mathbf{v}} = -\boldsymbol{\nu} \times \widehat{\mathbf{w}}$ on the evolving nonic surface at $t = 0.5, 0.75, 1.0, 1.25, 1.5$ and 3.5 (left to right and top to bottom) visualized as noise concentration field aligned to the velocity field $\widehat{\mathbf{v}}$. Right: Kinetic energy $\mathcal{F}^{\mathrm{kin}}$ against time t. Dashed lines indicate begin and end of the surface evolution. The color coding is according to the absolute value of the velocity field $\widehat{\mathbf{v}}$.

for $t \in (t_0, t_0 + T)$ with $C_d = 1.1$, $r_d = 0.95$, $t_0 = 0.5$ and $T = 1$. For $t < t_0$ and $t > t_0 + T$ we specify $C = B = r = 0$. To ensure global surface area conservation over time, $\mathbf{x}$ is rescaled in each time step such that the surface area is equal to the surface area of $\mathbf{x}|_{t=0}$. This leads to a surface evolution from the unit sphere to the nonic surface and vice versa until the unit sphere is reached again. We start with a Killing vector field for the velocity $\widehat{\mathbf{v}}$ on the sphere, i. e. $\widehat{\mathbf{v}}_0 = \mathrm{Rot}_{\mathcal{S}}\, \psi_0$ where $\psi_0 = 2.5\,(x + y)$ with $\boldsymbol{x} = (x, y, z)^T \in \mathcal{S}$, and fix the Reynolds number to be $\mathrm{Re} = 5$. All other parameters are treated as in the previous examples. Due to the scaling of the geometry for the global area conservation we cannot make use of the analytic formula for the geometric quantities. Therefore, we compute the normal vector $\boldsymbol{\nu}$ from the discrete surface mesh, from which the shape operator $\mathcal{B}$ and the curvatures $\mathcal{H}$ and κ can be computed according to Chapter 2. The simulation results for various times together with the surface kinetic energy over time is shown in Figure 4.9. The reached steady state solution after the evolution is again a Killing vector field at a lower energy level which is caused by the surface evolution itself and viscous dissipation during the non-constant Gaussian curvature period. Interestingly, the vortices in the final configuration

are significantly located off the vortex positions of the initial condition. Thus, besides dissipation the surface evolution causes a rotation of the killing vector field.

For further results on evolving surfaces, we refer to Chapter 6 where the incompressible surface Navier-Stokes equation on an evolving surface within a model for surface liquid crystals is used.

4.4 Conclusion

A discretization approach for the incompressible surface Navier-Stokes equation on general evolving surfaces independent of the genus $g(\mathcal{S})$ is proposed. The approach only requires standard ingredients which most finite element implementations can offer. It is based on a reformulation of the equation in Cartesian coordinates, penalization of the normal component, a Chorin projection method and discretization in space by the standard surface finite element method for each component. A further rotation of the velocity field leads to a drastic reduction of the complexity of the equation and the required computing time. The fully discrete scheme is described in detail and its accuracy is validated against a numerical solution based on DEC on a 1-torus, which has been considered in [NRV17, Figure 7.8]. Furthermore, a convergence study for the proposed Chorin projection method is presented and the interesting interplay between the topology of the surface, its geometric properties and defect dynamics in the flow field is shown on n-tori for $n = 1, 2, 3$. Additionally, a non-uniform surface evolution of the sphere based on the nonic surface is used in order to rotate a Killing vector field.

5 | Inextensible Newtonian fluid interfaces in viscous fluids

In this chapter, we consider an extension of the vorticity-stream function approach from Chapter 3 to model lipid membranes surrounded by viscous fluids. In the present setting the membranes are assumed to be stationary. We validate the results of the model and the numerical approach, which is based on a diffuse interface approximation, an operator splitting approach and a semi-implicit adaptive finite element discretization, against observed flow patterns in vesicles. These vesicles are adhered to a solid surface and are subjected to shear flow. The influence of the Gaussian curvature on the surface flow pattern on ellipsoidal vesicles is discussed.

The main content of this chapter is taken from the author's publication [RV16].

Contents

5.1 Overview

Lipid membranes behave as viscous fluids under physiological conditions. This interface fluidity is essential, e. g., for the mobility of proteins [SD75], fluid domains [CKV07] and lateral reorganizations [SV04]. However, even if the importance of membrane fluidity is recognized, it is only rarely accounted for in continuum modeling approaches. This might be due to the difficulty of solving and even formulating the governing equations for the membrane fluid flow.

Here, we consider an inextensible two-dimensional Newtonian fluid interface of arbitrary curvature embedded in a bulk fluid. In other words, an inextensible fluid interface has the property that it cannot be stretched or compressed. From a mathematical point of view this is equivalent to the incompressibility condition as used in the prior chapters. Thus, the model can be seen as an incompressible two-phase flow problem with an incompressible surface Navier-Stokes equation as interface condition. Similar problems within the Stokes limit and for special geometries have been considered in [HMS$^+$08, AD09, HL10, WG12, RDA13, HSWKG13]. Here, we focus on the coupling with the bulk fluid, but restrict the interface to be stationary. This already allows a comparison with an experiment [VMV07, HSWKG13] in which a vesicle was adhered to a solid surface and was subjected to a simple shear flow. The induced flow in the membrane has two vortices, which is due to the inextensibility of the membrane and in contrast to the toroidal circulation that would occur in the related problem of a drop of immiscible fluid attached to a surface and subject to shear flow [DV87]. The observed membrane and bulk flow patterns have already been theoretically predicted by [WG12, HSWKG13] using a Stokes approximation and a special hemispherical geometry of the vesicle. We will use these results to validate our numerical approach for the full Navier-Stokes problem with arbitrary curvature.

5.2 Sharp interface equations

Let $\mathcal{S}$ be a closed two-dimensional stationary interface separating two domains $\Omega_1 \subset \mathbb{R}^3$ and $\Omega_2 \subset \mathbb{R}^3$. The hydrodynamic equations for an incompressible fluid

in the outer phase Ω_1 and the inner phase Ω_2 read

$$\rho_i \left(\partial_t \mathbf{V}_i + (\mathbf{V}_i \cdot \nabla) \mathbf{V}_i\right) = -\nabla P_i + \eta_i \mathbf{\Delta} \mathbf{V}_i$$
$$\nabla \cdot \mathbf{V}_i = 0 \,,$$

where $\mathbf{V}_i$ is the fluid velocity, P_i the pressure, ρ_i the density and η_i the dynamic viscosity in Ω_i. Both systems are coupled through the no-slip interface condition

$$\mathbf{V}_i|_{\mathcal{S}} = \widehat{\mathbf{v}}$$

with the interfacial velocity $\widehat{\mathbf{v}}$ on $\mathcal{S}$, which results as solution of the incompressible surface Navier-Stokes equation on $\mathcal{S}$. Hence, we recall the dimensional formulation (2.26)-(2.27) for a stationary surface $\mathcal{S}$ with $v_{\boldsymbol{\nu}} = 0$, i.e.

$$\rho_{\mathcal{S}} \left(\partial_t \widehat{\mathbf{v}} + \mathbf{\nabla}_{\widehat{\mathbf{v}}} \widehat{\mathbf{v}}\right) = -\nabla_{\mathcal{S}} p + \eta_{\mathcal{S}} \left(-\mathbf{\Delta}^{\mathrm{dR}} \widehat{\mathbf{v}} + 2\kappa \widehat{\mathbf{v}}\right) + \widehat{\mathbf{f}} \tag{5.1}$$
$$\operatorname{div}_{\mathcal{S}} \widehat{\mathbf{v}} = 0 \,, \tag{5.2}$$

which is already extended to Cartesian coordinates according to Section 2.4 and Section 2.5, respectively. Thereby, $\widehat{\mathbf{v}}$ denotes the extended velocity field, p the interfacial pressure, $\widehat{\mathbf{f}}$ the extended external forces, $\rho_{\mathcal{S}}$ the surface density, $\eta_{\mathcal{S}}$ the surface dynamic viscosity, $\mathbf{\Delta}^{\mathrm{dR}}$ the Laplace-deRham operator and κ the Gaussian curvature. Note that by default the surface velocity $\widehat{\mathbf{v}}$ in system (5.1)-(5.2) is not necessarily tangential and a suitable penalty term according to Section 2.4 has to be considered. We will use the vorticity-stream function approach from Chapter 3 and thus we assume the velocity $\widehat{\mathbf{v}}$ to be tangential without loss of generality, see Chapter 3 for details. The force acting on an interfacial fluid surrounded by a bulk fluid is defined by the tangential part of the jump in the bulk stress tensor over the interface $\mathcal{S}$, i.e.

$$\widehat{\mathbf{f}} = \boldsymbol{\pi} \left[\!\left[\boldsymbol{\Sigma} \boldsymbol{\nu} \right]\!\right] \tag{5.3}$$

with the projection operator $\boldsymbol{\pi} = \mathbf{I} - \boldsymbol{\nu} \otimes \boldsymbol{\nu}$, the normal vector $\boldsymbol{\nu}$ and $\left[\!\left[\boldsymbol{\Sigma} \boldsymbol{\nu} \right]\!\right] = (\boldsymbol{\Sigma}_2 \boldsymbol{\nu} - \boldsymbol{\Sigma}_1 \boldsymbol{\nu})|_{\mathcal{S}}$, see [AD09] for details. The bulk stress tensor in Ω_i is defined by $\boldsymbol{\Sigma}_i = -P_i \mathbf{I} + 2\eta_i \mathbf{D}_i$ with the rate-of-strain tensor $\mathbf{D}_i = \frac{1}{2} \left(\nabla \mathbf{V}_i + (\nabla \mathbf{V}_i)^T\right)$.

By using $\boldsymbol{\pi\nu} = 0$ it can be easily shown that the forcing term (5.3) reduces to

$$\widehat{\mathbf{f}} = 2\boldsymbol{\pi} \left[\!\left[\eta\mathbf{D}\boldsymbol{\nu}\right]\!\right] , \tag{5.4}$$

which means that this force is independent of the bulk pressure and only considers velocity gradients. Finally, the complete system of equations in its dimensional form now reads

$$\rho_i \left(\partial_t \mathbf{V}_i + \left(\mathbf{V}_i \cdot \nabla\right) \mathbf{V}_i\right) = -\nabla P_i + \eta_i \boldsymbol{\Delta} \mathbf{V}_i$$

$$\nabla \cdot \mathbf{V}_i = 0$$

$$\mathbf{V}_i|_{\mathcal{S}} = \widehat{\mathbf{v}} \tag{5.5}$$

$$\rho_{\mathcal{S}} \left(\partial_t \widehat{\mathbf{v}} + \boldsymbol{\nabla}_{\widehat{\mathbf{v}}} \widehat{\mathbf{v}}\right) = -\nabla_{\mathcal{S}} p + \eta_{\mathcal{S}} \left(-\boldsymbol{\Delta}^{\mathrm{dR}}\widehat{\mathbf{v}} + 2\kappa\widehat{\mathbf{v}}\right) + 2\boldsymbol{\pi} \left[\!\left[\eta\mathbf{D}\boldsymbol{\nu}\right]\!\right]$$

$$\mathrm{div}_{\mathcal{S}} \, \widehat{\mathbf{v}} = 0 \, ,$$

which has to be equipped with appropriate initial and boundary conditions.

Next, we nondimensionalize the system of equations (5.5) and follow the same notation as in Section 2.5.3. For the bulk pressure we use the scale $\rho_i l^{*2}/t^{*2}$. Thus, the bulk hydrodynamic equations and the boundary conditions of system (5.5) transforms to

$$\frac{\rho_i l^*}{t^{*2}} \left(\widetilde{\partial}_t \widetilde{\mathbf{V}}_i + \left(\widetilde{\mathbf{V}}_i \cdot \widetilde{\nabla}\right) \widetilde{\mathbf{V}}_i\right) = -\frac{\rho_i l^*}{t^{*2}}\widetilde{\nabla}\widetilde{P}_i + \frac{\eta_i}{l^*t^*}\widetilde{\boldsymbol{\Delta}}\widetilde{\mathbf{V}}_i$$

$$\frac{1}{t^*}\widetilde{\nabla} \cdot \widetilde{\mathbf{V}}_i = 0$$

$$\frac{l^*}{t^*}\widetilde{\mathbf{V}}_i|_{\mathcal{S}} = \frac{l^*}{t^*}\widetilde{\widehat{\mathbf{v}}} \, .$$

For the nondimensionalization of the surface hydrodynamic equations in the system (5.5) we use the same ideas as for the system (2.28)-(2.29) with the nondimensional surface force

$$\widetilde{\widehat{\mathbf{f}}} = \frac{t^*}{\rho_{\mathcal{S}}l^*}2\widetilde{\boldsymbol{\pi}} \left[\!\left[\eta\widetilde{\mathbf{D}}\widetilde{\boldsymbol{\nu}}\right]\!\right] = \frac{2}{\mathrm{Re}}\widetilde{\boldsymbol{\pi}} \left[\!\left[\eta^{\star}\widetilde{\mathbf{D}}\widetilde{\boldsymbol{\nu}}\right]\!\right]$$

with the dynamic viscosity ratio $\eta_i^{\star} = \eta_i l^*/\eta_{\mathcal{S}}$. Henceforth, we drop the "$\sim$"-notation and consider each variable, quantity and operator in its nondimensional

form. Further manipulation and using the bulk Reynolds number $\mathrm{Re}_i^{\mathrm{B}} = \frac{\rho_i l^{*2}}{\eta_i t^*}$ finally yields the nondimensional bulk hydrodynamic equations of the system (5.5)

$$\partial_t \mathbf{V}_i + (\mathbf{V}_i \cdot \nabla) \mathbf{V}_i = -\nabla P_i + \frac{1}{\mathrm{Re}_i^{\mathrm{B}}} \mathbf{\Delta} \mathbf{V}_i$$

$$\nabla \cdot \mathbf{V}_i = 0$$

and the nondimensional surface hydrodynamic equations of system (5.5)

$$\partial_t \widehat{\mathbf{v}} + \boldsymbol{\nabla}_{\widehat{\mathbf{v}}} \widehat{\mathbf{v}} = -\nabla_{\mathcal{S}} p + \frac{1}{\mathrm{Re}} \left(-\mathbf{\Delta}^{\mathrm{dR}} \widehat{\mathbf{v}} + 2\kappa \widehat{\mathbf{v}} + 2\boldsymbol{\pi} \, [\![\eta^\star \mathbf{D} \boldsymbol{\nu}]\!] \right)$$

$$\mathrm{div}_{\mathcal{S}} \, \widehat{\mathbf{v}} = 0 \, . \tag{5.6}$$

According to Section 3.1 and [NVW12], we transform equation (5.6) into a vorticity-stream function formulation by using the substitution $\widehat{\mathbf{v}} = \mathrm{Rot}_{\mathcal{S}} \, \psi$, i. e.

$$\partial_t \phi + J(\psi, \phi) = \frac{1}{\mathrm{Re}} \left(\Delta_{\mathcal{S}} \phi + 2 \, \mathrm{div}_{\mathcal{S}} \left(\kappa \nabla_{\mathcal{S}} \psi + \widehat{\mathbf{f}}^\perp \right) \right)$$

$$\phi = \Delta_{\mathcal{S}} \psi \tag{5.7}$$

on $\mathcal{S}$ with the stream function ψ, the vorticity ϕ and $\widehat{\mathbf{f}}^\perp := \boldsymbol{\nu} \times \boldsymbol{\pi} \, [\![\eta^\star \mathbf{D} \boldsymbol{\nu}]\!]$. The formulation (5.7) has been analyzed in detail in Chapter 3 and [NVW12] in the absence of external forces.

Summing up, the sharp interface equations of the complete system in nondimensional form now read

$$\partial_t \mathbf{V}_i + (\mathbf{V}_i \cdot \nabla) \mathbf{V}_i = -\nabla P_i + \frac{1}{\mathrm{Re}_i^{\mathrm{B}}} \mathbf{\Delta} \mathbf{V}_i \qquad \text{in } \Omega_i$$

$$\nabla \cdot \mathbf{V}_i = 0 \qquad \text{in } \Omega_i$$

$$\mathbf{V}_i|_{\mathcal{S}} = \mathrm{Rot}_{\mathcal{S}} \, \psi \qquad \text{on } \mathcal{S} \tag{5.8}$$

$$\partial_t \phi + J(\psi, \phi) = \frac{1}{\mathrm{Re}} \left(\Delta_{\mathcal{S}} \phi + 2 \, \mathrm{div}_{\mathcal{S}} \left(\kappa \nabla_{\mathcal{S}} \psi + \widehat{\mathbf{f}}^\perp \right) \right) \qquad \text{on } \mathcal{S}$$

$$\phi = \Delta_{\mathcal{S}} \psi \qquad \text{on } \mathcal{S}$$

with appropriate initial and boundary conditions. In general, $\mathcal{S}$ is a closed interface, which requires only the specification of standard boundary conditions for the outer velocity $\mathbf{V}_1$. However, in order to reproduce the experiment in
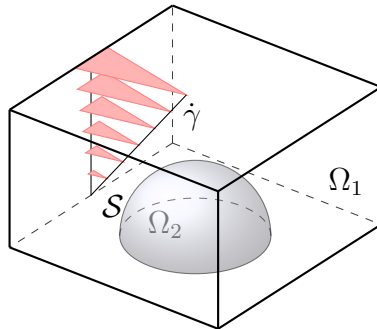
Figure 5.1: *Schematic computational domain Ω_1, Ω_2 and $\mathcal{S}$ to consider the experimental setting in [VMV07, HSWKG13]. The red arrows indicate the shear flow through the domain and $\dot{\gamma}$ denotes the shear rate. At the bottom the vesicle is adhered to a solid wall.*
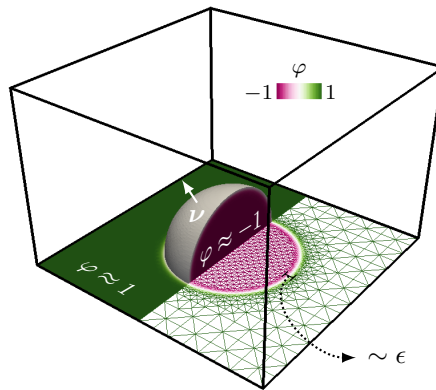
Figure 5.2: *Implicit description of the computational domain $\Omega = \Omega_1 \cup \mathcal{S} \cup \Omega_2$ using a phase field function φ, together with the adaptively refined mesh. Note that the height of the bounding box is not proportional to the rest of the domain due to visual clarity.*

[VMV07, HSWKG13], we need to consider adhesion of the interface to a solid surface, see Figure 5.1. Thus, we specify at the solid surface $\mathbf{V}_1 = \mathbf{V}_2 = \mathbf{0}$, as well as $\psi = 0$ and $\partial_n \psi = 0$.

5.3 Diffuse interface equations

To efficiently solve the coupled bulk/surface problem in equation (5.8), we use the diffuse domain/diffuse interface approximation proposed in [RV06, LLRV09].

We consider a phase field φ, which implicitly describes the interface $\mathcal{S}$ by $\varphi = 0$, the outer bulk domain Ω_1 by $\varphi \approx 1$ and the inner domain Ω_2 by $\varphi \approx -1$, e. g.

$$\varphi(\boldsymbol{x}) = \tanh\left(\frac{1}{\sqrt{2}\epsilon} d(\boldsymbol{x})\right).$$

Thereby, $0 < \epsilon \ll 1$ is a small interface parameter, which defines the width of the diffuse interface, and $d(\boldsymbol{x})$ is a signed distance function describing the minimal distance of $\boldsymbol{x} \in \Omega$ to the interface $\mathcal{S}$ with $\Omega = \Omega_1 \cup \mathcal{S} \cup \Omega_2$, see Figure 5.2. The interface conditions $\mathbf{V}_i|_{\mathcal{S}} = \text{Rot}_{\mathcal{S}}(\psi)$ are incorporated through penalty like forcing terms, cf. [LLRV09]. Thus, the diffuse bulk Navier-Stokes equations read

$$\partial_t \mathbf{V}_i + (\mathbf{V}_i \cdot \nabla) \mathbf{V}_i = -\nabla P_i + \frac{1}{\text{Re}_i^{\text{B}}} \boldsymbol{\Delta} \mathbf{V}_i + \mathbf{F}_i(\mathbf{V}_i, \psi) \qquad \text{in } \Omega$$

$$\nabla \cdot \mathbf{V}_i = 0 \qquad \text{in } \Omega$$

with

$$\mathbf{F}_1(\mathbf{V}_1, \psi) = -\frac{\beta_1}{2}(1 - \varphi)(\mathbf{V}_1 - \text{Rot}_{\mathcal{S}}(\psi))$$

$$\mathbf{F}_2(\mathbf{V}_2, \psi) = -\frac{\beta_2}{2}(1 + \varphi)(\mathbf{V}_2 - \text{Rot}_{\mathcal{S}}(\psi))$$

with typically large penalty parameters β_i. We use in our numerical examples $\beta_i = \frac{10}{\text{Re}_i^{\text{B}}\epsilon^2}$, which was justified asymptotically in [FRGV12]. We further assume that the interface velocity $\hat{\mathbf{v}} = \text{Rot}_{\mathcal{S}}(\psi)$ is defined in the whole domain Ω and has a constant extension normal to the interface $\mathcal{S}$. The vorticity-surface stream function formulation (5.7) is extended to Ω according to the diffuse interface approach proposed in [RV06] and reads

$$B(\varphi)\left(\partial_t \phi + J(\psi, \phi)\right) = \frac{1}{\text{Re}} \nabla \cdot \left(B(\varphi)\left(\nabla \phi + 2\kappa \nabla \psi + 2\widehat{\mathbf{f}}^{\perp}\right)\right)$$

$$B(\varphi)\phi = \nabla \cdot (B(\varphi)\nabla\psi)$$

in Ω where $B(\varphi) \sim (\varphi^2 - 1)^2$ defines an approximation of an interface delta function, which restricts the solution to the surface $\mathcal{S}$. Note that in this formulation all geometric quantities have to be extended to Ω, which can be achieved

by constant normal extension off the surface $\mathcal{S}$. The two bulk velocities $\mathbf{V}_1$ and $\mathbf{V}_2$ allow to compute the jump in the stress tensor in the forcing term $\widehat{\mathbf{f}}^{\perp}$ according to equation (5.4), which again is extended constantly in normal direction off the surface $\mathcal{S}$.

The combination of these equations defines a diffuse domain/diffuse interface approximation of the sharp interface equations (5.8), which can be justified by matched asymptotic expansions, see [TLL^{+}09]. The coupled system reads

$$\partial_t \mathbf{V}_i + (\mathbf{V}_i \cdot \nabla) \mathbf{V}_i = -\nabla P_i + \frac{1}{\mathrm{Re}_i^{\mathrm{B}}} \boldsymbol{\Delta} \mathbf{V}_i + \mathbf{F}_i(\mathbf{V}_i, \psi)$$

$$\nabla \cdot \mathbf{V}_i = 0$$

$$B(\varphi)\left(\partial_t \phi + J(\psi, \phi)\right) = \frac{1}{\mathrm{Re}} \nabla \cdot \left(B(\varphi)\left(\nabla \phi + 2\kappa \nabla \psi + 2\widehat{\mathbf{f}}^{\perp}\right)\right)$$

$$B(\varphi)\phi = \nabla \cdot (B(\varphi)\nabla \psi)$$

(5.9)

in Ω and combines three Navier-Stokes equations, two in the bulk phases and one in the vorticity-stream function formulation on the interface. Again, system (5.9) has to be supplemented by appropriate initial and boundary conditions. At the solid surface we specify again $\mathbf{V}_1 = \mathbf{V}_2 = \mathbf{0}$ as well as $\psi = 0$ and $\partial_n \psi = 0$.

5.4 Numerical approach

To solve the system (5.9) we use a finite element approach. An operator splitting technique is applied to solve both bulk Navier-Stokes systems and the surface flow problem separately. We also use a semi-implicit Euler time stepping scheme. Thus, let the time interval $(0, t_{\mathrm{end}}]$ with end time t_{end} be divided into a sequence of discrete times $0 < t_0 < t_1 < ...$ with time step width $\tau^m = t_m - t_{m-1}$, where the subscript denotes the timestep number. We define the discrete time derivative $\mathrm{d}_\tau v^m := \frac{1}{\tau^m}\left(v^m - v^{m-1}\right)$ for an arbitrary time dependent function v. Thereby, v^m corresponds to the respective function at time $t = t_m$, i.e. $v^m := v(\cdot, t_m)$. Let $\mathcal{T}$ be a conforming triangulation of mesh size h_{M} such that

$$\Omega_h = \bigcup_{T \in \mathcal{T}} T$$

is an interpolation of Ω. The finite element spaces read

$$V_h = \left\{ v \in \mathcal{C}^0(\bar{\Omega}) \mid v_{|T} \in \mathbb{P}^2(T) \; \forall T \in \mathcal{T}, \; v_{|\partial\Omega} = 0 \right\}$$
$$M_h = \left\{ q \in L^2(\Omega) \mid q_{|T} \in \mathbb{P}^1(T) \; \forall T \in \mathcal{T} \right\}$$
$$Y_h = \left\{ \eta \in \mathcal{C}^0(\bar{\Omega}) \mid \eta_{|T} \in \mathbb{P}^1(T) \; \forall T \in \mathcal{T} \right\}$$

with $\mathcal{C}^k(\bar{\Omega})$ the space of k-times continuously differentiable functions on $\bar{\Omega}$, $\mathbb{P}^r(T)$ the set of polynomial functions of degree r on $T \in \mathcal{T}$ and $L^2(\Omega)$ the space of square-integrable functions on Ω. Moreover, the standard L^2 scalar product is denoted by $(\cdot, \cdot)$. Thus, the finite element approximation of the coupled system of equations (5.9) now reads: Find $\mathbf{V}_i^m \in V_h^3, P_i^m \in M_h$ such that $\forall \mathbf{U}_i \in V_h^3, \forall Q_i \in M_h$

$$\left(\mathrm{d}_\tau \mathbf{V}_i^m + (\mathbf{V}_i^{m-1} \cdot \nabla)\mathbf{V}_i^m \,,\; \mathbf{U}_i \right) = \left(P_i^m \,,\; \nabla \cdot \mathbf{U}_i \right) - \frac{1}{\mathrm{Re}_i^{\mathrm{B}}} \left(\nabla \mathbf{V}_i^m \,,\; \nabla \mathbf{U}_i \right)$$
$$+ \left(\mathbf{F}_i(\mathbf{V}_i^m, \psi_h^{m-1}) \,,\; \mathbf{U}_i \right)$$
$$\left(\nabla \cdot \mathbf{V}_i^m \,,\; Q_i \right) = 0$$

and find $\phi^m, \psi^m \in Y_h$ such that $\forall \eta, \xi \in Y_h$

$$\left(B(\varphi)\left(\mathrm{d}_\tau \phi^m + J\left(\psi^{m-1}, \phi^m\right)\right) \,,\; \eta \right) = -\frac{1}{\mathrm{Re}} \left(B(\varphi)\left(\nabla \phi^m + 2\kappa \nabla \psi^m\right) \,,\; \nabla \eta \right)$$
$$- \frac{2}{\mathrm{Re}} \left(B(\varphi)\widehat{\mathbf{f}}^{\perp,m} \,,\; \nabla \eta \right)$$
$$-\left(B(\varphi)\nabla \psi^m \,,\; \nabla \xi \right) = \left(B(\varphi)\phi^m \,,\; \xi \right)$$

with $\widehat{\mathbf{f}}^{\perp,m} = \boldsymbol{\nu} \times \boldsymbol{\pi} \, [\![\eta^\star \mathbf{D}^m \boldsymbol{\nu}]\!]$. In order to ensure the solvability of the resulting linear system, we replace $B(\varphi)$ by $\max(B(\varphi), \delta)$ in the second order terms with a small regularization parameter $0 < \delta \ll 1$, see [RV06]. In the following numerical examples we specify $\delta = 10^{-7}$. A general discussion of the numerical treatment of the boundary conditions for the stream function ψ and the vorticity ϕ at the solid surface is given in [EL96]. We consider an approach of [Cal02], which has already been adapted to the diffuse domain/diffuse interface approximation and validated in [PGRPV17]. Here, we explicitly specify $\partial_n \psi = 0$ and $\partial_n \phi = 0$

on the solid surface and treat the Dirichlet condition $\psi = 0$ implicitly using a penalty approach.

The following simulations have been computed using the finite element toolbox AMDiS [VV07, WLPV15] with an adaptively refined mesh, with a high resolution along the diffuse interface, with mesh size $h_M \approx 3\sqrt{2}\epsilon/5$. This leads to approximately 7 to 8 points along the normal direction across the diffuse interface. We use Taylor-Hood finite elements for both Navier-Stokes equations, i. e. quadratic finite elements for the velocity components and linear finite elements for the pressure variable. For the surface stream function formulation linear finite elements are employed. A domain decomposition approach enables to perform simulations with a large number of degrees of freedom with an acceptable cost. A parallel iterative solver BiCGStab(l) with $l = 2$ and a Jacobi preconditioner is used in order to solve the resulting linear systems.

5.5 Simulation results

5.5.1 Experimental validation

In [HSWKG13] the experimental setup of [VMV07] was used to determine membrane viscosity. Two types of vesicles – liquid ordered (L_o) and liquid disordered (L_d) – are adhered to a solid surface and are considered under shear flow. Here, we use the same setup in order to compare the experimental data as well as their simulation data and the results of our approach. We use the length scale $l^* = 20\mu$m and the time scale $t^* = \frac{1}{5.2}$s. The computational domain $\Omega = [-2, 2]^2 \times [0, 4]$ is used and a hemispherical geometry for the vesicle with radius $R = 1$ is located at the origin. Thus, the signed distance function used to define φ is $d(\boldsymbol{x}) = |\boldsymbol{x}| - R$. We consider a shear flow boundary condition with shear rate $\dot{\gamma} = \frac{1}{2}$ on top of Ω and no slip boundary conditions on the solid surface at the bottom. On all other boundaries we employ homogeneous Neumann conditions, which can be justified by the relatively large spatial extension of the domain compared to the vesicle size. Table 5.1 concludes the used material and nondimensional parameters. We start with zero initial condition and let the flow evolve until a steady state is reached.

Parameter	L_o	L_d
$\eta_{\mathcal{S}}$	$17.47 \cdot 10^{-9} \frac{\text{kg}}{\text{s}}$	$9.56 \cdot 10^{-9} \frac{\text{kg}}{\text{s}}$
$\rho_{\mathcal{S}}$	$20 \cdot 10^{-3} \frac{\text{kg}}{\text{m}^2}$	
η_1, η_2	$10^{-3} \frac{\text{kg}}{\text{ms}}$	
ρ_1, ρ_2	$10^3 \frac{\text{kg}}{\text{m}^3}$	
$\eta_1^\star, \eta_2^\star$	1.14	2.09
Re	$2.38 \cdot 10^{-3}$	$4.35 \cdot 10^{-3}$
$\text{Re}_1^{\text{B}}, \text{Re}_2^{\text{B}}$	$2.08 \cdot 10^{-3}$	

Table 5.1: *Material parameters for the experimental setup proposed in [HSWKG13] and nondimensional parameters used for simulation. The length scale l^* is set to $20 \cdot 10^{-6}$m and the timescale t^* is $\frac{1}{5.2}$s.*

shear flow direction
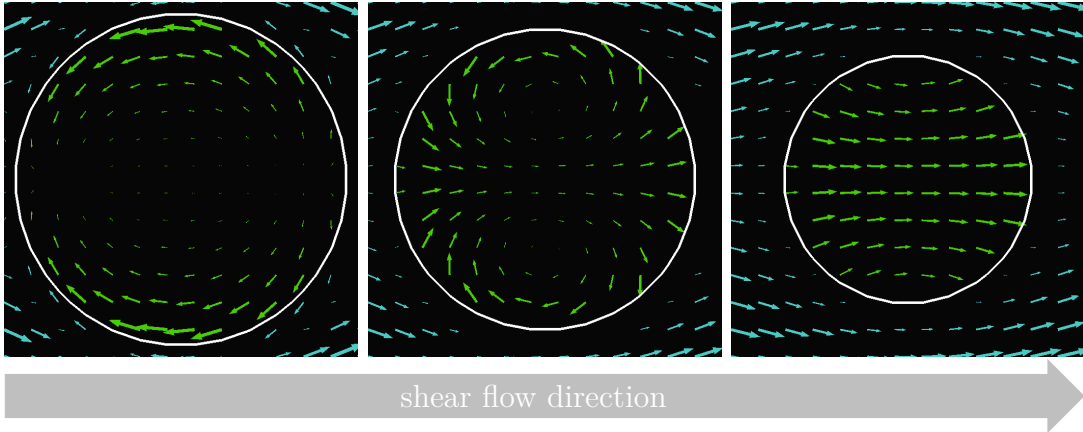
Figure 5.3: *Two dimensional velocity (projected to the plane and rescaled for visualization) of the sliced L_d vesicle at height levels $z = 0.3, 0.5, 0.7$ (from left to right) for $\epsilon = 0.01$. The green arrows indicate the inner velocity $\mathbf{V}_2$ and the blue arrows indicate the outer velocity $\mathbf{V}_1$. Shear direction is from left to right.*

Figure 5.3 shows the inner velocity $\mathbf{V}_2$ on plane cuts at different height levels through the vesicle. In Figure 5.4 (left) a visualization based on streamlines of the inner velocity $\mathbf{V}_2$ is shown and in Figure 5.4 (right) the flow field of the fluid interface is visualized. All these results qualitatively coincide with the experimental as well as the simulation data in [HSWKG13].

In order to compare the results quantitatively, we use the velocity profile through
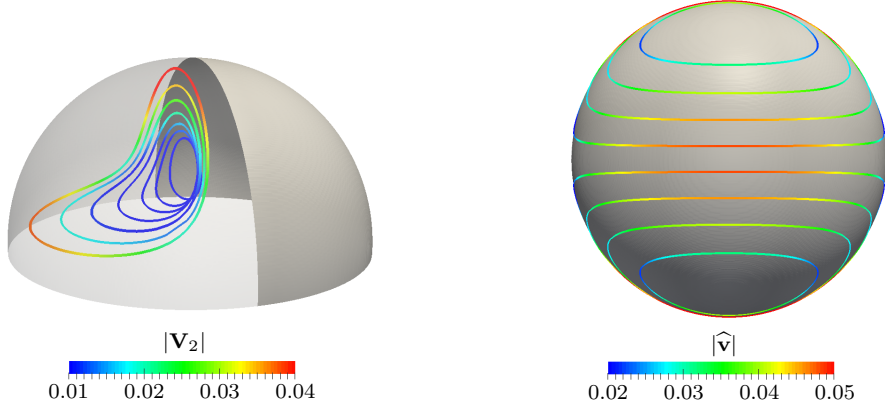
Figure 5.4: Streamlines of the inner velocity $\mathbf{V}_2$ (left) and streamlines of the surface fluid viewed from top (right) for $\epsilon = 0.01$.
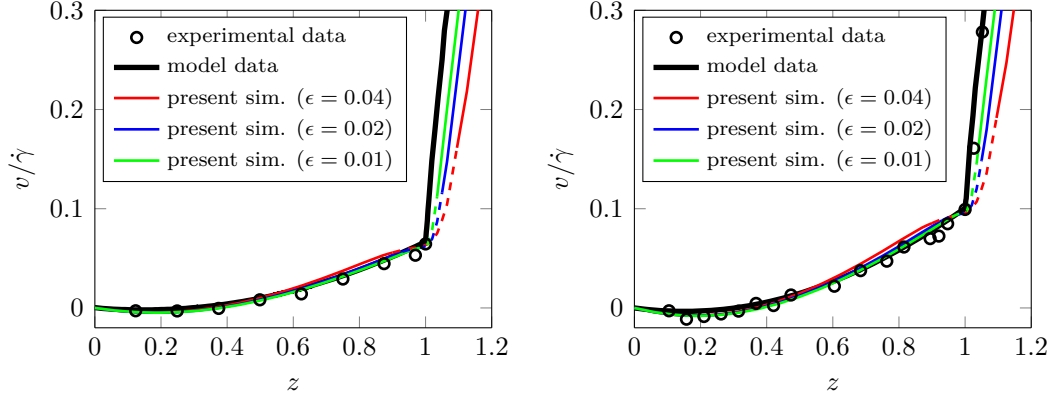
Figure 5.5: Quantitative comparison of experimental as well as model data reported in [HSWKG13] and the simulation of the present model for different values of ϵ and both vesicle types L_o (left) and L_d (right). Thereby, v denotes the component of the velocity field parallel to the shear flow. The dashed part of each colored lines indicates the interface region for the respective simulation. We here considered the interpolated velocity $\mathbf{V} = \frac{1}{2} ((1 + \varphi)\mathbf{V}_1 + (1 - \varphi)\mathbf{V}_2)$. The experimental as well as the model data (black lines and black circles, respectively) are extracted from [HSWKG13].

the vesicle apex, see Figure 5.5. The experimental as well as the model data, which is obtained using a Stokes approximation, (black lines and black circles, respectively) are extracted from [HSWKG13]. The numerical convergence of our phase field approach to the experimental data for $\epsilon \to 0$ can be observed. The velocity profile inside the vesicle, as well as the slope discontinuity at the membrane are nicely resolved. Table 5.2 shows the experimental order of con-

ϵ	$\|\mathbf{V} - \widehat{\mathbf{v}}\|_{2,\mathcal{S}}$	EOC	L_o $\|\mathbf{V}_1 - \mathbf{V}_2\|_{2,\mathcal{S}}$	EOC	$\|\mathbf{V} - \widehat{\mathbf{v}}\|_{2,\mathcal{S}}$	EOC	L_d $\|\mathbf{V}_1 - \mathbf{V}_2\|_{2,\mathcal{S}}$	EOC
0.10	0.0142	–	0.0145	–	0.0142	–	0.0145	–
0.09	0.0123	1.30	0.0126	1.30	0.0124	1.30	0.0127	1.29
0.08	0.0112	0.82	0.0115	0.84	0.0112	0.82	0.0115	0.83
0.07	0.0101	0.77	0.0103	0.78	0.0101	0.77	0.0103	0.78
0.06	0.0089	0.82	0.0091	0.83	0.0089	0.82	0.0091	0.83
0.05	0.0078	0.70	0.0080	0.71	0.0079	0.69	0.0080	0.70
0.04	0.0063	1.01	0.0064	1.02	0.0063	1.01	0.0064	1.01
0.03	0.0049	0.83	0.0050	0.84	0.0050	0.82	0.0050	0.83
0.02	0.0033	1.01	0.0033	1.01	0.0033	1.01	0.0034	1.00
0.01	0.0016	1.00	0.0017	0.99	0.0017	0.99	0.0017	0.97

Table 5.2: Experimental order of convergence (EOC) for both the L_o and the L_d vesicle and different errors $\|\mathbf{V} - \widehat{\mathbf{v}}\|_{2,\mathcal{S}}$ and $\|\mathbf{V}_1 - \mathbf{V}_2\|_{2,\mathcal{S}}$. Thereby, $\|\cdot\|_{2,\mathcal{S}}$ denotes the L^2 norm over the interface $\mathcal{S}$.

vergence (EOC) for different errors and both vesicle types L_o and L_d. We use the errors in the L^2 norm $\|\mathbf{V} - \widehat{\mathbf{v}}\|_{2,\mathcal{S}}$ and $\|\mathbf{V}_1 - \mathbf{V}_2\|_{2,\mathcal{S}}$ on the interface $\mathcal{S}$ to get a measure for the approximation of the boundary conditions at the interface. In all cases a linear convergence rate is observed.

5.5.2 Ellipsoidal shaped vesicle

Since our approach is not limited to a hemispherical shape we consider an ellipsoidal shape for the vesicle. The ellipsoid is represented by the levelset function $q(\boldsymbol{x}) = (x/a)^2 + (y/b)^2 + (z/c)^2$, with $\boldsymbol{x} = (x, y, z)^T \in \mathbb{R}^3$. The function $q(\boldsymbol{x})$ can be transformed into a signed distance function $d(\boldsymbol{x})$ using, e. g., the methods proposed in [SVV05, BR06]. In the following simulations we use the coefficients $a = 0.8$, $b = 1.2$ and $c = 0.9$ and rotate the ellipsoid around the z-axis (height axis) by an angle of $\pi/5$ to break the symmetry. As for the hemispherical vesicle, also the ellipsoid is in equilibrium if the volume $|\Omega_2|$ is conserved, the contact angle with the solid bottom is π and the membrane is inextensible. Hence, also for this configuration our assumption of a stationary profile is fulfilled. All other parameters remain unchanged and we consider the L_d vesicle.

We visualized the inner flow field in Figure 5.6 (top row) in form of plane cuts at different height levels through the vesicle. In contrast to a hemisphere
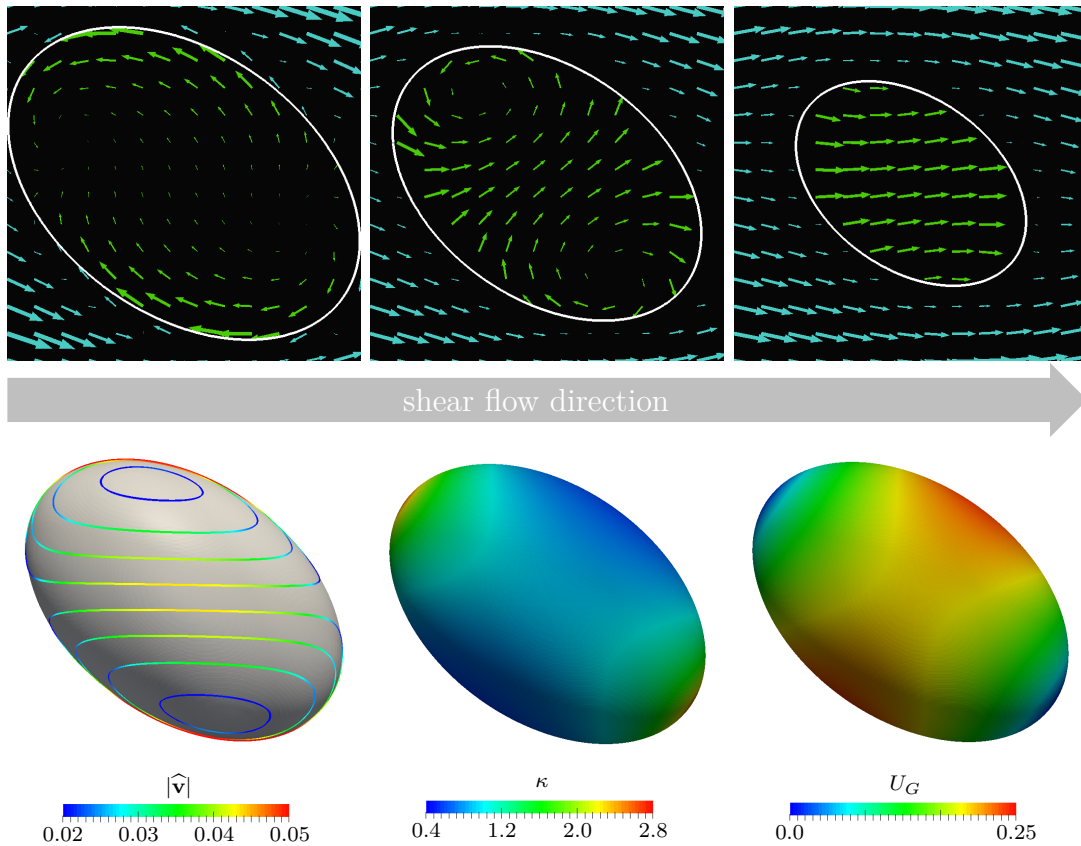
Figure 5.6: Top row: Two dimensional velocity (projected to the plane and rescaled for visualization) for the sliced ellipsoidal vesicle at levels $z = 0.3, 0.5, 0.7$ (from left to right) for $\epsilon = 0.01$. The green arrows indicate the inner velocity $\mathbf{V}_2$ and the blue arrows indicate the outer velocity $\mathbf{V}_1$. Bottom row: Streamlines of the surface fluid (left), Gaussian curvature κ (center) and the geometric potential U_G (right) viewed from top for the ellipsoid and $\epsilon = 0.01$. Shear direction is from left to right.

as used in the prior section the ellipsoidal shape has a non-constant Gaussian curvature κ (see Figure 5.6) and therefore a direct influence on the surface flow field. The influence of the geometry on the flow field can be analyzed by an effective geometric interaction which depends linearly on the geometric potential U_G defined by the surface Laplace equation $\Delta_{\mathcal{S}} U_G = \kappa$, see Chapter 3 and [TVN10, RV15, RV18a] for details. Due to this interaction, vortices in a flow field are typically attracted to peaks and valleys, i.e local maxima of the Gaussian curvature. The steady state interfacial flow field is shown in Figure 5.6 (bottom row, left) in form of the surface streamlines. The two vortices are

Ellipsoid	a	b	c
1	0.990	1.0	0.9
2	0.892	1.1	0.9
3	0.800	1.2	0.9
4	0.712	1.3	0.9
5	0.627	1.4	0.9
6	0.544	1.5	0.9
7	0.464	1.6	0.9
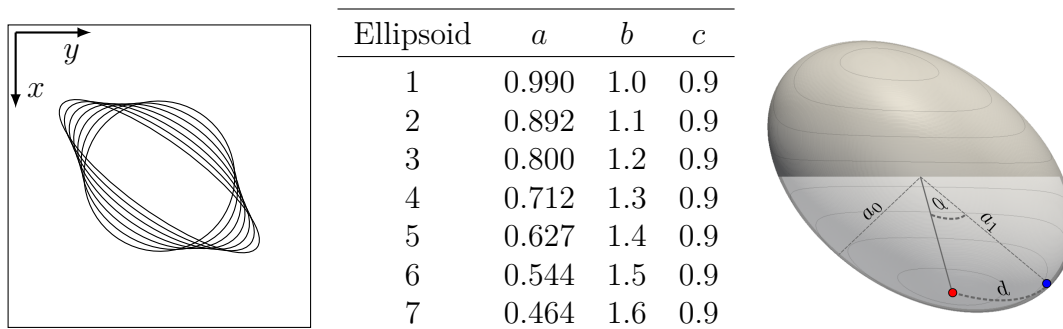
Figure 5.7: Left: Considered ellipsoidal shapes visualized as contour lines of the phase field function in the bottom plane. Middle: Table with axes parameters for the considered ellipsoids. Right: Ellipsoidal surface with surface streamlines, the center of one vortex (red dot) and highest curvature point (blue dot), the major and minor axis of the projected ellipsoid, and the measured values d and α.

shifted towards the regions of high Gaussian curvature κ, see Figure 5.6 (bottom row, center and right) which shows the Gaussian curvature κ and the geometric potential U_G for the ellipsoidal shaped vesicle. However, already the specified no-slip boundary condition on the substrate prohibit the vortices to be located at the points of highest Gaussian curvature. Furthermore, the surface flow field is influenced by the bulk flow. Thus, if this shift in the location of the vortices is a result of the geometric potential or has its origin in the bulk flow or the specified boundary conditions remains open. To identify the effect we vary the geometry. Thereby, we keep the height of the ellipsoid $c = 0.9$ constant to have a comparable interaction with the bulk flow. Furthermore, we fix the area of the ellipsoid, to maintain comparable surface flow properties. We only vary a and b, see Figure 5.7 (left, middle). Figure 5.7 (right) shows the setting, with the red dot being the center of one vortex and the blue dot being the point of highest curvature on the major axis. We measure the geodesic distance d between both points and the angle α. Both values should decrease with increasing curvature effect. In Figure 5.8 the values of α and d are plotted for the different geometries in comparison with the results obtained without the Gaussian curvature term in the incompressible surface Navier-Stokes equation. Both values decrease for more elongated ellipsoids and also the difference between the results with the correct κ and with $\kappa = 0$ increases, which indicates the geometric contribution.
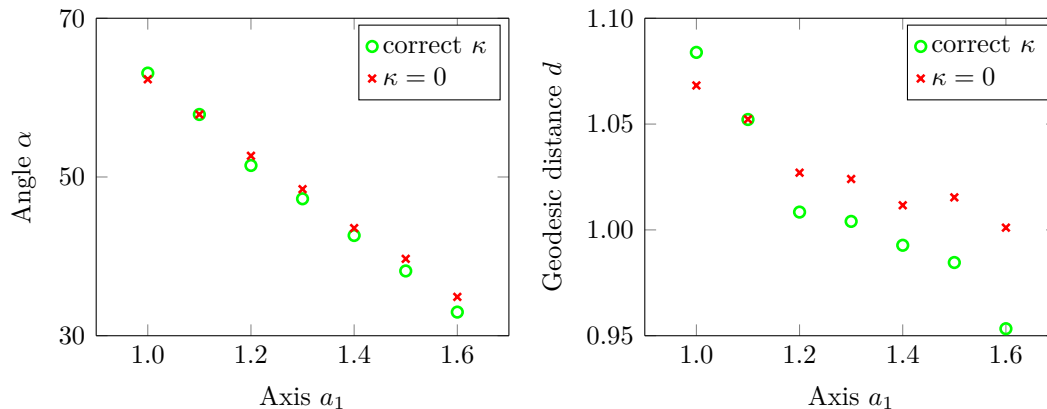
Figure 5.8: The angle α (left) and geodesic distance d (right) as a function of the major axis of the ellipsoid. In addition the results for $\kappa = 0$ in the surface Navier-Stokes equation are shown for comparison for the same geometries.

5.6 Conclusion

We have introduced a model for a stationary fluidic interface in a viscous fluid. The interfacial hydrodynamics are described by the incompressible surface Navier-Stokes equation, for which we used the surface vorticity-stream function approach introduced in Chapter 3. The basic ideas of [RV06] and [LLRV09] are used to transform the model in a description with phase fields. We have validated the results of the model on the experimental as well as model data provided in [HSWKG13] and have shown the numerical convergence of our approach for the interface parameter $\epsilon \to 0$. Additionally, we have presented numerical examples for interfaces with non-constant Gaussian curvature κ and the interaction with the underlying geometry. The numerical approach is reliant on the inextensibility of the membrane. Without this constraint, simpler models can be built which consider the membrane fluidity implicitly using a Boussinesq-Scriven interface stress tensor, see e. g. [SPJVH11, RZ13, BGN15b, GBJL16]. The resulting interfacial flow patterns in these models, which consider droplets instead of vesicles or cells, are qualitatively different and lead to toroidal circulation [DV87].

6 | Polar liquid crystals on evolving surfaces

In this chapter, we consider the flow of polar liquid crystals whose molecular orientation is subjected to a tangential anchoring on an evolving curved surface. The underlying model is a simplified surface Ericksen-Leslie model, which has been derived as a thin-film limit of the corresponding three-dimensional equations, recently. We propose the numerical approach, which is based on the Cartesian extension of the corresponding equations, an operator splitting approach and a finite element discretization in space. We study the strong interplay between hydrodynamics and topology, geometric properties and defect dynamics in various numerical examples.

The main content of this chapter is taken from the author's publication [NRV18].

Contents

6.1 Overview

Liquid crystals (LCs) are partially ordered materials that combine the fluidity of liquids with the orientational order of crystalline solids [dGP93, CL95]. Topological defects are a key feature of LCs if considered under external constraints. In particular, on curved surfaces these defects are important and have been intensively studied on a sphere [DSL00, BSZ10, SBX08, DSOdlC12, KLLFNV13, NV12] and under more complicated constraints [Sta01, PvdS03, MRL⁺14]. LCs on curved surfaces can be realized on various levels. One possibility is to prepare a double emulsion of two concentric droplets [FNVU⁺07] for which the intervening shell is filled with molecular or colloidal LCs, which show a planar anchoring at the two curved interfaces [LLFNNB12, LNZ⁺13, LSRL11]. Also experiments with air bubbles covered by microrods have been prepared and studied [ZCLS08]. Moreover, topological defects for charged colloidal spheres confined on a sphere were experimentally investigated [GKHC18]. Ellipsoidal colloids bound to curved fluid-fluid interfaces with negative Gaussian curvature [LSMS18] and spherical droplets covered with aspherical surfactants [YWSG18] were explored. Even living and motile "particles" like cells [BKAS17] and suspensions of microtubules and kinesin [KLS⁺14, EPC⁺18] were recently studied on surfaces of different curvatures. In all these studies a tight coupling between topology, geometric properties and defect dynamics is observed. In equilibrium, defects are positioned according to geometric properties of the surface [LP92, Nel02, KRV11]. Creation and annihilation of defects can result from geometric interaction, leading to different realizations of the Poincaré-Hopf theorem (2.18) on topologically equivalent but geometrically different surfaces [NNPV18].

Most theoretical studies of these phenomena use particle methods. Despite the interest in such methods, a continuous description would be more essential for predicting and understanding the macroscopic relation between type and position of the defects and geometric properties of the surface. Also the influence of hydrodynamics and dynamic shape changes on these relations would be much more appropriate to study within a continuous approach. However, a coherent model, which accounts for the complex interplay between topology, geometry, defect interactions and hydrodynamics, is still lacking. Here, we propose a min-

imal continuous surface hydrodynamic LC model, which contains the evolution of the surface, tangential polar ordering and surface hydrodynamics. Recently, this model has been derived as a thin-film limit of the simplified Ericksen-Leslie model [LL00] in [NRV18]. We describe a numerical approach to solve this model on general surfaces and demonstrate by simulations various expected and some unexpected phenomena on ellipsoidal and toroidal surfaces. These phenomena result from the tight coupling of the geometry with the velocity and the director field. However, a full exploration of the rich nonlinear phenomena resulting from this relation goes beyond the scope of this chapter. Here, we only highlight the importance of the newly introduced geometric coupling terms in the equations.

6.2 Surface Ericksen-Leslie model

The Ericksen-Leslie model [Eri61, Eri76, Les68] is an established model for LCs, whose relaxation dynamics are affected by hydrodynamics. In [LL00] a simplified model was introduced and analyzed. This system already retains the main properties of the original Ericksen-Leslie model [LLW10, HW13, WZZ13, HLW14] and is considered as a starting model to derive a surface hydrodynamic LC model by means of a thin-film limit. Here, we briefly sketch the basic ideas of the limiting process. For more details we refer to [NRV18]. We recall the general notation from Chapter 2, i.e., let $\mathcal{S}(t) \subset \mathbb{R}^3$ be a regular moving oriented compact smooth Riemannian surface without boundaries and let $\Omega_h(t) \subset \mathbb{R}^3$ be the corresponding neighborhood, which is called thin film from now on. The thickness of the thin film is denoted by h and considered to be sufficiently small. Again, the normal velocity of the surface $v_{\boldsymbol{\nu}}$ is considered to be prescribed. However, the simplified Ericksen-Leslie model [LL00] in the thin film Ω_h reads

$$\rho\left(\partial_t \mathbf{V} + (\mathbf{U} \cdot \nabla)\,\mathbf{V}\right) = -\nabla P + \eta \boldsymbol{\Delta} \mathbf{V} - \lambda \nabla \cdot \boldsymbol{\sigma}^{\mathrm{E}} \tag{6.1}$$

$$\nabla \cdot \mathbf{V} = 0 \tag{6.2}$$

$$\partial_t \boldsymbol{P} + (\mathbf{U} \cdot \nabla)\,\boldsymbol{P} = \eta_p \boldsymbol{\Delta} \boldsymbol{P} - \omega_n \left(\|\boldsymbol{P}\|_{\Omega_h}^2 - 1\right) \boldsymbol{P}\,. \tag{6.3}$$

Here, $\mathbf{V}$ denotes the fluid velocity, $\mathbf{U} = \mathbf{V} - \mathbf{W}$ the relative fluid velocity (relative to the observer velocity, which is denoted by $\mathbf{W}$, see [NRV18]), $\boldsymbol{P}$ the

director field, P the pressure, $\boldsymbol{\sigma}^{\mathrm{E}} = (\nabla \boldsymbol{P})^T \nabla \boldsymbol{P}$ the Ericksen stress tensor, ρ the fluid density, η the dynamic viscosity, λ the competition between kinetic energy and elastic potential energy, η_p the elastic relaxation time for the molecular orientation field and ω_n a penalty parameter to enforce $\|\boldsymbol{P}\| = 1$ weakly.

Next, we use the same notation as in Section 2.5.3 and nondimensionalize equations (6.1), (6.2) and (6.3). Hence, we consider the nondimensional parameters $\widetilde{\lambda} := \lambda \frac{t^{*2}}{\rho l^{*4}}$, $\widetilde{\eta}_p := \eta_p \frac{t^*}{l^{*2}}$ and $\widetilde{\omega}_n := \omega_n t^*$ as well as $\widetilde{\boldsymbol{\sigma}}^{\mathrm{E}} := l^{*2} \boldsymbol{\sigma}^{\mathrm{E}}$ and $\boldsymbol{P} = \widetilde{\boldsymbol{P}}$. Thus, the nondimensional form of equations (6.1), (6.2) and (6.3) reads

$$\widetilde{\partial}_t \widetilde{\mathbf{V}} + \left(\widetilde{\mathbf{U}} \cdot \widetilde{\nabla} \right) \widetilde{\mathbf{V}} = -\widetilde{\nabla} \widetilde{P} + \frac{\eta t^*}{\rho l^{*2}} \widetilde{\boldsymbol{\Delta}} \widetilde{\mathbf{V}} - \widetilde{\lambda} \widetilde{\nabla} \cdot \widetilde{\boldsymbol{\sigma}}^{\mathrm{E}}$$

$$\widetilde{\nabla} \cdot \widetilde{\mathbf{V}} = 0$$

$$\widetilde{\partial}_t \widetilde{\boldsymbol{P}} + \left(\widetilde{\mathbf{U}} \cdot \widetilde{\nabla} \right) \widetilde{\boldsymbol{P}} = \widetilde{\eta}_p \widetilde{\boldsymbol{\Delta}} \widetilde{\boldsymbol{P}} - \widetilde{\omega}_n \left(\left\| \widetilde{\boldsymbol{P}} \right\|_{\Omega_h}^2 - 1 \right) \widetilde{\boldsymbol{P}}.$$

Finally, by dropping the "$\sim$"-notation for better readability and using the Reynolds number $\mathrm{Re} = \frac{\rho l^{*2}}{\eta t^*}$ the nondimensional version of equations (6.1), (6.2) and (6.3) reads

$$\partial_t \mathbf{V} + (\mathbf{U} \cdot \nabla) \mathbf{V} = -\nabla P + \frac{1}{\mathrm{Re}} \boldsymbol{\Delta} \mathbf{V} - \lambda \nabla \cdot \boldsymbol{\sigma}^{\mathrm{E}} \tag{6.4}$$

$$\nabla \cdot \mathbf{V} = 0 \tag{6.5}$$

$$\partial_t \boldsymbol{P} + (\mathbf{U} \cdot \nabla) \boldsymbol{P} = \eta_p \boldsymbol{\Delta} \boldsymbol{P} - \omega_n \left(\|\boldsymbol{P}\|_{\Omega_h}^2 - 1 \right) \boldsymbol{P}. \tag{6.6}$$

Henceforth, we consider each variable, geometric quantity and parameter in its nondimensional form.

The system has to be equipped with appropriate initial conditions for the velocity, i. e. $\mathbf{V}(\cdot, t)|_{t=0} = \mathbf{V}_0(\cdot)$, and for the director field, i. e. $\boldsymbol{P}(\cdot, t)|_{t=0} = \boldsymbol{P}_0(\cdot)$. The boundary conditions are specified as follows. For the director field we use a homogeneous Dirichlet condition for the normal component and a homogeneous Neumann condition for the tangential components, i. e.

$$\boldsymbol{\nu} \cdot \boldsymbol{P} = 0 \tag{6.7}$$

$$\boldsymbol{\nu} \cdot \nabla \left(\boldsymbol{\pi}_{\partial \Omega_h} \boldsymbol{P} \right)_i = 0 \tag{6.8}$$

on $\partial\Omega_h$, where $\boldsymbol{\pi}_{\partial\Omega_h}$ denotes the orthogonal projection into the boundary tangential space and $\boldsymbol{\nu}$ the surface normal vector, which is considered to be extended to the thin film Ω_h, cf. Chapter 2 for details. For the velocity we specify a homogeneous Navier boundary condition for the tangential components, i.e.

$$\boldsymbol{\pi}_{\partial\Omega_h}\left[\left(\nabla\mathbf{V} + (\nabla\mathbf{V})^T\right)\boldsymbol{\nu}\right] = 0 \tag{6.9}$$

on $\partial\Omega_h$. The boundary condition for the normal component of the velocity is fixed by the Dirichlet condition $\boldsymbol{\nu}\cdot\mathbf{V} = v_{\boldsymbol{\nu}}$ on $\partial\Omega_h$. However, the thin film limit $h\to 0$ is achieved by Taylor expansions in orders of the thin film thickness h of the equations (6.4), (6.5) as well as (6.6) and evaluating at the surface. By applying this rigorous technique and using the boundary conditions (6.7), (6.8), (6.9) as well as $h\to 0$ we obtain simplified surface Ericksen-Leslie model

$$\boldsymbol{\pi}\partial_t\mathbf{v} + \boldsymbol{\nabla}_{\mathbf{v}}\mathbf{v} - v_{\boldsymbol{\nu}}\mathcal{B}\mathbf{v} - v_{\boldsymbol{\nu}}\nabla_{\mathcal{S}}v_{\boldsymbol{\nu}} = -\nabla_{\mathcal{S}}p + \frac{1}{\mathrm{Re}}\left(-\boldsymbol{\Delta}^{\mathrm{dR}}\mathbf{v} + 2\kappa\mathbf{v} + \nabla_{\mathcal{S}}\left(v_{\boldsymbol{\nu}}\mathcal{H}\right)\right)$$
$$- \frac{2}{\mathrm{Re}}\operatorname{div}_{\mathcal{S}}\left(v_{\boldsymbol{\nu}}\mathcal{B}\right) - \lambda\operatorname{div}_{\mathcal{S}}\boldsymbol{\sigma}_{\mathcal{S}}^{\mathrm{E}} \tag{6.10}$$
$$\operatorname{div}_{\mathcal{S}}\mathbf{v} = v_{\boldsymbol{\nu}}\mathcal{H} \tag{6.11}$$
$$\boldsymbol{\pi}\partial_t\mathbf{p} + \boldsymbol{\nabla}_{\mathbf{v}}\mathbf{p} = \eta_p\left(\boldsymbol{\Delta}^{\mathrm{B}}\mathbf{p} - \mathcal{B}^2\mathbf{p}\right) - \omega_n\left(\|\mathbf{p}\|_{\mathcal{S}}^2 - 1\right)\mathbf{p}\,. \tag{6.12}$$

Thereby, $\boldsymbol{\sigma}_{\mathcal{S}}^{\mathrm{E}} = (\nabla_{\mathcal{S}}\mathbf{p})^T\nabla_{\mathcal{S}}\mathbf{p} + (\mathcal{B}\mathbf{p})\otimes(\mathcal{B}\mathbf{p})$ is called the extrinsic surface Ericksen stress tensor. The detailed limiting process from above can be found in [NRV18]. Thereby, it is noted that equations (6.10) and (6.11) coincide with equations (2.28) and (2.29) from Chapter 2 with $\mathbf{f} = -\lambda\operatorname{div}_{\mathcal{S}}\boldsymbol{\sigma}_{\mathcal{S}}^{\mathrm{E}}$. Again, the system of equations (6.10), (6.11) and (6.12) has to be equipped with appropriate initial conditions for the velocity, i.e. $\mathbf{v}\left(\cdot,t\right)|_{t=0} = \mathbf{v}_0(\cdot)$, and for the director field, i.e. $\mathbf{p}\left(\cdot,t\right)|_{t=0} = \mathbf{p}_0(\cdot)$. The system combines the incompressible surface Navier-Stokes equation from Section 2.5 with a weak surface Frank-Oseen model [NNPV18] on an evolving surface. Eq. (6.12) with $\mathbf{v} = \mathbf{0}$, $v_{\boldsymbol{\nu}} = 0$ and the Laplace-deRham operator $\boldsymbol{\Delta}^{\mathrm{dR}}$ instead of the Bochner Laplacian $\boldsymbol{\Delta}^{\mathrm{B}}$ has been derived as a thin-film limit in [NNPV18] and models the L^2-gradient flow of a weak surface Frank-Oseen energy. The different operators result from different one-constant approximations in the Frank-Oseen energy, see [NRV18] for details.

Again, an additional geometric term $\mathcal{B}^2\mathbf{p}$ enters in this equation, if compared with the corresponding model in flat space. This term results from the influence of the embedding [NV12, SSV14, NNPV18]. The coupled system of equations (6.10), (6.11) and (6.12) with $v_{\boldsymbol{\nu}} = 0$ can be considered as the surface counterpart of the model in [LL00]. A related surface model has been proposed and analyzed in [Shk02]. However, this model is derived from a variational principle on a stationary surface and thus only contains intrinsic terms. It differs from equations (6.10), (6.11) and (6.12) with $v_{\boldsymbol{\nu}} = 0$ by the extrinsic term $\mathcal{B}^2\mathbf{p}$ and the extrinsic contribution in the surface Ericksen stress tensor $(\mathcal{B}\mathbf{p}) \otimes (\mathcal{B}\mathbf{p})$. We will numerically demonstrate the influence of the additional geometric terms. If $v_{\boldsymbol{\nu}} \neq 0$ further coupling terms occur. For a general discussion on transport of vector-valued quantities on evolving surfaces we refer to [NV18].

Next, we introduce the Cartesian extension of the resulting system of vector-valued surface PDEs (6.10), (6.11) and (6.12) according to Section 2.4. Thus, the corresponding extended problem of equations (6.10) and (6.11) reads

$$\boldsymbol{\pi}\partial_t\widehat{\mathbf{v}} + \mathrm{rot}_{\mathcal{S}}\,\widehat{\mathbf{v}}\boldsymbol{\nu} \times \widehat{\mathbf{v}} - v_{\boldsymbol{\nu}}\mathcal{B}\widehat{\mathbf{v}} = -\nabla_{\mathcal{S}}\bar{p} + \frac{1}{\mathrm{Re}}\left(\mathrm{Rot}_{\mathcal{S}}\,\mathrm{rot}_{\mathcal{S}}\,\widehat{\mathbf{v}} + 2\kappa\widehat{\mathbf{v}}\right) - \lambda\,\mathrm{div}_{\mathcal{S}}\,\widehat{\boldsymbol{\sigma}}_{\mathcal{S}}^{\mathrm{E}}$$
$$+ \mathbf{f}_G - \alpha_{\mathbf{v}}(\widehat{\mathbf{v}} \cdot \boldsymbol{\nu})\boldsymbol{\nu} \qquad (6.13)$$
$$\mathrm{div}_{\mathcal{S}}\,\widehat{\mathbf{v}} = v_{\boldsymbol{\nu}}\mathcal{H} \qquad (6.14)$$

with initial condition $\widehat{\mathbf{v}}\left(\cdot, t\right)|_{t=0} = \widehat{\mathbf{v}}_0(\cdot)$, the extended surface Ericksen stress tensor $\widehat{\boldsymbol{\sigma}}_{\mathcal{S}}^{\mathrm{E}} = (\nabla_{\mathcal{S}}\widehat{\mathbf{p}})^T\nabla_{\mathcal{S}}\widehat{\mathbf{p}} + (\mathcal{B}\widehat{\mathbf{p}}) \otimes (\mathcal{B}\widehat{\mathbf{p}})$ and the abbreviation

$$\mathbf{f}_G := \frac{2}{\mathrm{Re}}\left(\mathcal{H}\nabla_{\mathcal{S}}v_{\boldsymbol{\nu}} - \mathcal{B}\nabla_{\mathcal{S}}v_{\boldsymbol{\nu}}\right) + v_{\boldsymbol{\nu}}\nabla_{\mathcal{S}}v_{\boldsymbol{\nu}}$$

according to equation (4.3). Thereby, the alternative formulation of the viscous terms as proposed in equation (2.30), the alternative version of the transport term $\boldsymbol{\nabla}_{\widehat{\mathbf{v}}}\widehat{\mathbf{v}} = \frac{1}{2}\nabla_{\mathcal{S}}(\widehat{\mathbf{v}} \cdot \widehat{\mathbf{v}}) + \mathrm{rot}_{\mathcal{S}}\,\widehat{\mathbf{v}}\boldsymbol{\nu} \times \widehat{\mathbf{v}}$ (cf. Section 3.1 and Chapter 4) and $\bar{p} = p + \frac{1}{2}\widehat{\mathbf{v}} \cdot \widehat{\mathbf{v}}$ were used. Moreover, the corresponding extended problem of equation (6.12) reads

$$\boldsymbol{\pi}\partial_t\widehat{\mathbf{p}} + \boldsymbol{\nabla}_{\widehat{\mathbf{v}}}\widehat{\mathbf{p}} = \eta_p\left(\boldsymbol{\Delta}^{\mathrm{B}}\widehat{\mathbf{p}} - \mathcal{B}^2\widehat{\mathbf{p}}\right) - \omega_n\left(\|\widehat{\mathbf{p}}\|^2 - 1\right)\widehat{\mathbf{p}} - \alpha_{\mathbf{p}}\left(\boldsymbol{\nu} \cdot \widehat{\mathbf{p}}\right)\boldsymbol{\nu} \qquad (6.15)$$

with initial condition $\widehat{\mathbf{p}}\left(\cdot, t\right)|_{t=0} = \widehat{\mathbf{p}}_0(\cdot)$. The normal components $\widehat{\mathbf{v}} \cdot \boldsymbol{\nu}$ and $\widehat{\mathbf{p}} \cdot \boldsymbol{\nu}$ are penalized by the additional terms $\alpha_{\mathbf{v}}(\boldsymbol{\nu} \cdot \widehat{\mathbf{v}})\boldsymbol{\nu}$ and $\alpha_{\mathbf{p}}(\boldsymbol{\nu} \cdot \widehat{\mathbf{p}})\boldsymbol{\nu}$. Equations (6.13), (6.14) and (6.15) can now be solved for each component of the velocity $\widehat{\mathbf{v}}$, the director field $\widehat{\mathbf{p}}$ and the pressure $\bar{p}$ using standard approaches for scalar-valued problems on surfaces, such as the surface finite element method [DE07b, DE07a, DE13], levelset approaches [BCOS01, GBS06, SV08, DE08] or diffuse interface approximations [RV06]. However, to efficiently solve the incompressible surface Navier-Stokes equation (6.13)-(6.14), we use the same trick as introduced in Chapter 4. The numerical cost is drastically reduced by applying $\boldsymbol{\nu} \times$ to equation (6.13) and considering the rotated velocity field $\widehat{\mathbf{w}} := \boldsymbol{\nu} \times \widehat{\mathbf{v}}$. Thus, the rotated version of system (6.13)-(6.14) with normal penalization of the rotated velocity $\widehat{\mathbf{w}}$ reads

$$\boldsymbol{\pi}\partial_t\widehat{\mathbf{w}} - \operatorname{div}_{\mathcal{S}} \widehat{\mathbf{w}}\boldsymbol{\nu} \times \widehat{\mathbf{w}} = -\operatorname{Rot}_{\mathcal{S}} \bar{p} + \frac{1}{\operatorname{Re}} \left(\nabla_{\mathcal{S}} \operatorname{div}_{\mathcal{S}} \widehat{\mathbf{w}} + 2\kappa\widehat{\mathbf{w}}\right) + \mathbf{f}_G^{\perp} - \alpha_{\mathbf{w}} \left(\widehat{\mathbf{w}} \cdot \boldsymbol{\nu}\right) \boldsymbol{\nu}$$
$$- v_{\boldsymbol{\nu}}\boldsymbol{\nu} \times \left(\mathcal{B}\left(\boldsymbol{\nu} \times \widehat{\mathbf{w}}\right)\right) - \lambda\boldsymbol{\nu} \times \operatorname{div}_{\mathcal{S}} \widehat{\boldsymbol{\sigma}}_{\mathcal{S}}^{\mathrm{E}} \tag{6.16}$$
$$\operatorname{rot}_{\mathcal{S}} \widehat{\mathbf{w}} - v_{\boldsymbol{\nu}}\mathcal{H} = 0 \tag{6.17}$$

with initial condition $\widehat{\mathbf{w}}\left(\cdot, t\right)|_{t=0} = \boldsymbol{\nu} \times \widehat{\mathbf{v}}_0(\cdot) =: \widehat{\mathbf{w}}_0(\cdot)$ and $\mathbf{f}_G^{\perp} := \boldsymbol{\nu} \times \mathbf{f}_G$.

6.3 Numerical approach

6.3.1 Time discretization

We consider a simple operator splitting approach and solve the system (6.16)-(6.17) and the equation (6.15) iteratively in each time step. For the discretization in time of equations (6.16) and (6.17) we again use the same approach proposed in Chapter 4, i. e. the Chorin projection method Problem 4.2, and for equations (6.15) we use a semi-implicit Euler time discretization. Let the time interval $(0, t_{\mathrm{end}}]$ with end time t_{end} be divided into a sequence of discrete times $0 < t_0 < t_1 < ...$ with time step width $\tau^m = t_m - t_{m-1}$. Thereby, m denotes the time step number. The vector field $\widehat{\mathbf{w}}^m(\boldsymbol{x})$ corresponds to the respective rotated velocity field $\widehat{\mathbf{w}}(\boldsymbol{x}, t^m)$. All other quantities follow the same notation as in Chapter 4. Furthermore, we define the discrete time derivatives $\mathrm{d}_{\tau^m}^{\widehat{\mathbf{w}}} := \frac{1}{\tau^m} \left(\widehat{\mathbf{w}}^* - \boldsymbol{\pi}\widehat{\mathbf{w}}^{m-1}\right)$

and $\mathrm{d}\widehat{\mathbf{p}}_{\tau^m} := \frac{1}{\tau^m}(\widehat{\mathbf{p}}^m - \boldsymbol{\pi}\widehat{\mathbf{p}}^{m-1})$, with $\boldsymbol{\pi}$ the projection to the surface at time $t = t_m$. Thus, we get the time-discrete version of system (6.16)- (6.17)

$$\mathrm{d}\widehat{\mathbf{w}}_{\tau^m} - \operatorname{div}_{\mathcal{S}} \widehat{\mathbf{w}}^* \boldsymbol{\nu} \times \widehat{\mathbf{w}}^{m-1} = \frac{1}{\mathrm{Re}}(\nabla_{\mathcal{S}} \operatorname{div}_{\mathcal{S}} \widehat{\mathbf{w}}^* + 2\kappa\widehat{\mathbf{w}}^*) + \mathbf{f}_G^{\perp} - \lambda\boldsymbol{\nu} \times \operatorname{div}_{\mathcal{S}} \widehat{\boldsymbol{\sigma}}_{\mathcal{S}}^{\mathrm{E}}$$

$$- v_{\boldsymbol{\nu}}\boldsymbol{\nu} \times (\mathcal{B}(\boldsymbol{\nu} \times \widehat{\mathbf{w}}^*)) - \alpha_{\mathbf{w}}(\widehat{\mathbf{w}}^* \cdot \boldsymbol{\nu})\boldsymbol{\nu} \quad (6.18)$$

$$\tau^m \Delta_{\mathcal{S}} \bar{p}^m = \operatorname{rot}_{\mathcal{S}} \widehat{\mathbf{w}}^* - v_{\boldsymbol{\nu}}\mathcal{H} \quad (6.19)$$

$$\widehat{\mathbf{w}}^m = \widehat{\mathbf{w}}^* - \tau^m \operatorname{Rot}_{\mathcal{S}} \bar{p}^m, \quad (6.20)$$

where $\widehat{\boldsymbol{\sigma}}_{\mathcal{S}}^{\mathrm{E}}$ is evaluated at the old timestep, i.e. $\widehat{\boldsymbol{\sigma}}_{\mathcal{S}}^{\mathrm{E}} = (\nabla_{\mathcal{S}}\widehat{\mathbf{p}}^{m-1})^T \nabla_{\mathcal{S}}\widehat{\mathbf{p}}^{m-1} + (\mathcal{B}\widehat{\mathbf{p}}^{m-1}) \otimes (\mathcal{B}\widehat{\mathbf{p}}^{m-1})$, and the time-discrete version of equation (6.15)

$$\mathrm{d}\widehat{\mathbf{p}}_{\tau^m} + \boldsymbol{\nabla}_{\widehat{\mathbf{v}}^m}\widehat{\mathbf{p}}^m = \eta_p\left(\boldsymbol{\Delta}^{\mathrm{B}}\widehat{\mathbf{p}}^m - \mathcal{B}^2\widehat{\mathbf{p}}^m\right) - \omega_n\left(\|\widehat{\mathbf{p}}^{m-1}\|^2 - 1\right)\widehat{\mathbf{p}}^m$$

$$- \alpha_{\mathbf{p}}(\boldsymbol{\nu} \cdot \widehat{\mathbf{p}}^m)\boldsymbol{\nu}. \quad (6.21)$$

Note that we used a Taylor-0 linearization of the norm-1 penalization term in (6.15) for better readability. In the following simulations this term is linearized in time by a Taylor-1 expansion, see [NNPV18] for details. The transport term in equation (6.15) as well as the term including the surface Ericksen stress tensor in equation (6.13) are coupling terms in the operator splitting scheme. Additionally, we employ an adaptive time-stepping scheme, which is based on the combination of changes in the surface Frank-Oseen energy, see the below equation (6.22), and the Courant-Friedrichs-Lewy (CFL) condition for fluid flows.

6.3.2 Space discretization

The considered extension of the tangential vector fields to the Euclidean space allows us to apply the surface finite element method [DE13] for each component of the respective vector field. Let $\mathcal{S}_h = \mathcal{S}_h(t)$ denote the interpolation of the surface $\mathcal{S} = \mathcal{S}(t)$ such that

$$\mathcal{S}_h := \bigcup_{T \in \mathcal{T}} T$$

with a conforming surface triangulation $\mathcal{T} = \mathcal{T}(t)$ of mesh size h_M at time $t = t_m$. Here, we consider each space, set and quantity at time $t = t_m$ and therefore omit indexing with the timestep number m for better readability (unless it is explicitly needed). Furthermore, we introduce the finite element space

$$V_h = \left\{ v \in \mathcal{C}^0(\mathcal{S}_h) \mid v_{|_T} \in \mathbb{P}^1(T), \ \forall T \in \mathcal{T} \right\}$$

with $\mathcal{C}^k(\mathcal{S}_h)$ the space of k-times continuously differentiable functions on $\mathcal{S}_h$ and $\mathbb{P}^r(T)$ the set of polynomial functions of degree r on $T \in \mathcal{T}$. The finite element space V_h is thereby used twice as trail and test space. Let $(\cdot, \cdot)$ denote the standard scalar product on $L^2(\mathcal{S}_h)$ with $L^2(\mathcal{S}_h)$ the space of square-integrable functions on $\mathcal{S}_h$. First, the surface finite element approximation of equations (6.18) and (6.19) is solved, which reads: For $m = 1, 2, 3, \ldots$, find $\widehat{\mathbf{w}}^* \in V_h^3, p^m \in V_h$ such that $\forall \mathbf{u} \in V_h^3, \forall q \in V_h$

$$\left(\mathrm{d}_{\tau^m}^{\widehat{\mathbf{w}}} - \mathrm{div}_{\mathcal{S}} \, \widehat{\mathbf{w}}^\star \boldsymbol{\nu} \times \widehat{\mathbf{w}}^{m-1} + v_{\boldsymbol{\nu}} \boldsymbol{\nu} \times (\mathcal{B}\,(\boldsymbol{\nu} \times \widehat{\mathbf{w}}^\star)) - \mathbf{f}_G^\perp + \alpha_\mathbf{w}\,(\widehat{\mathbf{w}}^\star \cdot \boldsymbol{\nu})\,\boldsymbol{\nu} \ , \ \mathbf{u} \right)$$
$$= \frac{1}{\mathrm{Re}} \left(\mathrm{div}_{\mathcal{S}} \, \widehat{\mathbf{w}}^\star \ , \ \mathrm{div}_{\mathcal{S}} \, \mathbf{u} \right) + \frac{2}{\mathrm{Re}} \left(\kappa \widehat{\mathbf{w}}^\star \ , \ \mathbf{u} \right)$$
$$- \left(\lambda \widehat{\boldsymbol{\sigma}}_{\mathcal{S}}^\mathrm{E} \ , \ \nabla_{\mathcal{S}}\,(\boldsymbol{\nu} \times \mathbf{u}) \right)$$
$$\left(\tau^m \nabla_{\mathcal{S}} \bar{p}^m + \boldsymbol{\nu} \times \widehat{\mathbf{w}}^\star \ , \ \nabla_{\mathcal{S}} q \right) = \left(v_{\boldsymbol{\nu}} \mathcal{H} \ , \ q \right).$$

The corresponding finite element approximation for the i-th component of $\widehat{\mathbf{w}}^\star$ follows by testing with $\mathbf{u} = \xi \mathbf{e}_i$ for $\xi \in V_h$, where $\mathbf{e}_i$ is the i-th unit vector in $\mathbb{R}^3$. Accordingly, the resulting vector field $\widehat{\mathbf{w}}^*$ is used to determine $\widehat{\mathbf{w}}^m$ by the pressure correction step in equation (6.20). The transformation $\widehat{\mathbf{v}}^m = -\boldsymbol{\nu} \times \widehat{\mathbf{w}}^m$ leads to the velocity field at the new timestep t_m. Note that in the above discrete system only the simple Chorin projection method is considered, i.e. Algorithm 4.1 with only one iteration, due to better readability. In the following simulations we additionally use the pressure relaxation scheme Algorithm 4.2, for which the finite element approximation can be easily derived along the same lines. Finally, the surface finite element approximation of equation (6.21) is

solved, which reads: For $m = 1, 2, 3, \ldots$, find $\widehat{\mathbf{p}}^m \in V_h$ such that $\forall \mathbf{q} \in V_h^3$

$$
\left(\mathrm{d}\widehat{\mathbf{p}}_{\tau^m} + \widehat{\mathbf{v}}_i^m \mathcal{D}_i \widehat{\mathbf{p}}^m \ , \ \mathbf{q} \right) = \left(\eta_p \nabla_{\mathcal{S}} \widehat{\mathbf{p}}^m \ , \ \nabla_{\mathcal{S}} \mathbf{q} \right) - \left(\omega_n \left(\|\widehat{\mathbf{p}}^{m-1}\|^2 - 1 \right) \widehat{\mathbf{p}}^m \ , \ \mathbf{q} \right)
$$
$$
- \left(\eta_p \mathcal{B}^2 \widehat{\mathbf{p}}^m + \alpha_{\mathbf{p}} \left(\boldsymbol{\nu} \cdot \widehat{\mathbf{p}}^m \right) \boldsymbol{\nu} \ , \ \mathbf{q} \right) .
$$

Again, testing with $\mathbf{q} = \xi \mathbf{e}_i$ for $\xi \in V_h$ yields the corresponding finite element approximation for the i-th component of $\widehat{\mathbf{p}}^m$. As is the previous chapters, the resulting discrete systems are implemented in the finite element toolbox AMDiS [VV07, WLPV15], where we additionally use a domain decomposition approach to efficiently distribute the workload on many-core-platforms. As linear solver for both systems a BiCGStab(l) method with $l = 2$ and a Jacobi preconditioner is used.

6.4 Simulation results

In the following simulations we use $\lambda = 0.5$, $\alpha_{\mathbf{w}} = 10^2$, $\omega_n = 10^2$ and $\alpha_{\mathbf{p}} = 10^5$. We compare the numerical solution of equations (6.13), (6.14) and (6.15) (the so-called *wet* case) with the numerical solution of equation (6.15) with $\widehat{\mathbf{v}} = 0$ (the so-called *dry* case). To highlight the differences we take the surface Frank-Oseen energy

$$
\mathcal{F}^{\mathbf{P}} := \int_{\mathcal{S}} \frac{\eta_p}{2} \left(\|\nabla_{\mathcal{S}} \widehat{\mathbf{p}}\|^2 + (\mathcal{B}\widehat{\mathbf{p}})^2 \right) + \frac{\omega_n}{4} \left(\|\widehat{\mathbf{p}}\|^2 - 1 \right)^2 + \frac{\alpha_{\mathbf{p}}}{2} \left(\widehat{\mathbf{p}} \cdot \boldsymbol{\nu} \right)^2 \, \mathrm{d}\mathcal{S} \quad (6.22)
$$

and the surface kinetic energy

$$
\mathcal{F}^{\mathrm{kin}} := \frac{1}{2} \int_{\mathcal{S}} \|\widehat{\mathbf{v}}\|^2 \, \mathrm{d}\mathcal{S} \quad (6.23)
$$

into account.

First, we consider a stationary ($v_{\boldsymbol{\nu}} = 0$) ellipsoidal surface with major axes parameters $(0.7, 0.7, 1.2)$. We use the trivial solution as initial condition for the velocity and for the director field $\widehat{\mathbf{p}}_0 = \nabla_{\mathcal{S}} \psi_0 / \|\nabla_{\mathcal{S}} \psi_0\|$, where $\psi_0 = x/10 + y + z/10$ and $\boldsymbol{x} = (x, y, z)^T \in \mathcal{S}$. This generates an out-of-equilibrium solution with two $+1$ defects – more precisely a source and a sink. Furthermore, we use $\mathrm{Re} = 0.5$,
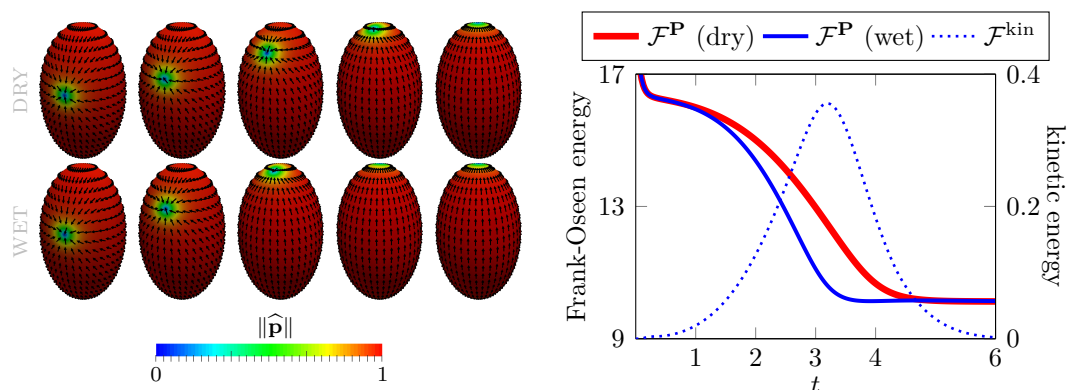
Figure 6.1: Left: Evolution of the director field $\widehat{\mathbf{p}}$ on a stationary ellipsoid of the dry case (top row) and the wet case (bottom row) for $t = 1, 2, 3, 4, 6$ (left to right). Right: Surface Frank-Oseen energy $\mathcal{F}^{\mathbf{P}}$ and surface kinetic energy $\mathcal{F}^{\mathrm{kin}}$ against time t for the dry and the wet case, respectively.

$\eta_p = 0.6$ and $h_{\mathrm{M}} = 1.32 \cdot 10^{-2}$. Figure 6.1 shows the influence of the hydro-dynamics on the dynamical evolution of the director field. The two defects, which fulfill the Poincaré-Hopf theorem (2.18), evolve towards the geometrically favorable positions of high Gaussian curvature, the director field aligns with the minimal curvature lines of the geometry and – as in flat space – the hydro-dynamics enhances the evolution towards the equilibrium configuration, which coincides for the dry and the wet case.

In the next example we consider a stationary torus with major radius $R = 2$, minor radius $r = 0.5$ and the z-axis as symmetry axis. Again, we use the trivial solution as initial condition for the velocity $\widehat{\mathbf{v}}$ and a random (normalized) vector field for the director field $\widehat{\mathbf{p}}$. Here, we use the simulation parameters $\mathrm{Re} = 1$ and $\eta_p = 0.4$. The mesh size is fixed at $h_{\mathrm{M}} = 2.74 \cdot 10^{-2}$. All other parameters are equal to that used in Figure 6.1. In Figure 6.2 we focus on the annihilation of defects in one realization. Figure 6.2 (top) shows the evolution of the director field $\widehat{\mathbf{p}}$ for the dry and the wet case. Again in the wet case the dynamic is enhanced, which is quantified by the stronger overall decay of the surface Frank-Oseen energy, cf. Figure 6.2 (middle). Additionally, in Figure 6.2 (bottom) the corresponding flow field $\widehat{\mathbf{v}}$ is shown for the considered annihilation of a source ($+1$) and a saddle (-1) defect in the director field $\widehat{\mathbf{p}}$. After all defects are annihilated, which again is in accordance with the Poincaré-Hopf theorem
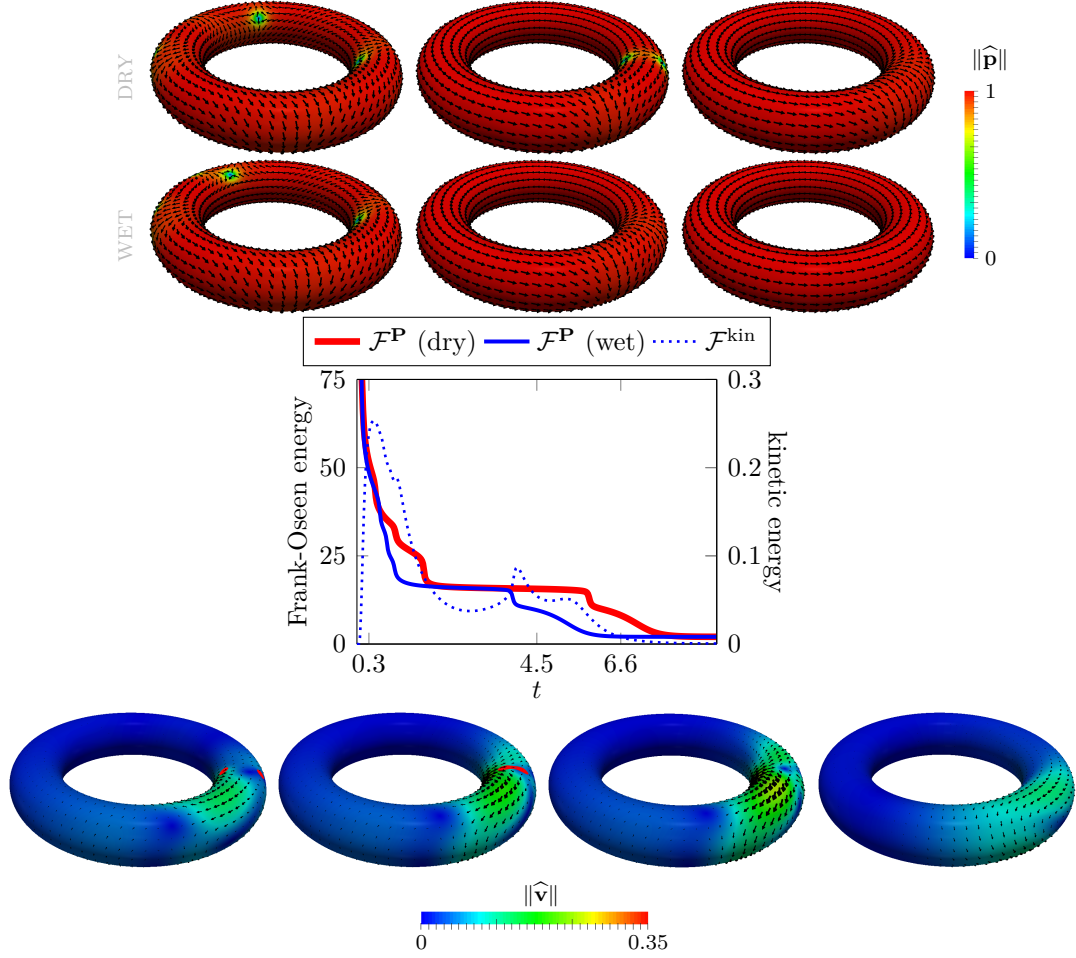
Figure 6.2: Top: Evolution of the director field $\widehat{\mathbf{p}}$ on a torus of the dry case (top row) and the wet case (bottom row) for $t = 0.3$, 4.5, 6.6 (left to right). Middle: Surface Frank-Oseen energy $\mathcal{F}^{\mathbf{P}}$ and surface kinetic energy $\mathcal{F}^{\text{kin}}$ against time t for the dry and the wet case, respectively. Bottom: Velocity field $\widehat{\mathbf{v}}$ for the annihilation of a source ($+1$, left) and a saddle (-1, right) defect in the director field $\widehat{\mathbf{p}}$ (red dots) for $t = 3$, 3.81, 4.05, 5.7 (left to right).

(2.18), the velocity field $\widehat{\mathbf{v}}$ becomes a Killing vector field and the director field $\widehat{\mathbf{p}}$ aligns with the minimal curvature lines of the geometry. The reached equilibrium configurations coincide for both cases, the dry and the wet case.

While in the two previous examples the expected minimal energy configuration was reached, we now consider an initial condition for which only a local minima can be reached. We use $\widehat{\mathbf{p}}_0 = \nabla_{\mathcal{S}}\psi_0/\|\nabla_{\mathcal{S}}\psi_0\|$, where $\psi_0(\boldsymbol{x}) = \exp\left(-(\boldsymbol{x}-\mathbf{m})^2/2\right)$
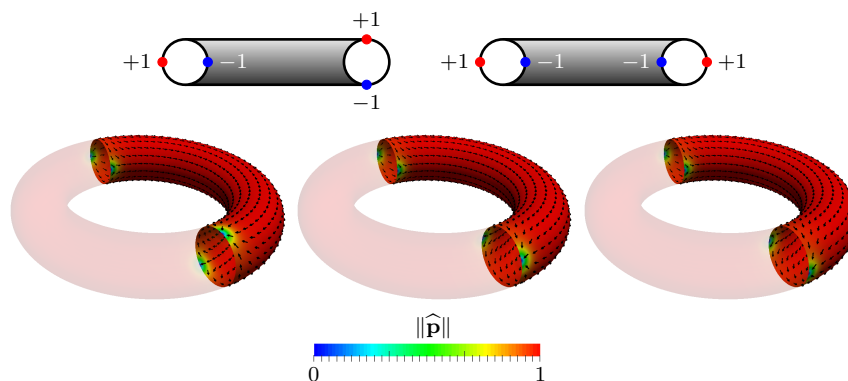
Figure 6.3: *Top: Schematic defect positions of the initial condition (left) and the final configuration (right) on a torus with the analytical initial condition for the director field $\widehat{\mathbf{p}}$ and zero initial condition for the velocity field $\widehat{\mathbf{v}}$. Red dots are indicating $+1$ defects (sources or sinks) and blue dots are indicating -1 defects (saddles). Bottom: Evolution of the director field $\widehat{\mathbf{p}}$ in the wet case for $t = 1,\ 5,\ 25$ (left to right).*
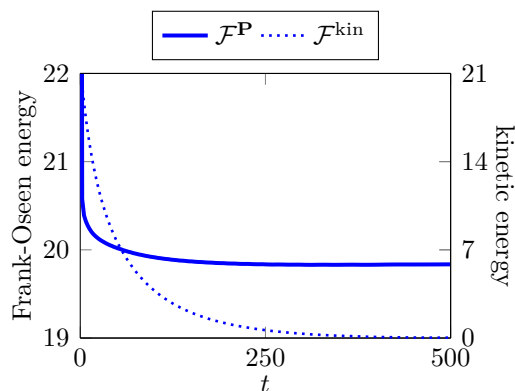
Figure 6.4: *Surface Frank-Oseen energy $\mathcal{F}^{\mathbf{P}}$ and surface kinetic energy $\mathcal{F}^{\mathrm{kin}}$ against time t for the analytical initial condition for the director field $\widehat{\mathbf{p}}$ and the Killing vector field as initial condition for the velocity $\widehat{\mathbf{v}}$.*

with $\boldsymbol{x} \in \mathcal{S}$ and $\mathbf{m} = (R, 0, r)^T \in \mathbb{R}^3$, as initial condition for the director field. This produces two ± 1 defect pairs which are located in opposite position to each other along the toroidal direction of the torus, again fulfilling the Poincaré-Hopf theorem (2.18). Thereby, one pair is rotated by an angle of $\pi/2$ compared to the other along the poloidal direction, see Figure 6.3. The parameters are adapted to $\mathrm{Re} = 1$, $\eta_p = 0.4$ and $h_{\mathrm{M}} = 2.74 \cdot 10^{-2}$. In a flat geometry with zero curvature such defect pairs would annihilate. However, due to the geometric interaction in
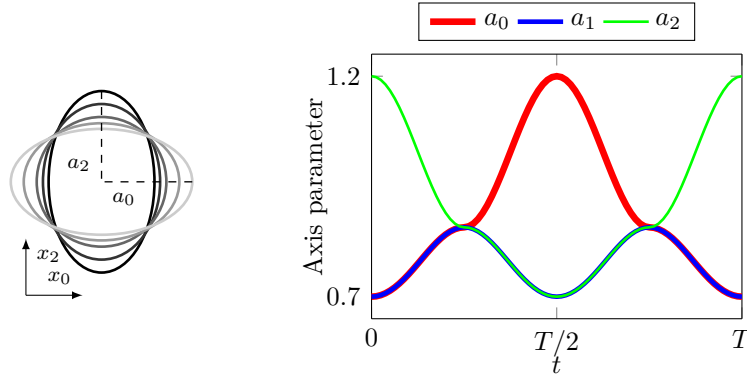
Figure 6.5: Left: Schematic description of the ellipsoid evolution for a half period of oscillation. Descending gray scale indicates increasing time. The motion in the second half of the oscillation is reversed, respectively. Right: Major axes parameters for the ellipsoid over a full period of oscillation. The time of one oscillation period is considered to be $T = 160$. The major axes parameters are chosen such that the surface area of the ellipsoid is conserved over time.

the present case resulting from the difference of the Gaussian curvature inside and outside of the torus, the reached nontrivial defect configuration is stable and the two ± 1 defect pairs remain over time. The -1 defects are attracted to regions with negative Gaussian curvature, i.e. the inner of the torus, and $+1$ defects are attracted to regions with positive Gaussian curvature, i.e. the outer of the torus, see Figure 6.3. The reached configuration, is a local minimum with a significantly larger surface Frank-Oseen energy $\mathcal{F}^{\mathbf{P}}$ as the defect-free configuration. In this example we did not find any significant difference between the dry and the wet case, when the zero initial condition for the velocity $\widehat{\mathbf{v}}$ is used. However, if we use a Killing vector field for the velocity as initial condition, i.e. $\widehat{\mathbf{v}}_0(\boldsymbol{x}) = 1/2(-y, x, 0)^T$ with $\boldsymbol{x} = (x, y, z)^T \in \mathcal{S}$, cf. [NRV17, RV18b], the four defects start to rotate and cause a damping of the flow field, which converges to zero. In other words, the defects in the director field produce an additional contribution to the total surface stress tensor and therefore the kinetic energy dissipates to zero, see Figure 6.4. Thus, the final configuration is just a rotation of the configuration reached with $\widehat{\mathbf{v}}_0 = 0$.

Now, we let the ellipsoid from Figure 6.1 evolve by prescribing the normal velocity $v_{\boldsymbol{\nu}}$, such that the ellipsoid changes to a sphere and afterwards to an ellipsoid with a different axis orientation and vice versa to obtain a shape oscillation. The
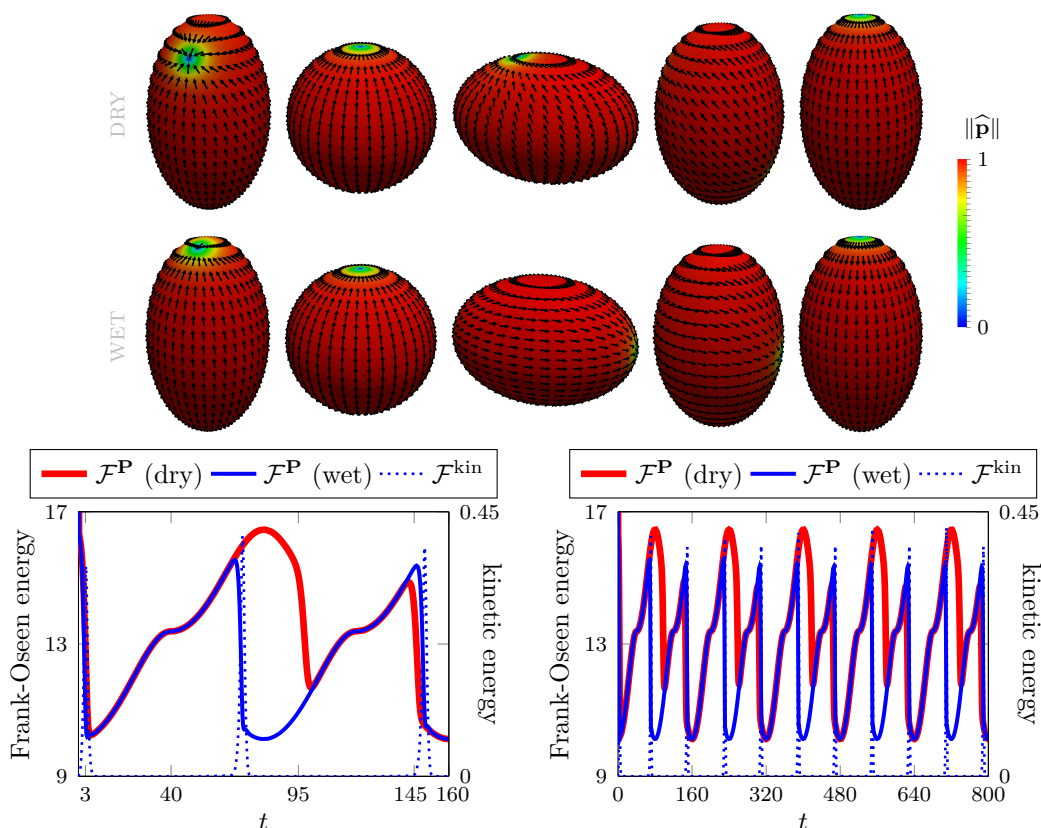
Figure 6.6: Top: Evolution of the director field $\widehat{\mathbf{p}}$ on a evolving ellipsoid of the dry case (top row) and the wet case (bottom row) for $t = 3, 40, 95, 145, 160$ (left to right). Bottom: Surface Frank-Oseen energy $\mathcal{F}^{\mathbf{P}}$ and surface kinetic energy $\mathcal{F}^{\text{kin}}$ against time t for the first period of oscillation (left) and over five periods of oscillation (right) for the dry and the wet case, respectively.

surface area remains constant during the evolution. Figure 6.5 shows schematically the evolution of the geometry and the axes parameters for one period of oscillation. Here, we use the same simulation parameters and initial conditions as considered in Figure 6.1. The evolution of the director field $\widehat{\mathbf{p}}$ is shown in Figure 6.6 (top), again for the dry (top row) and the wet case (bottom row). The defect positions again reallocate at their geometrically favorable position. However, due to the change in geometry the time scale for the reallocation competes with the time scale for the shape changes. The enhanced evolution towards the minimal energy configuration with hydrodynamics becomes even more significant in these situations. Already slight modifications of the geometry are enough

to push the defect after crossing the sphere configurations (with no preferred defect position) to the energetically favorable state. In the dry case there is a strong delay and much stronger shape changes are needed to push the defect to the energetically favorable position. First, an energy barrier for reallocating the defect position has to be overcome, which is shown by the further increase of the red line after the blue line has already dropped after crossing the sphere configuration in Figure 6.6 (middle). The parameters and the initial condition are chosen in such a way that in the dry case the defects do not quite reach the position at the poles, if the shape evolution crosses the sphere. In the wet case they have moved beyond. This results in a constant orientation in the dry case and a flipping of the orientation of the director field in the wet case after each oscillation. The final configuration in Figure 6.6 after completing one oscillation cycle is energetically equivalent for the dry and the wet case, even if the orientation of the director field $\widehat{\mathbf{p}}$ differs. This behavior clearly depends on the used parameters. However, it also demonstrates the strong influence hydrodynamics might have in such highly nonlinear systems, where the topology, geometric properties and defect dynamics are strongly coupled.

These examples together with the demonstrated energy reduction by creation of additional defects in geometrically favored positions in [NNPV18], which is expected to hold also for the wet case, lead to a very rich phase space, whose exploration is beyond the scope of this chapter.

6.5 Discussion

Equations (6.10), (6.11) and (6.12) have been derived as a thin-film limit of a three-dimensional simplified Ericksen-Leslie model in [NRV18]. In [Shk02] a similar model was proposed, which differs from equations (6.10), (6.11) and (6.12) on stationary surfaces ($v_{\boldsymbol{\nu}} = 0$) in the extrinsic contributions. Especially the surface Ericksen stress tensor is considered to be $\boldsymbol{\sigma}_{\mathcal{S}}^{\mathrm{E}} = (\nabla_{\mathcal{S}}\mathbf{p})^{T}\nabla_{\mathcal{S}}\mathbf{p}$. To show the strong difference between this intrinsic and the extrinsic surface Ericksen stress tensor from above $\boldsymbol{\sigma}_{\mathcal{S}}^{\mathrm{E}} = (\nabla_{\mathcal{S}}\mathbf{p})^{T}\nabla_{\mathcal{S}}\mathbf{p} + (\mathcal{B}\mathbf{p}) \otimes (\mathcal{B}\mathbf{p})$, we come back to the stationary ellipsoid in Figure 6.1, but with slightly different parameters, i.e. Re $= 2$, $\eta_p = 0.3$ and $\lambda = 1$. These parameters lead to a damped oscillation
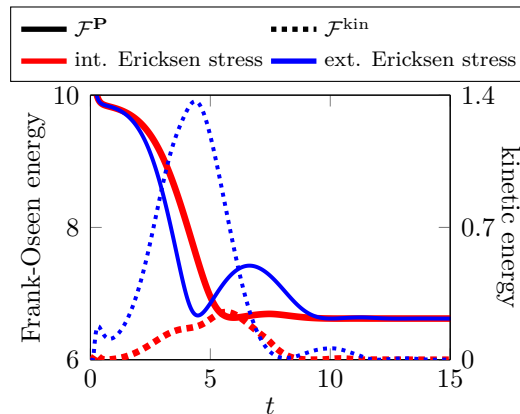
Figure 6.7: Surface Frank-Oseen energy $\mathcal{F}^{\mathbf{P}}$ and surface kinetic energy $\mathcal{F}^{\mathrm{kin}}$ against time t for the simulation of the damped oscillation of the defects around the minimal defect configuration.

of the defects around the energetically favorable positions before they reach the final state configuration as in Figure 6.1. In Figure 6.7 the differences in the time evolution of the surface Frank-Oseen energy as well as the surface kinetic energy for both cases, the intrinsic and extrinsic surface Ericksen stress, are shown. The influence of the hydrodynamics is much stronger for the extrinsic surface Ericksen stress. Together with the example in Figure 6.6 such differences in the dynamics might have a huge impact on the overall evolution, if also shape changes are considered. We would also like to point out, that even if the thin-film limit of the individual equations in system (6.10), (6.11) and (6.12), namely the surface Navier-Stokes and the surface Frank-Oseen equation, are known [RV15, RV18a, NNPV18], a naive transformation of the missing coupling term from the three-dimensional formulation to its surface counterpart will not be sufficient to obtain the extrinsic surface Ericksen stress term. Only a thin-film limit of the complete model, with appropriate boundary conditions, will lead to the full model, see [NRV18].

6.6 Conclusion

We have introduced a minimal model for surface LCs on evolving surfaces. This model follows by a thin film limit of the three dimensional simplified Ericksen-

Leslie model [LL00]. The basic ideas of the limiting process are briefly sketched and the resulting local equations are extended to the Euclidean basis according to Chapter 2. The surface finite element method is used to numerically solve the final system of vector-valued surface PDEs for each component of the respective vector field. Similar to Chapter 4 the rotated velocity field is considered to reduce the numerical effort and the Chorin projection method is applied to the incompressible surface Navier-Stokes equation. In various numerical experiments we have demonstrated the strong influence of the flow field on the orientational ordering. On ellipsoidal and toroidal surfaces some expected and unexpected phenomena were presented, in which a highly nonlinear coupling of hydrodynamics, topology, geometric properties, shape changes and defect dynamics can be observed.

7 | Conclusion

7.1 Summary

In this thesis, we have studied the hydrodynamic behavior of fluid interfaces, which are considered as two-dimensional evolving surfaces. We have introduced the required notation, basic concepts for the appearance of defects in the flow field and a general concept to numerically treat vector-valued surface PDEs in Chapter 2. Moreover, the incompressible surface Navier-Stokes equation is derived and introduced. The geometric terms in the resulting equation accounts for a highly nonlinear interplay between topology, geometry, fluid properties and defect dynamics, which can induce non-uniform surface flow patterns. In Chapter 3, we have reformulated the incompressible surface Navier-Stokes equation by the vorticity-stream function formulation. The resulting equations of this alternative approach is a system of scalar-valued surface PDEs and therefore the standard surface finite element method is used to discretize this system in space. Furthermore, we have considered designed numerical examples, which show the strong interplay between the geometry and the hydrodynamics. Additionally, numerical examples on evolving surfaces are presented which show the highly nonlinear dynamic behavior through geometric shape changes. The vorticity-stream function approach is limited to surfaces, which are topologically invariant to a sphere, see Section 3.4. To circumvent this issue, a direct discretization technique of the incompressible surface Navier-Stokes equation in its original form has been considered in Chapter 4. More precisely, the approach is based on the extended version of the equations, the Chorin projection method and the standard surface finite element method. A numerical study of the experimental order of convergence for the proposed Chorin projection algorithm is proposed. The accuracy of the fully discrete scheme is validated against a

107

numerical solution based on discrete exterior calculus on a torus from the literature. To demonstrate that this approach has the ability to work on more general surfaces independent of the genus $g(\mathcal{S})$, we have numerically studied the interesting interplay between the topology of the surface and the hydrodynamics in the flow field on n-tori. Additionally, we have shown the strong influence of shape changes to the flow field based on a non-uniform evolution of the nonic surface. In the remaining chapters, two extensions of the proposed methods have been considered. E.g. in Chapter 5, a model for a stationary fluid interface in viscous fluids is derived. This system can be seen as two-phase flow problem with an interface condition based on the incompressible surface Navier-Stokes equation. We have used the vorticity-stream function formulation for describing the interfacial hydrodynamics and the basic ideas of the diffuse domain/diffuse interface approach in order to reformulate the whole system of equations with phase fields. The results are compared with an experiment based on vesicles in shear flow and the numerical convergence of the present approach to the experimental data is shown. Moreover, the influence of the non-constant Gaussian curvature of ellipsoidal shaped vesicles on the flow field is studied and analyzed. A further extension is proposed in Chapter 6, which describes polar liquid crystals on evolving surfaces. Here, the approach from Chapter 4 is used in combination with an additional vector-valued surface PDE describing the orientational ordering of the liquid crystals. Again, the general concept proposed in Section 2.4 is applied to this additional equation. The resulting system is the surface counterpart of the simplified Ericksen-Leslie model for describing polar liquid crystals in flat space. Various examples are shown, which accounts for the strong influence of the flow field on the orientational ordering. Furthermore, we have studied some expected and unexpected phenomena on ellipsoidal and toroidal surfaces, which again show the highly nonlinear coupling of hydrodynamics, topology, geometric properties, shape changes and defect dynamics.

7.2 Outlook

The fluid film in the extension proposed in Chapter 5 is stationary. Considering the fluid interface as free surface would enable a broader range of applications,

e. g. vesicles under shear flow which are not adhered to a solid surface as considered in the experimental validation in Chapter 5. Thereby, the normal velocity follows physical principles such as conservation laws, which typically yields an additional surface PDE. Also the interaction of the interfacial and bulk hydrodynamics in spinodal decomposition in lipid bilayer membranes are of special interest. This has already been considered in [FHH10] but for planar membranes. However, both proposed approaches, i. e. the vorticity-stream function approach from Chapter 3 and the direct numerical treatment of the incompressible surface Navier-Stokes equation from Chapter 4, can be used in such physical problems.

In Chapter 6 the polar ordering of liquid crystals is considered. Another approach to describe liquid crystals follows by investigating the nematic ordering, where in contrast to the polar case the rod-like particles are seen without orientation. A model without the interfacial hydrodynamic effects on stationary surfaces has already been proposed in [NNP+18]. This typically involves tensor-valued surface PDEs, which can be handled in a similar way as in Section 2.4 and [NNV18], respectively. The extension to the more general case of evolving surfaces can be easily done by using [NV18]. Taking hydrodynamic effects into account requires the coupling of this tensor-valued equation with the incompressible surface Navier-Stokes equation. It is thereby noted that naively coupling the individual equations, i. e. along the same lines as in the three-dimensional case, is probably not sufficient. As in Chapter 6, we expect that only the thin-film limit of the three-dimensional counterpart, e. g. the so-called Beris-Edwards model [ADL13], yields the correct formulation on the evolving surface – especially for the coupling terms.

All these polar/nematic models for liquid crystals can be extended to model active liquid crystals on fluid interfaces. Such active suspensions transform chemical into kinetic energy which is the reason why these systems are never in equilibrium and the defects move randomly over the surface. Again, the hydrodynamics and the geometry are expected key ingredients for the dynamic behavior of the whole system and the tools provided within this theses can be used for describing the hydrodynamic effects.

Also the flow patterns in such active systems by itself are of special interest,

as considered, e. g., in [MSB$^+$18]. Here, the activity of the system is included in the surface stress tensor, which yields an extension of the incompressible surface Navier-Stokes equation by higher order terms (in terms of powers of the Laplacian). This causes a continuous energy input and the chaotic flow patterns. The extension of the method proposed in Chapter 4 to these more general higher order equations is ongoing work within a master's thesis in this institute and will be published elsewhere.

Bibliography

[AD09]   M. Arroyo and A. DeSimone. Relaxation dynamics of fluid mem-
             branes. *Phys. Rev. E*, 79:031915, 2009.

[ADL13]   H. Abels, G. Dolzmann, and Y. Liu. Strong solutions for the
             Beris-Edwards model for nematic liquid crystals with homoge-
             neous Dirichlet boundary conditions. *arXiv:1312.5988*, 2013.

[AMR88]   R. Abraham, J.E. Marsden, and T.S. Ratiu. *Manifolds, Tensor
             Analysis, and Applications*. Number 75 in Applied Mathematical
             Sciences. Springer, 1988.

[BCOS01]   M. Bertalmio, L.-T. Cheng, S. Osher, and G. Sapiro. Variational
             Problems and Partial Differential Equations on Implicit Surfaces.
             J. Comput. Phys., 174:759–780, 2001.

[BG09]   M. J. Bowick and L. Giomi. Two-Dimensional Matter: Order,
             Curvature and Defects. *Adv. Phys.*, 58:449–563, 2009.

[BGN15a]   J. W. Barrett, H. Garcke, and R. Nürnberg. Numerical compu-
             tations of the dynamics of fluidic membranes and vesicles. *Phys.
             Rev. E*, 92:052704, 2015.

[BGN15b]   J. W. Barrett, H. Garcke, and R. Nürnberg. Stable numerical ap-
             proximation of two-phase flow with a Boussinesq-Scriven surface
             fluid. *Commun. Math. Sci.*, 13:1829–1874, 2015.

[BKAS17]   N. D. Bade, R. Kamien, R. Assoian, and K. Stebe. Patterned
             Cell Alignment in Response to Macroscale Curvature. *Biophys.
             J.*, 112(3):536a, 2017.

[Boo05]   A. H. Boozer. Physics of magnetically confined plasmas. *Rev. Mod. Phys.*, 76:1071–1141, 2005.

[BP10]   D. Bothe and J. Prüss. On the Two-Phase Navier-Stokes Equations with Boussinesq-Scriven Surface Fluid. *J. Math. Fluid Mech.*, 12(1):133–150, 2010.

[BR06]   F. Bornemann and C. Rasch. Finite-element Discretization of Static Hamilton-Jacobi Equations based on a Local Variational Principle. *Comput. Vis. Sci.*, 9:57–69, 2006.

[BSZ10]   M. A. Bates, G. Skačej, and C. Zannoni. Defects and ordering in nematic coatings on uniaxial and biaxial colloids. *Soft Matter*, 6(3):655–663, 2010.

[Cal02]   D. Calhoun. A Cartesian Grid Method for Solving the Two-Dimensional Streamfunction-Vorticity Equations in Irregular Regions. *J. Comput. Phys.*, 176(2):231–275, 2002.

[Cho68]   A. J. Chorin. Numerical solution of the Navier-Stokes equations. *Math. Comp.*, 22:745–762, 1968.

[CKV07]   P. Cicuta, S. L. Keller, and S. L. Veatch. Diffusion of Liquid Domains in Lipid Bilayer Membranes. *J. Phys. Chem. B*, 111(13):3328–3331, 2007.

[CL95]   P. M. Chaikin and T. C. Lubensky. *Principles of condensed matter physics*. Cambridge University Press, 1995.

[CRT99]   C. Cao, M. A. Rammaha, and E. S. Titi. The Navier-Stokes equations on the rotating 2-D sphere: Gevrey regularity and asymptotic degrees of freedom. *Z. Angew. Math. Phys.*, 50(3):341–360, 1999.

[DE07a]   G. Dziuk and C. M. Elliott. Finite elements on evolving surfaces. *IMA J. Numer. Anal.*, 27:262–292, 2007.

[DE07b]   G. Dziuk and C. M. Elliott. Surface finite elements for parabolic equations. *J. Comput. Math.*, 25:385–407, 2007.

[DE08]   G. Dziuk and C. M. Elliott. Eulerian finite element method for parabolic PDEs on implicit surfaces. *Interfaces Free Bound.*, 10(1):119–138, 2008.

[DE13]   G. Dziuk and C. M. Elliott. Finite element methods for surface PDEs. *Acta Numer.*, 22:289–396, 2013.

[DF96]   G. Dörries and G. Foltin. Energy dissipation of fluid membranes. *Phys. Rev. E*, 53:2547–2550, 1996.

[dGP93]   P. G. de Gennes and J. Prost. *The Physics of Liquid Crystals.* Second Edition, Oxford Science Publications, 1993.

[DSL00]   J. Dzubiella, M. Schmidt, and H. Löwen. Topological defects in nematic droplets of hard spherocylinders. *Phys. Rev. E*, 62:5081–5091, 2000.

[DSOdlC12] S. Dhakal, F. J. Solis, and M. Olvera de la Cruz. Nematic liquid crystals on spherical surfaces: Control of defect configurations by temperature, density, and rod shape. *Phys. Rev. E*, 86:011709, 2012.

[DV87]   E. B. Dussan V. On the ability of drops to stick to surfaces of solids. Part 3. The influences of the motion of the surrounding fluid on dislodging drops. *J. Fluid Mech.*, 174:381–397, 1987.

[Dzi88]   G. Dziuk. *Finite Elements for the Beltrami operator on arbitrary surfaces*, pages 142–155. Springer Berlin Heidelberg, Berlin, Heidelberg, 1988.

[EL96]   W. E and J.-G. Liu. Vorticity Boundary Condition and Related Issues for Finite Difference Schemes. *J. Comput. Phys.*, 124(2):368–382, 1996.

[EM70]   D. G. Ebin and J. Marsden. Groups of Diffeomorphisms and the Motion of an Incompressible Fluid. *Ann. Math.*, 92:102–163, 1970.

[EPC⁺18]   P. W. Ellis, D. J. G. Pearce, Y.-W. Chang, G. Goldsztein, L. Giomi, and A. Fernandez-Nieves. Curvature-induced defect unbinding and dynamics in active nematic toroids. *Nat. Phys.*, 14:85–90, 2018.

[Eri61]   J. L. Ericksen. Conservation Laws for Liquid Crystals. *T. Soc. Rheo.*, 5(1):23–34, 1961.

[Eri76]   J. L. Ericksen. Equilibrium Theory of Liquid Crystals. In G. H. Brown, editor, *Advances in Liquid Crystals*, pages 233–298. Elsevier, 1976.

[ETK⁺07]   S. Elcott, Y. Tong, E. Kanso, P. Schröder, and M. Desbrun. Stable, circulation-preserving, simplicial fluids. *ACM T. Graphic.*, 26:4, 2007.

[FHH10]   J. Fan, T. Han, and M. Haataja. Hydrodynamic effects on spinodal decomposition kinetics in planar lipid bilayer membranes. *J. Chem. Phys.*, 133(23):235101, 2010.

[FNVU⁺07]   A. Fernández-Nieves, V. Vitelli, A. S. Utada, D. R. Link, M. Márquez, D. R. Nelson, and D. A. Weitz. Novel Defect Structures in Nematic Liquid Crystal Shells. *Phys. Rev. Lett.*, 99:157801, 2007.

[FRGV12]   S. Franz, H.-G. Roos, R. Gärtner, and A. Voigt. A Note on the Convergence Analysis of a Diffuse-domain Approach. *Comput. Meth. Appl. Mat.*, 12(2):153–167, 2012.

[GA18]   B. J. Gross and P. J. Atzberger. Hydrodynamic flows on curved surfaces: Spectral numerical methods for radial manifold shapes. *J. Comput. Phys.*, 371:663–689, 2018.

[GBJL16]   J. Gounley, G. Boedec, M. Jaeger, and M. Leonetti. Influence of surface viscosity on droplets in shear flow. *J. Fluid Mech.*, 791:464–494, 2016.

[GBS06]   J. B. Greer, A. L. Bertozzi, and G. Sapiro. Fourth order partial differential equations on general geometries. *J. Comput. Phys.*, 216:216–246, 2006.

[GKHC18]   R. E. Guerra, C. P. Kelleher, A. D. Hollingsworth, and P. M. Chaikin. Freezing on a sphere. *Nature*, 554:346, 2018.

[Hel73]   W. Helfrich. Elastic Properties of Lipid Bilayers - Theory and Possible Experiments. *Z. Naturforsch. C*, 28:693–703, 1973.

[HL10]   M. L. Henle and A. J. Levine. Hydrodynamics in curved membranes: The effect of geometry on particulate mobility. *Phys. Rev. E*, 81:011905, 2010.

[HLL16]   P. Hansbo, M. G. Larson, and K. Larsson. Analysis of Finite Element Methods for Vector Laplacians on Surfaces. *arXiv:1610.06747*, 2016.

[HLW14]   J. Huang, F. Lin, and C. Wang. Regularity and Existence of Global Solutions to the Ericksen–Leslie System in R2. *Commun. Math. Phys.*, 331(2):805–850, 2014.

[HMS$^+$08] M. L. Henle, R. McGorty, A. B. Schofield, A. D. Dinsmore, and A. J. Levine. The effect of curvature and topology on membrane hydrodynamics. *Europhys. Lett.*, 84(4):48001, 2008.

[HSWKG13]   A. R. Honerkamp-Smith, F. G. Woodhouse, V. Kantsler, and R. E. Goldstein. Membrane Viscosity Determined from Shear-Driven Flow in Giant Vesicles. *Phys. Rev. Lett.*, 111:038103, 2013.

[HW13]   X. Hu and H. Wu. Long-time dynamics of the nonhomogeneous incompressible flow of nematic liquid crystals. *Commun. Math. Sci.*, 11(3):779–806, 2013.

[HZE07]   D. Hu, P. Zhang, and W. E. Continuum theory of a moving membrane. *Phys. Rev. E*, 75:041605, 2007.

[JOR17]   T. Jankuhn, M. A. Olshanskii, and A. Reusken. Incompressible Fluid Problems on Embedded Surfaces: Modeling and Variational Formulations. *arXiv:1702.02989*, 2017.

[Kam02]   R. D. Kamien. The geometry of soft materials: a primer. *Rev. Mod. Phys.*, 74:953–971, 2002.

[KLG17]   H. Koba, C. Liu, and Y. Giga. Energetic variational approaches for incompressible fluid systems on an evolving surface. *Quart. Appl. Math.*, 75:359–389, 2017.

[KLLFNV13] V. Koning, T. Lopez-Leon, A. Fernandez-Nieves, and V. Vitelli. Bivalent defect configurations in inhomogeneous nematic shells. *Soft Matter*, 9:4993–5003, 2013.

[KLS$^+$14]   F. C. Keber, E. Loiseau, T. Sanchez, S. J. DeCamp, L. Giomi, M. J. Bowick, M. C. Marchetti, Z. Dogic, and A. R. Bausch. Topology and dynamics of active nematic vesicles. *Science*, 345(6201):1135–1139, 2014.

[KRV11]   S. Kralj, R. Rosso, and E. G. Virga. Curvature control of valence on nematic shells. *Soft Matter*, 7:670–683, 2011.

[Les68]   F. M. Leslie. Some constitutive equations for liquid crystals. *Arch. Ration. Mech. An.*, 28(4):265–283, 1968.

[LL00]   F.-H. Lin and C. Liu. Existence of Solutions for the Ericksen-Leslie System. *Arch. Ration. Mech. An.*, 154(2):135–156, 2000.

[LLFNNB12] T. Lopez-Leon, A. Fernandez-Nieves, M. Nobili, and C. Blanc. Smectic shells. *J. Phys.-Condens. Mat.*, 24(28):284122, 2012.

[LLRV09]   X. Li, J. Lowengrub, A. Rätz, and A. Voigt. Solving PDEs in complex geometries: A diffuse domain approach. *Commun. Math. Sci.*, 7(1):81–107, 2009.

[LLW10]   F. Lin, J. Lin, and C. Wang. Liquid Crystal Flows in Two Dimensions. *Arch. Ration. Mech. An.*, 197(1):297–336, 2010.

[LNZ+13]   H.-L. Liang, J. Noh, R. Zentel, P. Rudquist, and J. Lagerwall. Tuning the defect configurations in nematic and smectic liquid crystalline shells. *Phil. Trans. Roy. Soc. A*, 371(1988), 2013.

[LP92]   T. C. Lubensky and J. Prost. Orientational order and vesicle shape. *J. de Physique II*, 2(3):371–382, 1992.

[LSMS18]   I. B. Liu, N. Sharifi-Mood, and K. J. Stebe. Capillary Assembly of Colloids: Interactions on Planar and Curved Interfaces. *Annu. Rev. Condens. Matter Phys.*, 9:283–305, 2018.

[LSRL11]   H.-L. Liang, S. Schymura, P. Rudquist, and J. Lagerwall. Nematic-Smectic Transition under Confinement in Liquid Crystalline Colloidal Shells. *Phys. Rev. Lett.*, 106:247801, 2011.

[MCP+09]   P. Mullen, K. Crane, D. Pavlov, Y. Tong, and M. Desbrun. Energy-preserving integrators for fluid animation. *ACM T. Graphic.*, 28:38, 2009.

[MHS16]   M. S. Mohamed, A. N. Hirani, and R. Samtaney. Discrete exterior calculus discretization of incompressible Navier-Stokes equations over surface simplicial meshes. *J. Comput. Phys.*, 312:175–191, 2016.

[Miu17]   T.-H. Miura. On singular limit equations for incompressible fluids in moving thin domains. *arXiv:1703.09698*, 2017.

[MRL+14]   A. Martinez, M. Ravnik, B. Lucero, R. Visvanathan, S. Zumer, and I. I. Smalyukh. Mutually tangled colloidal knots and induced defect loops in nematic fields. *Nat. Mater.*, 13:258–263, 2014.

[MSB+18]   O. Mickelin, J. Słomka, K. J. Burns, D. Lecoanet, G. M. Vasil, L. M. Faria, and Jörn Dunkel. Anomalous Chained Turbulence in Actively Driven Flows on Spheres. *Phys. Rev. Lett.*, 120:164503, 2018.

[MT01]   M. Mitrea and M. Taylor. Navier-Stokes equations on Lipschitz domains in Riemannian manifolds. *Math. Ann.*, 321(4):955–987, 2001.

[Nel02]   D. R. Nelson. Toward a Tetravalent Chemistry of Colloids. *Nano Lett.*, 2(10):1125–1129, 2002.

[NNP⁺18]   I. Nitschke, M. Nestler, S. Praetorius, H. Löwen, and A. Voigt. Nematic liquid crystals on curved surfaces – a thin film limit. *Proc. Roy. Soc. A*, 474:20170686, 2018.

[NNPV18]   M. Nestler, I. Nitschke, S. Praetorius, and A. Voigt. Orientational Order on Surfaces: The Coupling of Topology, Geometry, and Dynamics. *J. Nonlinear Sci.*, 28(1):147–191, 2018.

[NNV18]   M. Nestler, I. Nitschke, and A. Voigt. A finite element approach for vector- and tensor-valued surface PDEs. *arXiv:1801.06589*, 2018.

[NRV17]   I. Nitschke, S. Reuther, and A. Voigt. Discrete Exterior Calculus (DEC) for the Surface Navier-Stokes Equation. In Dieter Bothe and Arnold Reusken, editors, *Transport Processes at Fluidic Interfaces*, pages 177–197. Springer, 2017.

[NRV18]   I. Nitschke, S. Reuther, and A. Voigt. Hydrodynamic interactions in polar liquid crystals on evolving surfaces. *arXiv:1809.00457*, 2018.

[NV12]   G. Napoli and L. Vergori. Extrinsic Curvature Effects on Nematic Shells. *Phys. Rev. Lett.*, 108:207803, 2012.

[NV18]   I. Nitschke and A. Voigt. *in preperation*, 2018.

[NVW12]   I. Nitschke, A. Voigt, and J. Wensch. A finite element approach to incompressible two-phase flow on manifolds. *J. Fluid Mech.*, 708:418–438, 2012.

[OQRY18]   M. A. Olshanskii, A. Quaini, A. Reusken, and V. Yushutin. A finite element method for the surface Stokes problem. *arXiv:1801.06589*, 2018.

[PGRPV17]   K. Padberg-Gehle, S. Reuther, S. Praetorius, and A. Voigt. Transfer Operator-Based Extraction of Coherent Features on Surfaces. In Hamish Carr, Christoph Garth, and Tino Weinkauf, editors, *Topological Methods in Data Analysis and Visualization IV: Theory, Algorithms, and Applications*, pages 283–297. Springer, 2017.

[PL96]   J. M. Park and T. C. Lubensky. Sine-Gordon field theory for the Kosterlitz-Thouless transitions on fluctuating membranes. *Phys. Rev. E*, 53:2665–2669, 1996.

[PvdS03]   P. Prinsen and P. van der Schoot. Shape and director-field transformation of tactoids. *Phys. Rev. E*, 68:021701, 2003.

[RDA13]   M. Rahimi, A. DeSimone, and M. Arroyo. Curved fluid membranes behave laterally as effective viscoelastic media. *Soft Matter*, 9:11033–11045, 2013.

[Reu14]   A. Reusken. Analysis of trace Finite Element Methods for surface partial differential equations. *IMA J. Num. Ana.*, 35:1568–1590, 2014.

[RV06]   A. Rätz and A. Voigt. PDE's on surfaces: A diffuse interface approach. *Commun. Math. Sci.*, 4(3):575–590, 2006.

[RV15]   S. Reuther and A. Voigt. The Interplay of Curvature and Vortices in Flow on Curved Surfaces. *Multiscale Model. Sim.*, 13(2):632–643, 2015.

[RV16]   S. Reuther and A. Voigt. Incompressible two-phase flows with an inextensible Newtonian fluid interface. *J. Comput. Phys.*, 322:850–858, 2016.

[RV18a]   S. Reuther and A. Voigt. Erratum: The Interplay of Curvature and Vortices in Flow on Curved Surfaces. *Multiscale Model. Sim.*, 16(3):1448–1453, 2018.

[RV18b]   S. Reuther and A. Voigt. Solving the incompressible surface Navier-Stokes equation by surface finite elements. *Phys. Fluids*, 30(1):012107, 2018.

[RZ13]   A. Reusken and Y. Zhang. Numerical simulation of incompressible two-phase flows with a Boussinesq-Scriven interface stress tensor. *Int. J. Numer. Meth. Fl.*, 73(12):1042–1058, 2013.

[SBX08]   H. Shin, M. J. Bowick, and X. Xing. Topological Defects in Spherical Nematics. *Phys. Rev. Lett.*, 101:037802, 2008.

[Scr60]   L. E. Scriven. Dynamics of a fluid interface equation of motion for Newtonian surface fluids. *Chem. Eng. Sci.*, 12(2):98–108, 1960.

[SD75]   P. G. Saffman and M. Delbrück. Brownian motion in biological membranes. *P. Natl. Acad. Sci. USA*, 72(8):3111–3113, 1975.

[Shk02]   S. Shkoller. Well-posedness and global attractors for liquid crystals on Riemannian manifolds. *Commun. Part. Diff. Eq.*, 27(5-6):1103–1137, 2002.

[SPJVH11]   J. T. Schwalbe, Frederick R. Phelan, Jr., Petia M. Vlahovska, and Steven D. Hudson. Interfacial effects on droplet dynamics in Poiseuille flow. *Soft Matter*, 7:7797–7804, 2011.

[SS82]   T. W. Secomb and R. Skalak. Surface flow of viscoelastic membranes in viscous fluids. *Quart. J. Mech. Appl. Math.*, 35(2):233–247, 1982.

[SSV14]   A. Segatti, M. Snarski, and M. Veneroni. Equilibrium configurations of nematic liquid crystals on a torus. *Phys. Rev. E*, 90:012501, 2014.

[Sta01]   H. Stark. Physics of colloidal dispersions in nematic liquid crystals. *Phys. Rep.*, 351:387–474, 2001.

[STY15]   E. Sasaki, S. Takehiro, and M. Yamada. Bifurcation structure of two-dimensional viscous zonal flows on a rotating sphere. *J. Fluid Mech.*, 774:224–244, 2015.

[SV04]   K. Simons and W. L. C. Vaz. Model systems, lipid rafts, and cell membranes. *Annu. Rev. Bioph. Biom.*, 33:269–295, 2004.

[SV08]   C. Stöcker and A. Voigt. Geodesic Evolution Laws – A Level-Set Approach. *SIAM J. Imaging Sci.*, 1:379–399, 2008.

[SVV05]   C. Stöcker, S. Vey, and A. Voigt. AMDiS – adaptive multidimensional simulation: composite finite elements and signed distance functions. *WSEAS Trans. Circ. Syst.*, 4:111–116, 2005.

[Tem88]   R. Temam. *Infinite-Dimensional Dynamical Systems in Mechanics and Physics.* Springer-Verlag, 1988.

[TLL+09]   K. E. Teigen, X. Li, J. Lowengrub, F. Wang, and A. Voigt. A diffuse-interface approach for modeling transport, diffusion and adsorption/desorption of material quantities on a deformable interface. *Commun. Math. Sci.*, 7:1009–1037, 2009.

[TVN10]   A. M. Turner, V. Vitelli, and D. R. Nelson. Vortices on curved surfaces. *Rev. Mod. Phys.*, 82:1301–1348, 2010.

[VCD+16]   A. Vaxman, M. Campen, O. Diamanti, D. Panozzo, D. Bommes, K. Hildebrandt, and M. Ben-Chen. Directional field synthesis, design and processing. In *EUROGRAPHICS - STAR*, volume 35, pages 1–28. 2016.

[VMV07]   C. Vezy, G. Massiera, and A. Viallat. Adhesion induced nonplanar and asynchronous flow of a giant vesicle membrane in an external flow. *Soft Matter*, 3:844–851, 2007.

[VN06]   V. Vitelli and D. R. Nelson. Nematic textures in spherical shells. *Phys. Rev. E*, 74:021711, 2006.

[VT04]   V. Vitelli and A. M. Turner. Anomalous Coupling Between Topological Defects and Curvature. *Phys. Rev. Lett.*, 93, 2004.

[VV07]   S. Vey and A. Voigt. AMDiS: Adaptive multidimensional simulations. *Comput. Vis. Sci.*, 10(1):57–67, 2007.

[WG12]   F. G. Woodhouse and R. E. Goldstein. Shear-driven circulation patterns in lipid membrane vesicles. *J. Fluid Mech.*, 705:165–175, 2012.

[WLPV15]   T. Witkowski, S. Ling, S. Praetorius, and A. Voigt. Software concepts and numerical algorithms for a scalable adaptive parallel finite element method. *Adv. Comput. Math.*, 41(6):1145–1177, 2015.

[WZZ13]   W. Wang, P. Zhang, and Z. Zhang. Well-Posedness of the Ericksen–Leslie System. *Arch. Ration. Mech. An.*, 210(3):837–855, 2013.

[YOS16]   A. Yavari, A. Ozakin, and S. Sadik. Nonlinear Elasticity in a Deforming Ambient Space. *J. Nonlinear Sci.*, 26(6):1651–1692, 2016.

[YWSG18]   Z. Yang, J. Wei, Y. I. Sobolev, and B. A. Grzybowski. Systems of mechanized and reactive droplets powered by multi-responsive surfactants. *Nature*, 553:313, 2018.

[ZCLS08]   W. Zhou, J. Cao, W. Liu, and S. Stoyanov. How Rigid Rods Self-Assemble at Curved Surfaces. *Angew. Chem. Int. Ed.*, 48(2):378–381, 2008.

Erklärung des Promovierenden zum Antrag auf Eröffnung des Promotionsverfahrens

1. Die folgende Promotionsordnung in ihrer gültigen Fassung erkenne ich an:

    Bereich Mathematik und Naturwissenschaften - Promotionsordnung vom 23.02.2011

2. Die Promotion wurde an folgendem Institut/an folgender Professur durchgeführt:
    Institut für Wissenschaftliches Rechnen /
    Professur für Wissenschaftliches Rechnen und Angewandte Mathematik

3. Folgende Personen haben die Promotion wissenschaftlich betreut und/oder mich bei der Auswahl und Auswertung des Materials sowie bei der Herstellung des Manuskripts unterstützt:

    Prof. Dr. rer. nat. habil. Axel Voigt

    _____

    _____

    _____

4. Ich bestätige, dass für meine Person bisher keine früheren, erfolglosen Promotionsverfahren stattgefunden haben. Andernfalls habe ich diesem Antrag eine Erklärung bzw. Nachweise beigelegt, in dem ersichtlich ist, wo, wann, mit welchem Thema und mit welchem Bescheid diese Promotionsversuche stattgefunden haben

5. Ich versichere weiterhin, dass

(a) ich die vorliegende Arbeit mit dem Titel „The Incompressible Surface Navier-Stokes Equation - Numerical Approaches, Geometric Interactions and Extensions" ohne unzulässige Hilfe Dritter und ohne Benutzung anderer als der angegebenen Hilfsmittel selbst angefertigt habe. Hilfe Dritter wurde nur in wissenschaftlich vertretbarem und prüfungsrechtlich zulässigem Ausmaß in Anspruch genommen. Es sind keine unzulässigen geldwerten Leistungen, weder unmittelbar noch mittelbar, im Zusammenhang mit dem Inhalt der vorliegenden Dissertation an Dritte erfolgt.

(b) die aus fremden Quellen direkt oder indirekt übernommenen Gedanken als solche kenntlich gemacht sind.

(c) ich die vorliegende Arbeit bisher weder im Inland noch im Ausland in gleicher oder ähnlicher Form einer anderen Prüfungsbehörde zum Zwecke einer Promotion oder eines anderen Prüfungsverfahrens vorgelegt habe.

6. Mir ist bekannt, dass die Nichteinhaltung dieser Erklärung oder unrichtige Angaben zum Verfahrensabbruch oder zum nachträglichen Entzug des Doktortitels führen können.

Dresden, 18. Dezember 2018
_____   _____
Ort, Datum   Unterschrift Antragsteller/in